Infrared Spectroscopy of Size Selected
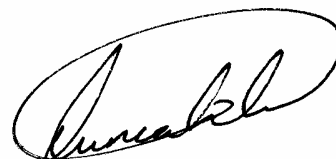
Anion Complexes and Clusters

Duncan Andrew Wild

A thesis submitted in fulfillment of

the requirements for the degree of

Doctor of Philosophy

March, 2003

School of Chemistry

The University of Melbourne

The work reported in this thesis is original except where reference is made to previously published material, and results from investigations undertaken by the author in the School of Chemistry, The University of Melbourne. I declare that this thesis is less than 100,000 words in length, exclusive of tables, diagrams and bibliographies.

Duncan Andrew Wild.

March, 2003.

Abstract

Gas phase anion clusters, consisting of solvent molecules hydrogen bonded to halide anions, are characterised by vibrational predissociation spectroscopy using a combination of mass spectrometry and laser spectroscopy. Monitoring changes in the vibrational properties of neutral solvent molecules when they are attached to a halide anion allows one to infer cluster structures. In some cases, the spectra contain rotationally resolved features, so that quantitative structural parameters can be obtained.

Infrared spectra are recorded for the halide-acetylene clusters, $F^-–(C_2H_2)_n$, $Cl^-–(C_2H_2)_n$, $Br^-–(C_2H_2)_n$, and $I^-–(C_2H_2)_n$. The spectra of the dimer complexes are consistent with linear hydrogen bonded structures. The decreasing strength of the intermolecular bonds as the halide becomes larger is reflected in a progressive reduction in the red shift of the acetylene ν_3 vibrational frequency. Spectra of the argon solvated dimer complexes, $Cl^-–C_2H_2.Ar$, $Br^-–C_2H_2.Ar$, and $I^-–C_2H_2.Ar$, resolve questions concerning the unusual structure of the ν_3 vibrational bands for the bare dimers. Quantitative structural data are obtained for the $Br^-–C_2H_2$ dimer from a spectrum displaying partial rotational resolution. As well, the spectrum allows an accurate determination of the dissociation energy for the complex ($D_o = 3020 \pm 3$ cm^{-1}). Infrared spectra of larger clusters, with up to nine acetylene molecules bound to the anion core, suggest that they posses structures in which the halide is situated in the interior of the cluster. Additional vibrational bands in spectra of clusters containing more than six C_2H_2 ligands provide evidence that the second solvation shell is initiated for n = 6 or 7, and suggest the existence of structural isomers differing in the number of inner and outer shell ligands.

Infrared spectra are reported for the halide-hydrogen complexes, $Cl^-–H_2$, $Br^-–H_2$, $I^-–H_2$, $F^-–(D_2)_n$, $Cl^-–(D_2)_n$, $Br^-–D_2$, and $I^-–D_2$. The form of the spectra suggests that the complexes adopt linear, hydrogen bonded structures. The spectra display complete resolution of rotational features, and upon analysis provide estimates of the vibrationally averaged intermolecular separations, harmonic stretching frequencies and harmonic stretching force constants. Analysis of the line widths for the rovibrational transitions provides estimates of the dissociation rates following *IR* photon absorption. The

spectroscopic data are used to construct empirical radial potential energy curves, describing the interaction between the halide anions and the hydrogen molecule. The curves yield information on the complexes that is not directly provided from the experiments, such as binding energies and anharmonic intermolecular stretching frequencies. Spectra of larger clusters, with more than one hydrogen molecule attached to the halide anion, suggest that they adopt structures with the anion in the interior.

Finally, infrared spectra of the halide-methane anion complexes, F^-–CH_4, Cl^-–CH_4, and Br^-–CH_4, are presented. The spectra are consistent with C_{3v} equilibrium structures in which the halide anion is bound to the methane through a single hydrogen bond. The spectra display partial rotational resolution, exhibiting pronounced Q–branches corresponding to the $\Delta J = 0$, $\Delta K = \pm 1$ transitions characteristic of a prolate symmetric top. Splitting of the Q–branches implies that the complexes are not locked into a vertex–bound structure, but rather that the methane molecule is able to rotate between the four equivalent hydrogen bonded minima. Comparison of the structural and vibrational properties of X^-–CH_4 with those of the isoelectronic X^-–H_2O and X^-–NH_3 complexes shows that the X^-–CH_4 species are the most loosely bound, and display the smallest shift in the hydrogen stretch vibrational frequencies.

Acknowledgments

I am greatly indebted to a number of people. First and foremost I must thank my supervisor Dr. Evan Bieske. I thank him for his patience, support, and generosity throughout my time in the Laser Spectroscopy Group.

I must also thank the other members of the Laser Spectrosocpy Group, both past and present. Paul Weiser, Paula Milley, Rosemary Wilson, and Zoë Loh for your company during the long hours in the laboratory, thank you.

To my friendly proof raeders, Tom Waters, Dr. Toby Bell, Dr. Evan Bieske; Thank-you!

To my support crew at home, thank you for everything. I now realise that the great challenge of completing a PhD is matched only by living with someone undertaking that challenge!

And last, but certainly not least to my fiance, Linda. Thank you for the motivation, support, and understanding during our time together. We met as I was starting to write this thing, and I am surprised that you endured it all!

Publications

The following publications were produced from the work presented in this thesis.

Infrared spectra of $I^--(C_2H_2)_n$ ($1 \leq n \leq 4$) anion complexes
P. S. Weiser, D. A. Wild and E. J. Bieske, Chem. Phys. Lett. **299**, 303–308 (1999)

Infrared spectra of $Cl^--(C_2H_2)_n$ ($1 \leq n \leq 9$) anion clusters: Spectroscopic evidence for solvent shell closure
P. S. Weiser, D. A. Wild and E. J. Bieske, J. Chem. Phys. **110**, 9443–9449 (1999)

The Cl^--CH_4 anion dimer: mid infrared spectrum and ab initio calculations
D. A. Wild, Z. M. Loh, P. P. Wolynec, P. S. Weiser and E. J. Bieske, Chem. Phys. Lett. **332**, 531–537 (2000)

Structural and energetic properties of the $Br^--C_2H_2$ anion complex from rotationally resolved mid–infrared spectra and ab initio calculations
D. A. Wild, P. J. Milley, Z. M. Loh, P. P. Wolynec, P. S. Weiser and E. J. Bieske, J. Chem. Phys. **113**, 1075–1080 (2000)

Infrared spectra of $Br^--(C_2H_2)_n$ complexes
D. A. Wild, P. J. Milley, Z. M. Loh, P. S. Weiser and E. J. Bieske, Chem. Phys. Lett. **323**, 49–54 (2000)

Rotationally resolved infrared spectrum of the Cl^--H_2 anion complex
D. A. Wild, R. L. Wilson, P. S. Weiser and E. J. Bieske, J. Chem. Phys. **113**, 10154–10157 (2000)

Rotationally resolved infrared spectrum of the Br^--D_2 anion complex
D. A. Wild, P. S. Weiser and E. J. Bieske, J. Chem. Phys. **115**, 6394–6400 (2001)

The $^{35}Cl^--H2$ and $^{35}Cl^--D_2$ anion complexes: Infrared spectra and radial intermolecular potentials
D. A. Wild, P. S. Weiser, E. J. Bieske and A. Zehnacker, J. Chem. Phys. **115**, 824–832 (2001)

Infrared Spectra of Size Selected $Cl^--(D_2)_n$ and $F^--(D_2)_n$ Anion Clusters
D. A. Wild, P. S. Weiser, Z. M. Loh and E. J. Bieske, J. Phys. Chem. **106**, 906–910 (2002)

Infrared spectra of the F^--CH_4 and Br^--CH_4 anion complexes
D.A. Wild, Z.M. Loh, and E.J. Bieske, Int. J. Mass. Spectrom., **220**, 273–280 (2002)

Br⁻–H₂ and I⁻–H₂ anion complexes: Infrared spectra and radial intermolecular potential energy curves
D. A. Wild, Z. M. Loh, R. L. Wilson, and E. J. Bieske, J. Chem. Phys. **117(7)**, 3256–3262 (2002)

Locating and confirming the C–H stretch bands of the halide–acetylene anion complexes using argon predissociation spectroscopy
D.A. Wild, Z.M. Loh, R.L. Wilson, E.J. Bieske, Chem. Phys. Lett. **369**, 684–690 (2003)

Infrared investigations of negatively charged complexes and clusters
D.A. Wild and E.J. Bieske, submitted to International Reviews in Physical Chemistry.

The following publication was also produced during the period of PhD candidature.

Infrared and *ab initio* study of the Chloride–Ammonia anion complex
P. S. Weiser, D. A. Wild, P. P. Wolynec and E. J. Bieske, J. Phys. Chem. **104**, 2562–2566 (2000)

Table of Contents

Chapter 1: Introduction

This thesis describes experimental investigations into the structures and energetics of anion clusters in the gas phase, using a combination of mass spectrometry and laser spectroscopy. The work is dedicated to cluster anions comprised of neutral molecules that are hydrogen bonded to a halide anion via electrostatic and induction forces.

The anion clusters are characterised by their infrared absorptions. Infrared spectroscopy is well suited for exploring the properties of hydrogen bonded ionic clusters, providing insights into their structures and the nature of the intermolecular interactions. Some time ago, Pimentel and McClellan noted that, '… the vibrational behaviour of X–H provides the most sensitive, the most characteristic, and one of the most informative manifestations of the hydrogen bond'.[1] With regard to complexes formed between a halide anion and a neutral X–H molecule, hydrogen bond formation results in a weakening of the X–H bond, and a characteristic reduction in the frequency of the X–H stretching motion.

In this thesis, infrared spectra are presented and interpreted for the halide–acetylene clusters [$F^-–(C_2H_2)_n$, $Cl^-–(C_2H_2)_n$, $Br^-–(C_2H_2)_n$, $I^-–(C_2H_2)_n$], the halide–hydrogen clusters [$Cl^-–H_2$, $Br^-–H_2$, $I^-–H_2$, $F^-–(D_2)_n$, $Cl^-–(D_2)_n$, $Br^-–D_2$, $I^-–D_2$], and the halide–methane clusters [$F^-–CH_4$, $Cl^-–CH_4$, and $Br^-–CH_4$]. Spectra of the dimer complexes, $Cl^-–H_2$, $Br^-–H_2$, $I^-–H_2$, $Cl^-–D_2$, $Br^-–D_2$, and $Br^-–C_2H_2$ display resolved rovibrational transitions, which are analysed to provide quantitative structural parameters. Qualitative structures are deduced for the $Cl^-–C_2H_2$, $I^-–C_2H_2$, $F^-–CH_4$, $Cl^-–CH_4$, and $Br^-–CH_4$ dimer complexes and the larger clusters, $F^-–(D_2)_n$, $Cl^-–(D_2)_n$, $F^-–(C_2H_2)_n$, $Cl^-–(C_2H_2)_n$, $Br^-–(C_2H_2)_n$, and $I^-–(C_2H_2)_n$, from spectra displaying vibrational resolution.

1.1 Motivations for investigating gas phase ion complexes

Ions and ionic complexes are active participants in a number of important chemical processes. They play a role in the chemistry of the atmosphere,[2-4] flames,[5, 6] discharges and plasmas, and virtually any gaseous environment where ionisation occurs. To understand the chemistry occurring in these different contexts, a thorough characterisation of the forces that stabilise ion–molecule complexes (electrostatic, induction, and dispersion forces) is desirable. These forces influence the stability of ions in solution, the structures of large biologically important molecules such as proteins, and the macroscopic properties of gases and liquids.

1.1.1 Neutral reaction potential energy surfaces (PES's)

An understanding of anion–neutral complexes can be useful for investigating neutral–neutral reactions. A PES describing a neutral–neutral reaction can be developed by close interaction between experiment and theory. For example, quantities derived from molecular beam scattering experiments such as product angular distributions, translational energies, and internal energy distributions are compared with predictions made employing a model PES. Photoelectron spectroscopy of anion complexes provides another avenue to access, and define, the transition state region of neutral reaction PES's. The anion complex absorbs a fixed frequency photon, resulting in detachment of an electron. The energy spectrum of the emitted electrons reflects the vibrational and electronic energy levels of the neutral transition state complex. Analysis of photoelectron spectra to yield information on the neutral system relies on knowledge of the PES describing the anion–molecule interaction, which in the absence of high resolution spectra for the complex is usually provided by *ab initio* calculations. Interpretation of photoelectron spectra would therefore be improved by an experimentally determined structure for the anion–molecule complex. A relevant example is the elementary triatomic rearrangement reaction:

$$Cl + H_2 \rightarrow HCl + H \qquad\qquad [4]$$

which has been the subject of crossed beam experiments[7-9] and theoretical investigations.[10-12] For elementary reactions, the adiabatically allowed pathway is usually the preferred one.[13, 14] Recent crossed beam experiments suggest however, that spin–orbit excited $Cl*(^2P_{1/2})$ atoms are more reactive with H_2 than ground state Cl $(^2P_{3/2})$ atoms.[7] This violates the adiabatic correlation rule, as the products $HCl(X^1\Sigma^+) + H(^2S)$ correlate adiabatically with $Cl(^2P_{3/2}) + H_2(X^1\Sigma^+)$ reactants. Photoelectron spectra recorded for the Cl$^-$–H$_2$ anion complex[15] provide information on the $Cl+H_2 \rightarrow HCl+H$ reaction PES, as the photo–detachment transitions access the van der Waals well of the PES reactant valley. The photoelectron spectrum, recorded at low resolution, displays transitions to ground and spin–orbit excited states of the Cl.H$_2$ neutral complex. High resolution photoelectron studies should provide information on the low frequency van der Waals progressions of the neutral complex. Interpretation of the high resolution spectra are expected to be aided by the experimentally determined structure of the Cl$^-$–H$_2$ complex presented in Chapter 4 and refs. 16 and 17. Structural information derived for the Br$^-$–H$_2$ and I$^-$–H$_2$ complexes should serve a similar purpose when the corresponding photoelectron spectra are eventually obtained.

1.1.2 Anion–molecule interactions and reactions

Ion–molecule complexes serve as intermediates for many important chemical reactions, including elementary proton transfer and S$_N$2 reactions:

$$X^- + HA \rightarrow [X-HA]^- \rightarrow XH + A^- \qquad [1]$$

$$X^- + H_3CY \rightarrow [XH_3CY]^- \rightarrow XCH_3 + Y^- \qquad [2]$$
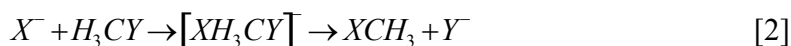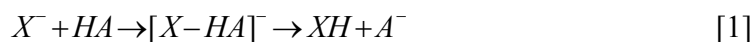
An understanding of the potential energy surfaces that govern these simple reactions is invaluable. High resolution *IR* spectra provide information on the structural and vibrational properties of the intermediate complexes that can be used to critically test *ab initio* potential energy surfaces (PES's). In the absence of high resolution spectra the veracity of calculated PES's is uncertain, and while theoretical methodologies are becoming increasingly sophisticated and reliable, their predictions still require experimental verification.

The dimer complexes studied in this thesis are intermediates for proton transfer reactions [1], and can be thought of as a proton shared between two bases, X^- and A^-:

$$X^- \cdots H^+ \cdots A^- \quad where \quad X^- = F^-, \, Cl^-, \, Br^-, \, I^-$$
$$A^- = H^-, \, CH_3^-, \, C_2H^-$$

[3]
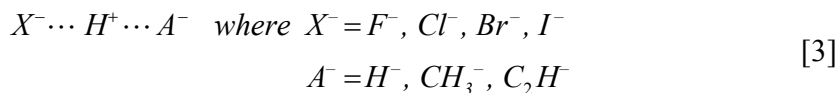
Usually, the intermediate proton is situated closer to the base with the larger proton affinity. For the halide–molecule complexes studied in this thesis, the A^- bases have greater proton affinities than the X^- halide anions, so that the H–A molecules remain essentially intact. Therefore, the complexes are most appropriately described as an X^- anion 'solvated' by a neutral ligand.

Rotationally resolved infrared spectra recorded for the Cl^-–H_2, Br^-–H_2, I^-–H_2, Cl^-–D_2, and Br^-–D_2 complexes provide spectroscopic constants, from which vibrationally averaged structures are deduced. It is hoped that in the future, the structural parameters will be used to test PES's describing the interaction between a halide anion and a hydrogen molecule. The spectroscopic constants are used to generate empirical potential energy curves describing the radial halide–hydrogen intermolecular interaction (Chapter 4). The radial curves can in turn be related to three dimensional *ab initio* PES's.

1.1.3 Anion solvation

Another motivation for studying gas phase anion–molecule complexes and clusters is to understand ion solvation better.[18] The solubility of ions is determined by the interactions between the ion and solvent molecules. The nature of the solute–solvent interaction is generally difficult to ascertain directly from measurements of the properties of bulk solution. Infrared spectroscopic studies of ionic clusters are an attractive means of exploring ion solvent interactions, as the vibrational properties of the solvent molecules depend on the environment in which they are situated. High resolution spectra, with rotational resolution, yield structural parameters for the smaller complexes, while from low resolution spectra one can infer the connectivity of the ligands to the anion for the larger clusters. Cluster structures can often be deduced by following changes in the infrared spectra as the cluster size is increased.

Ions can conceivably exist on the surface or in the interior of a cluster, depending on the nature of the solvating ligand, and on the identity of the ion. The cluster structure depends critically on the balance between the ion–solvent and solvent–solvent intermolecular interactions. The ion tends to exist in the interior of the cluster if the solvent molecules interact weakly with one another, or if they are prevented from bonding together due to strong, highly directional ion–solvent bonds. In contrast, the ion is more likely to exist on the surface of the cluster if the solvent molecules are able to form a stable network with one another, without significantly disrupting the directional nature of the ion–solvent bond. In some systems, the identity of the ion also determines the cluster structure. For example, infrared spectra of the small $X^-–(H_2O)_3$ clusters (X = Cl, Br and I) suggest that the anion is situated on the surface of the cluster,[19] whereas for fluoride–water clusters up to $F^-–(H_2O)_5$, the F^- anion exists in the interior.[20] The difference is ascribed to the stronger, more directional fluoride–water bond that prevents formation of water–water hydrogen bonds observed in $Cl^-–(H_2O)_3$, $Br^-–(H_2O)_3$, and $I^-–(H_2O)_3$.

In this thesis infrared spectra are interpreted to provide cluster structures for the $F^-–(C_2H_2)_n$, $Cl^-–(C_2H_2)_n$, $Br^-–(C_2H_2)_n$, $I^-–(C_2H_2)_n$, $F^-–(D_2)_n$, and $Cl^-–(D_2)_n$ clusters. The infrared spectra suggest that the C_2H_2 and D_2 solvent molecules are bound to the halide anion via linear hydrogen bonds. Under these circumstances, the solvent molecules avoid each other due to repulsive quadrupole–quadrupole forces, thereby preventing formation of a solvent network. The halide ions therefore tend to exist in the interior of these larger clusters.

1.2 *Investigations of ion–molecule complexes and clusters*

The investigation of ionic complexes has traditionally been the domain of mass spectroscopists. Using mass spectrometry, charged species can be securely identified in the gas phase, even when present in extremely low abundances. Several decades ago it was discovered that gas–phase ions tended to aggregate with molecules present in the surrounding gas.[21, 22] This realisation was followed by a series of measurements of clustering equilibria:

$$A^{\pm} - L_n + L \; F \; A^{\pm} - L_{n+1} \qquad\qquad [5]$$
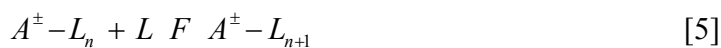
where $A^{\pm}$ is an atomic or molecular ion, and L is a solvent atom or molecule. Clustering experiments are carried out in high pressure mass spectrometers (HPMS), where equilibrium is attained in a high pressure cell and the cluster ion population is determined using mass spectrometry. Measurements of the equilibrium constant of equation [5] over a range of temperatures allows the construction of van't Hoff plots, from which solvent binding enthalpies and entropies can be ascertained. Abrupt decreases in the measured binding enthalpies of the neutral molecules to the cluster, and decreases in the cluster abundances, are often presumed to correspond to solvent shell closure.[23] Although an excellent source of thermochemical data, clustering experiments offer little structural information that can be related to the PES describing the ion–molecule interaction.

Experimental studies of ion–molecule complexes have been paralleled and complemented by *ab initio* calculations that have yielded structural parameters, vibrational frequencies, and binding energies.[24-36] *Ab initio* calculations of anions have been reviewed by Simons and Jordan.[37] Correspondences between calculated and measured vibrational frequencies have been used to distinguish different isomeric forms and to validate interpretations of experimental data. The conjunction of theory and experiment has played a particularly important role in elucidating the structures of the hydrated halide [20, 30, 32, 33, 38] and hydrated electron clusters.[29]

Details of ion–molecule interaction PES's can also be provided by investigating the reactions between ions and molecules. Identification of the reaction products (and their vibrational and rotational states, refs. 39–43), yields information on select regions of the reactive PES. Product distributions, branching ratios, and thermochemical data for gas phase ion–molecule reactions have been probed in crossed beam studies.[44] A beam of ions intersects a beam of neutral molecules at well defined angles and relative kinetic energies, and the resulting energy and angular distributions of the products are analysed. Other techniques for probing elementary ion–molecule reactions include stationary afterglow (SA), flowing afterglow (FA), and selected ion flow tube (SIFT), all of which are bath gas techniques.[45] An ion is reacted with a bath gas, and the products of the

reaction determined via mass spectrometry. Ion cyclotron resonance mass spectrometry (ICR)[46-48] and quadrupole ion traps[49-51] have also been used extensively to probe ion–molecule reactions. These techniques involve trapping ions, reacting them with injected gas, and detecting the products. While these experiments provide an understanding of the reactive processes, they usually do not directly provide information on the minima of the intermolecular PES.

In summary, while mass spectrometry, thermochemical measurements, and scattering experiments provide useful information on the existence, stability, and reactivity of ion–molecule complexes, such studies provide little structural information that can be used to test calculated anion–molecule PES's. Structural information is best supplied by high resolution spectroscopy.

1.3 Spectroscopy of ion complexes

Spectroscopic investigations of cluster ions have lagged behind those of neutral molecular species. The reasons for this are difficulties associated with cluster production, the sensitivity of standard spectroscopic techniques, and a lack of selectivity for a specific cluster. Ionic clusters are bound by weak intermolecular forces (electrostatic, induction, dispersion forces) and hence are difficult to produce in great abundance. Specialised ion sources that combine supersonic gas expansions[52] with plasmas and discharges are commonly used. In the initial part of the expansion, where the gas density is high, three–body collisions between ions and neutral species permit formation of complexes and clusters. Subsequent collisional cooling reduces the vibrational and rotational energy of the clusters, decreasing the chance of dissociation prior to spectroscopic interrogation, and simplifying the spectra ultimately obtained.

Traditional spectroscopic techniques that rely upon the attenuation of light passing through a sample are generally not applicable to the investigation of ionic clusters. The problem is one of sensitivity, as the density of a specific cluster within a plasma, or beam of ions, is usually quite low. A multi–pass optical cell combined with an electron impact plasma ion source has been used to increase the effective absorption pathlength.[53] Poor sensitivity due to low concentration of the ion complex can also be

circumvented by deposition of the species onto a rare gas matrix prior to spectroscopic interrogation.[54]   While both these techniques result in enhanced sensitivity, they do not account for the lack of cluster selectivity.

Plasmas and discharges are fertile chemical environments that are conducive to the production of an array of ionic complexes and clusters. To complicate matters, if the spectroscopic interrogation is performed on the plasma, the neutral precursor molecules are present in far larger concentrations than the ionic species, and hence the spectra are usually dominated by absorptions of neutral species. To determine the properties of a specific ion complex, selectivity prior to spectroscopic interrogation is usually required. To this end, the greatest advantage spectroscopists have is that the species are charged. The selection and isolation of specific ion complexes from a plasma is easily achieved by mass spectrometry. Furthermore, by use of electric or magnetic fields, the ions can be guided, slowed, and trapped to increase their temporal or spatial overlap with the probe light source. A further advantage for the experimentalist is that ionic complexes and clusters are generally weakly bound, and hence the absorption of a photon may lead to cluster dissociation producing an observable ionic fragment that in turn can be selected and detected with great efficiency.

1.3.1 Previous studies – Cations

The first spectroscopic studies of gas phase ionic clusters and complexes concentrated on cation systems. Cation complexes have been characterised via their electronic and infrared absorptions. Microwave spectra have been recorded for Ar–HCO^+ (ref. 55), Kr–HCO^+ (ref. 56), and Ar–H_3^+ (refs. 57–59). The first application of infrared spectroscopy to cation complexes and clusters was in 1985 by Lee and co–workers.[60] They combined laser spectroscopy with mass spectrometry to probe H_5^+, H_7^+, and H_9^+ by detecting photo–fragmentation products following resonant absorption of infrared radiation. The technique, termed infrared predissociation (IRPD) or vibrational predissociation spectroscopy (VPS), relies on transitions to excited vibrational states leading to dissociation of the complexes. Spectra were recorded by monitoring the abundance of the photo–fragments *vs* the *IR* photon wavenumber. Following these initial studies, Lee and coworkers investigated the hydrated hydronium clusters, H_3O^+–$(H_2O)_n$

(refs. 61 and 62), which are important in aqueous chemistry, and the ammoniated ammonium ion clusters, NH_4^+–$(NH_3)_n$ (refs. 63 and 64). Other groups have since used IRPD to undertake infrared investigations of a large variety of cation complexes and clusters including proton–bound complexes,[65, 66] metal–ligand complexes,[67-69] and clusters containing aromatic molecules.[70, 71] Progress in spectroscopic studies of ionic complexes since 1985 is described in refs. 66, 68, 72, and 73.

1.3.2 Previous studies – Anions

Spectroscopic investigations of gas phase anion complexes have trailed behind those of cations, and have been restricted to infrared and photoelectron techniques. Generally, electronic spectroscopy cannot be applied to anion complexes as most anions do not posses excited electronic states lying below the electron detachment threshold. Anion photoelectron spectroscopy provides dissociation energies for anion–molecule complexes, and vertical electron detachment energies. Sudden declines in the bond energies for the larger clusters are presumed to correspond to solvent shell filling.[74-78] Zero electron kinetic energy spectroscopy (ZEKE),[79, 80] a variant of photoelectron spectroscopy with substantially better resolution, has proved capable of yielding spectra that can be interpreted to furnish empirical potential energy curves describing anion–neutral interactions as shown in the recent studies of the $ArCl^-$, $KrBr^-$, $XeBr^-$, and $KrCl^-$ dimers.[81, 82] To date, no microwave spectra have been reported for gas phase anion complexes. Apart from the infrared spectra of the Cl^-–H_2, Br^-–H_2, I^-–H_2, Cl^-–D_2, Br^-–D_2, and Br^-–C_2H_2 complexes presented in this thesis, there have been no rotationally resolved spectra reported for weakly bound anion complexes (*J* structure). Partial rotational resolution (*K* structure) has been observed in spectra of I^-–HDO (ref. 83), Cl^-–CH_3Br (ref. 25), and I^-–CH_3 (ref. 84). *IR* spectra displaying full rotational resolution have been recorded for the strongly bound FHF^- (ref. 85) and $ClHCl^-$ (ref. 86) anion complexes.

The first application of infrared spectroscopy to a gas phase anion complex was by Okumura and co–workers in 1996 for the iodide–water complex, I^-–H_2O.[87] Since that time more than 30 different anion clusters and complexes have been characterised. Table 1.1 provides a list of the systems studied so far. The complexes and clusters that

are the subject of this thesis are highlighted. The list is reasonably comprehensive at the time of writing, yet is sure to be rapidly superseded. The majority of the systems studied are hydrogen bonded clusters, involving neutral molecules bound to halide anions. The halide–water complexes have received the most attention, due to their obvious importance in understanding aqueous halide solvation. The first spectra recorded for the strongly bound halide–water complexes were dominated by absorptions of 'hot' complexes, as a single *IR* photon does not provide cold complexes with sufficient energy to dissociate.[88, 89] This problem was overcome in the argon predissociation studies of the $X^- - (H_2O)_n.Ar_m$ clusters by Johnson and coworkers.[19, 90-92] The absorption of an *IR* photon by the core $X^- - (H_2O)_n$ cluster was observed from dissociation of the loosely bound Ar atoms to produce detectable ionic fragments.

Table 1.1: *Anion complexes and clusters characterised using infrared spectroscopy. Clusters studied in this thesis are highlighted*

Complex	Comments	Reference(s)
Hydrogen Bonded		
F^-–$(D_2)_n$	to n=6	93
Cl^-–$(H_2)_n$	to n=3; rotational resolution for Cl^-–H_2 & Cl^-–D_2	16, 17, 93
Br^-–H_2	rotational resolution for Br^-–H_2 & Br^-–D_2	94, 95
I^-–H_2	rotational resolution	95
Br^-–$(HBr)_n$	to n=3	96, 97
F^-–$(H_2O)_n$	to n=5	20, 90
Cl^-–$(H_2O)_n$	to n=5	19, 89, 90, 98-101
Br^-–$(H_2O)_n$	to n=6	19, 88, 90, 98
I^-–$(H_2O)_n$	to n=6; partial rotational resolution for I^-–HDO	19, 83, 87, 88, 90, 91, 98, 102
O_2^-–$(H_2O)_n$	to n=6	103, 104
NO^-–(H_2O)		105
OH^-–$(H_2O)_n$	to n=5	106, 107
SO_2^-–H_2O	double H–bond	108
F^-–$(C_2H_2)_n$	to n=6	
Cl^-–$(C_2H_2)_n$	to n=9	109, 110
Br^-–$(C_2H_2)_n$	to n=8; partial rotational resolution for Br^-–C_2H_2	110-112
I^-–$(C_2H_2)_n$	to n=4	110, 113
Cl^-–NH_3	single H–bond	114
I^-–CH_3	open shell, partial rotational resolution	84
Br^-–CH_2Br	open shell	84
F^-–$(CH_4)_n$	partial rotational resolution	115
Cl^-–$(CH_4)_n$	partial rotational resolution	116
Br^-–$(CH_4)_n$	partial rotational resolution	115
I^-–HCOOH	double H–bond	117
F^-–$(CH_3OH)_n$	up to n=13	118
Cl^-–$(CH_3OH)_n$	up to n=12	119
I^-–$(CH_3OH)_n$	up to n=2	24, 120
I^-–C_2H_5OH		120
I^-–C_3H_7OH		120
S_N2		
Cl^-–CH_3Br	partial rotational resolution	25
Cl^-–$(CH_3Cl)_n$	925–1090 cm^{-1}	26
Br^-–$(CH_3Br)_n$	925–1090 cm^{-1}	26
Other		
$(H_2O)_n^-$	hydrated electron clusters	27-29
O_4^-	*IR* electronic abs., vibrational progressions	121

The remainder of this thesis describes infrared spectroscopic investigations of the halide–acetylene, halide–hydrogen, and halide–methane complexes and clusters in the gas phase. The chapters are set out as follows:

Chapter 2 describes the experimental strategy and apparatus. The technique of vibrational predissociation spectroscopy (VPS), as applied to anion clusters and complexes, is discussed. The experimental apparatus, consisting of the tandem mass spectrometer (TMS) and optical parametric oscillator (OPO) infrared light source, is then described.

Chapter 3 describes investigations of the halide–acetylene clusters, $F^-–(C_2H_2)_n$, $Cl^-–(C_2H_2)_n$, $Br^-–(C_2H_2)_n$, and $I^-–(C_2H_2)_n$. Apart from the $Br^-–C_2H_2$ dimer complex, the spectra display vibrational resolution. The form of the spectra suggests that the complexes adopt linear, hydrogen bonded structures. Based on the infrared spectra, structures are proposed for the larger clusters.

Chapter 4 deals with the halide–hydrogen complexes, $Cl^-–H_2$, $Br^-–H_2$, $I^-–H_2$, $F^-–(D_2)_n$, $Cl^-–(D_2)_n$, $Br^-–D_2$, and $I^-–D_2$. Full resolution of rotational features is observed for the dimer complexes. The spectra are analysed to provide rotational constants, from which structural parameters are derived. The rotational constants are used to develop one dimensional potential energy curves describing the halide–hydrogen interaction. Spectra of the larger clusters, $F^-–(D_2)_n$ and $Cl^-–(D_2)_n$, are used to deduce their structures.

Chapter 5 is a discussion of the halide–methane complexes, $F^-–CH_4$, $Cl^-–CH_4$, and $Br^-–CH_4$. The spectra are consistent with C_{3v} structures in which the halide is bound to the methane via a single hydrogen bond. The vibrational bands are split, indicating that the complexes are not rigid, and that tunnelling of the methane molecule between the four equivalent vertex–bound minima is feasible.

1.4 *References:*

1. G. C. Pimentel and A. L. McClellan, *The Hydrogen Bond* (W.H. Freeman, New York, 1960)

2. G. de Petris, Acc. Chem. Res. **35**, 305 (2002)

3. R. S. MacTaylor and A. W. Castleman Jr., J. Atmos. Chem. **36**, 23 (2000)

4. D. Smith and P. Spanel, Mass Spec. Rev. **14**, 255 (1996)

5. J. M. Goodings, S. D. Tanner and D. K. Bohme, Can. J. Chem. **60**, 2766 (1982)

6. A. B. Fialkov, Progress in Energy and Combustion Science **23**, 399 (1997)

7. F. Dong, S-H. Lee and K. Liu, J. Chem. Phys. **115**, 1197 (2001)

8. S. H. Lee and K. Liu, J. Chem. Phys. **111**, 6253 (1999)

9. S. H. Lee, L. H. Lai, K. Liu and H. Chang, J. Chem. Phys. **110**, 8229 (1999)

10. M. H. Alexander, G. Capecchi and H-J. Werner, Science **296**, 715 (2002)

11. W. Bian and H. J. Werner, J. Chem. Phys. **112**, 220 (2000)

12. U. Manthe, W. Bian and H. J. Werner, Chem. Phys. Lett. **313**, 647 (1999)

13. R. J. Donovan and D. Husain, Chem. Rev. **70**, 489 (1970)

14. P. J. Dagdigian and M. L. Campbell, Chem. Rev. **87**, 1 (1987)

15. M. J. Ferguson, G. Meloni, H. Gomez and D. M. Neumark, J. Chem. Phys. **117**, 8181 (2002)

16. D. A. Wild, R. L. Wilson, P. S. Weiser and E. J. Bieske, J. Chem. Phys. **113**, 10154 (2000)

17. D. A. Wild, P. S. Weiser, E. J. Bieske and A. Zehnacker, J. Chem. Phys. **115**, 824 (2001)

18. K. Takashima and J. M. Riveros, Mass Spec. Rev. **17**, 409 (1998)

19. P. Ayotte, G. H. Weddle and M. A. Johnson, J. Chem. Phys. **110**, 7129 (1999)

20. O. M. Cabarcos, C. J. Weinheimer, J. M. Lisy and S. S. Xantheas, J. Chem. Phys. **110**, 5 (1999)

21. P. Kebarle, Ann. Rev. Phys. Chem. **28**, 445 (1977)

22. A. W. Castleman Jr. and R. G. Keesee, Chem. Rev. **86**, 589 (1986)

23. M. M. Meot-Ner and C. V. Speller, J. Phys. Chem. **90**, 6616 (1986)

24. W. H. Robertson, K. Karapetian, P. Ayotte, K. D. Jordan and M. A. Johnson, J. Chem. Phys. **116**, 4853 (2002)

25. P. Ayotte, J. Kim, J. A. Kelley, S. B. Nielsen and M. A. Johnson, J. Am. Chem. Soc. **121**, 6950 (1999)

26. M. Ichihasi, Y. Sadanaga, J. M. Lisy and T. Kondow, Chem. Lett. **11**, 1240 (2000)

27. C. G. Bailey, J. Kim and M. A. Johnson, J. Phys. Chem. **100**, 16782 (1996)

28. P. Ayotte, C. G. Bailey, J. Kim and M. A. Johnson, J. Chem. Phys. **108**, 444 (1998)

29. P. Ayotte, G. H. Weddle, C. G. Bailey, M. A. Johnson, F. Vila and K. D. Jordan, J. Chem. Phys. **110**, 6268 (1999)

30. S. S. Xantheas, J. Phys. Chem. **100**, 9703 (1996)

31. A. I. Boldyrev, J. Simons, G. V. Mil'nikov, V. A. Benderskii, S. Y. Grebenshchikov and E. V. Vetoshkin, J. Chem. Phys. **102**, 1295 (1995)

32. S. S. Xantheas and T. H. Dunning Jr., J. Phys. Chem. **98**, 13489 (1994)

33. S. S. Xantheas, J. Am. Chem. Soc. **117**, 10373 (1995)

34. P. Botschwina and H. Stoll, Phys. Chem. Chem. Phys. **3**, 1965 (2001)

35. P. Botschwina, T. Dutoi, M. Mladenovic, R. Oswald, S. Schmatz and H. Stoll, Faraday Disc. **118**, 433 (2001)

36. M. Gutowski, P. Skurski, K. D. Jordan and J. Simons, Int. J. Quant. Chem. **64**, 183 (1997)

37. J. Simons and K. H. Jordan, Chem. Rev. **87**, 535 (1987)

38. J. E. Combariza, N. R. Kestner and J. Jortner, Chem. Phys. Lett. **203**, 423 (1993)

39. T. S. Zwier, J. C. Weisshaar and S. R. Leone, J. Chem. Phys. **75**, 4885 (1981)

40. J. C. Weisshaar, T. S. Zwier and S. R. Leone, J. Chem. Phys. **75**, 4873 (1981)

41. D. R. Guyer, L. Huwel and S. R. Leone, J. Chem. Phys. **79**, 1259 (1983)

42. J. M. Farrar, Ann. Rev. Phys. Chem. **46**, 525 (1995)

43. R. J. Green and R. N. Zare, J. Chem. Phys. **107**, 772 (1997)

44. Z. Herman, Int. J. Mass Spectrom. **212**, 413 (2001)

45. N. G. Adams and D. Smith, in *Techniques For The Study Of Ion-Molecule Reactions*, edited by J. M. Farrar and W. H. Saunders Jr (Wiley, New York, 1988)

46. R. C. Dunbar, Chem. React. React. Paths 339 (1974)

47. N. M. M. Nibbering, Adv. Mass Spec. **10**, 417 (1986)

48. N. M. M. Nibbering, Acc. Chem. Res. **23**, 279 (1990)

49. M. Welling, H. A. Schuessler, R. I. Thompson and H. Walther, Int. J. Mass Spec. Ion Proc. **172**, 95 (1998)

50. R. W. Vachet, J. A. R. Hartman and J. H. Callahan, J. Mass Spec. **33**, 1209 (1998)

51. G. P. Jackson, F. L. King, D. E. Goeringer and D. C. Duckworth, J. Phys. Chem. **106**, 7788 (2002)

52. J. B. Fenn, Int. J. Mass. Spectrom. **200**, 459 (2000)

53. T. Ruchti, A. Rohrbacher, T. Speck, J. P. Connelly, E. J. Bieske and J. P. Maier, Chem. Phys. **209**, 169 (1996)

54. M. E. Jacox, Chem. Rev. Soc. **31**, 108 (2002)

55. Y. Ohshima, Y. Sumiyoshi and Y. Endo, J. Chem. Phys. **106**, 2977 (1997)

56. K. Seki, Y. Sumiyoshi and Y. Endo, Chem. Phys. Lett. **331**, 184 (2000)

57. M. Bogey, H. Bolvin, C. Demuynck and J. L. Destombes, Phys. Rev. Lett. **58**, 988 (1987)

58. S. Bailleux, M. Bogey, H. Bolvin, S. Civis, M. Cordonnier, A. F. Krupnov, M. Y. Tretyakov, A. Walters and L. H. Coudert, J. Mol. Spec. **190**, 130 (1998)

59. M. Bogey, H. Bolvin, C. Demuynck, J. L. Destombes and B. P. Van Eijck, J. Chem. Phys. **88**, 4120 (1988)

60. M. Okumura, L. I. Yeh and Y. T. Lee, J. Chem. Phys. **83**, 3705 (1985)

61. L. I. Yeh, M. Okumura, J. D. Myers, J. M. Price and Y. T. Lee, J. Chem. Phys. **91**, 7319 (1989)

62. M. Okumura, L. I. Yeh, J. D. Myers and Y. T. Lee, J. Phys. Chem. **94**, 3416 (1990)

63. J. M. Price, M. W. Crofton and Y. T. Lee, J. Chem. Phys. **91**, 2749 (1989)

64. J. M. Price, M. W. Crofton and Y. T. Lee, J. Phys. Chem. **95**, 2182 (1991)

65. M. W. Crofton, J. M. Price and Y. T. Lee, Springer Ser. Chem. Phys. **56**, 44 (1994)

66. E. J. Bieske and O. Dopfer, Chem. Rev. **100**, 3963 (2000)

67. C. J. Weinheimer and J. M. Lisy, J. Chem. Phys. **105**, 2938 (1996)

68. J. M. Lisy, Int. Rev. Phys. Chem. **16**, 267 (1997)

69. G. Gregoire and M. A. Duncan, J. Chem. Phys. **117**, 2120 (2002)

70. M. Miyazaki, A. Fujii, T. Ebata and N. Mikami, Chem. Phys. Lett. **349**, 431 (2001)

71. N. Solca and O. Dopfer, J. Phys. Chem. **105**, 5637 (2001)

72. E. J. Bieske and J. P. Maier, Chem. Rev. **93**, 2603 (1993)

73. M. A. Duncan, Int. J. Mass. Spectrom. **200**, 545 (2000)

74. G. Markovich, R. Giniger, M. Levin and O. Cheshnovsky, J. Chem. Phys. **95**, 9416 (1991)

75. S. T. Arnold, J. H. Hendricks and K. H. Bowen, J. Chem. Phys. **102**, 39 (1995)

76. G. Markovich, L. Perera, M. L. Berkowitz and O. Cheshnovsky, J. Chem. Phys. **105**, 2675 (1996)

77. K. R. Asmis, T. R. Taylor, C. Xu and D. M. Neumark, J. Chem. Phys. **109**, 4389 (1998)

78. H. Gomez, T. R. Taylor and D. M. Neumark, J. Chem. Phys. **116**, 6111 (2002)

79. U. Boesl, C. Bassmann and E. W. Schlag, Adv. Ser. Phys. Chem. **10B**, 809 (2000)

80. E. W. Schlag, Adv. Chem. Phys. **101**, 607 (1997)

81. I. Yourshaw, T. Lenzer, G. Resier and D. M. Neumark, J. Chem. Phys. **109**, 5247 (1998)

82. T. Lenzer, I. Yourshaw, M. R. Furlanetto, G. Resier and D. M. Neumark, J. Chem. Phys. **110**, 9578 (1999)

83. C. G. Bailey, J. Kim, C. E. H. Dessent and M. A. Johnson, Chem. Phys. Lett. **269**, 122 (1997)

84. S. B. Nielsen, P. A. Ayotte, J. A. Kelley and G. H. Weddle, J. Chem. Phys. **111**, 10464 (1999)

85. K. Kawaguchi and E. Hirota, J. Chem. Phys. **87**, 6838 (1987)

86. K. Kawaguchi, J. Chem. Phys. **88**, 4186 (1988)

87. M. S. Johnson, K. T. Kuwata, C. Wong and M. Okumura, Chem. Phys. Lett. **260**, 551 (1996)

88. P. Ayotte, C. G. Bailey and M. A. Johnson, J. Phys. Chem. **102**, 3067 (1998)

89. J. H. Choi, K. T. Kuwata, Y. B. Cao and M. Okumura, J. Phys. Chem. **102**, 503 (1998)

90. P. Ayotte, S. B. Nielsen, G. H. Weddle, M. A. Johnson and S. S. Xantheas, J. Phys. Chem. **103**, 10665 (1999)

91. P. Ayotte, G. H. Weddle, J. Kim and M. A. Johnson, Chem. Phys. **239**, 485 (1998)

92. P. Ayotte, J. A. Kelly, S. B. Nielsen and M. A. Johnson, Chem. Phys. Lett. **316**, 455 (2000)

93. D. A. Wild, P. S. Weiser, Z. M. Loh and E. J. Bieske, J. Phys. Chem. **106**, 906 (2002)

94. D. A. Wild, P. S. Weiser and E. J. Bieske, J. Chem. Phys. **115**, 6394 (2001)

95. D. A. Wild, Z. M. Loh, R. L. Wilson and E. J. Bieske, J. Chem. Phys. **117**, 3256 (2002)

96. N. L. Pivonka, C. Kaposta, G. von Helden, G. Meijer, L. Wöste, D. M. Neumark and K. R. Asmis, J. Chem. Phys. **117**, 6493 (2002)

97. N. L. Pivonka, C. Kaposta, M. Brummer, G. von Helden, G. Meijer, L. Woste, D. M. Neumark and K. R. Asmis, J. Chem. Phys. **118**, 5275 (2003)

98. P. Ayotte, G. H. Weddle, J. Kim and M. A. Johnson, J. Am. Chem. Soc. **120**, 12361 (1998)

99. J. A. Kelly, J. M. Weber, K. M. Lisle, W. H. Robertson, P. Ayotte and M. A. Johnson, Chem. Phys. Lett. **327**, 1 (2000)

100. S. A. Corcelli, J. A. Kelley, J. C. Tully and M. A. Johnson, J. Phys. Chem. **106**, 4872 (2002)

101. W. H. Robertson, G. H. Weddle, J. A. Kelley and M. A. Johnson, J. Phys. Chem. **106**, 1205 (2002)

102. P. Ayotte, G. H. Weddle, J. Kim, J. Kelley and M. A. Johnson, J. Phys. Chem. **103**, 443 (1999)

103. J. M. Weber, J. A. Kelley, S. B. Nielsen, P. Ayotte and M. A. Johnson, Science **287**, 2461 (2000)

104. J. M. Weber, J. A. Kelley, W. H. Robertson and M. A. Johnson, J. Chem. Phys. **114**, 2698 (2001)

105. W. H. Robertson, M. A. Johnson, E. M. Myshakin and K. D. Jordan, J. Phys. Chem. **106**, 10010 (2002)

106. C. Chaudhuri, Y. S. Wang, J. C. Jiang, Y. T. Lee, H. C. Chang and G. Niedner-Schatteburg, Mol. Phys. **99**, 1161 (2001)

107. E. A. Price, W. H. Robertson, E. G. Diken, G. H. Weddle and M. A. Johnson, Chem. Phys. Lett. **366**, 412 (2002)

108. E. A. Woronowicz, W. H. Robertson, G. H. Weddle, M. A. Johnson, E. M. Myshakin and K. D. Jordan, J. Phys. Chem. **106**, 7086 (2002)

109. P. S. Weiser, D. A. Wild and E. J. Bieske, J. Chem. Phys. **110**, 9443 (1999)

110. D. A. Wild, Z. M. Loh, R. L. Wilson and E. J. Bieske, Chem. Phys. Lett. **369**, 684 (2003)

111. D. A. Wild, P. J. Milley, Z. M. Loh, P. P. Wolynec, P. S. Weiser and E. J. Bieske, J. Chem. Phys. **113**, 1075 (2000)

112. D. A. Wild, P. J. Milley, Z. M. Loh, P. S. Weiser and E. J. Bieske, Chem. Phys. Lett. **323**, 49 (2000)

113. P. S. Weiser, D. A. Wild and E. J. Bieske, Chem. Phys. Lett. **299**, 303 (1999)

114. P. S. Weiser, D. A. Wild, P. P. Wolynec and E. J. Bieske, J. Phys. Chem. **104**, 2562 (2000)

115. D. A. Wild, Z. M. Loh and E. J. Bieske, Int. J. Mass. Spectrom. **220**, 273 (2002)

116. D. A. Wild, Z. M. Loh, P. P. Wolynec, P. S. Weiser and E. J. Bieske, Chem. Phys. Lett. **332**, 531 (2000)

117. W. H. Robertson, J. A. Kelley and M. A. Johnson, J. Chem. Phys. **113**, 7879 (2000)

118. C. A. Corbett, T. J. Martinez and J. M. Lisy, J. Phys. Chem. **106**, 10015 (2002)

119. O. M. Cabarcos, C. J. Weinheimer, T. J. Martinex and J. M. Lisy, J. Chem. Phys. **110**, 9516 (1999)

120. S. B. Nielsen, P. A. Ayotte, J. A. Kelley and M. A. Johnson, J. Chem. Phys. **111**, 9593 (1999)

121. J. A. Kelley, W. H. Robertson and M. A. Johnson, Chem. Phys. Lett. **362**, 255 (2002)

Chapter 2: Experimental strategy and apparatus

The infrared spectra presented in this thesis are obtained by vibrational predissociation spectroscopy (VPS), a technique that combines mass spectrometry and laser spectroscopy. Cluster ions are produced, mass selected, and overlapped with tuneable infrared radiation which for appropriate wavelengths excites the clusters to predissociative vibrational levels. Following dissociation, the ionic fragments are mass selected and detected. Spectra are recorded by monitoring fragment ion intensity as a function of infrared photon wavenumber.

The following discussion of the experimental strategy and apparatus is divided into three sections. Firstly, a brief overview of vibrational predissociation spectroscopy (VPS) is provided, including a discussion of the limitations of the technique and the additional information that is provided (other than (ro)vibrational frequencies). The experimental apparatus, consisting of the tandem mass spectrometer (TMS) and optical parametric oscillator (OPO) infrared light source, is then discussed. The chapter concludes with a description of the data collection protocol.

2.1: Vibrational predissociation spectroscopy

The technique of vibrational predissociation spectroscopy involves the preparation of an excited vibrational state, energy transfer into a weak intermolecular bond, and consequent dissociation of the complex. Fig. 2.1 provides a schematic representation of VPS for a generic hydrogen bonded X^-–HA complex. The lower and upper potential energy curves correspond, respectively, to the anion X^- interacting with the HA molecule in the $v_{AH} = 0$ and $v_{AH} = 1$ vibrational states. The energy levels supported by the potentials correspond to the intermolecular stretching vibrational levels. Absorption of an *IR* photon, having appropriate frequency, results in a transition from an energy level supported by the $v_{AH} = 0$ curve to an energy level associated with the $v_{AH} = 1$ curve. Dissociation of the complex ensues if the wavefunction of the prepared upper state couples with continuum wavefunctions associated with the $X^- + HA$ ($v_{AH} = 0$) potential energy curve. Dissociation results in a charged X^- and neutral HA ($v_{AH} = 0$) fragment, with the excess energy appearing as fragment translational and rotational

energy. For a more detailed description of vibrational predissociation, the reader is directed to refs. 1 and 2.
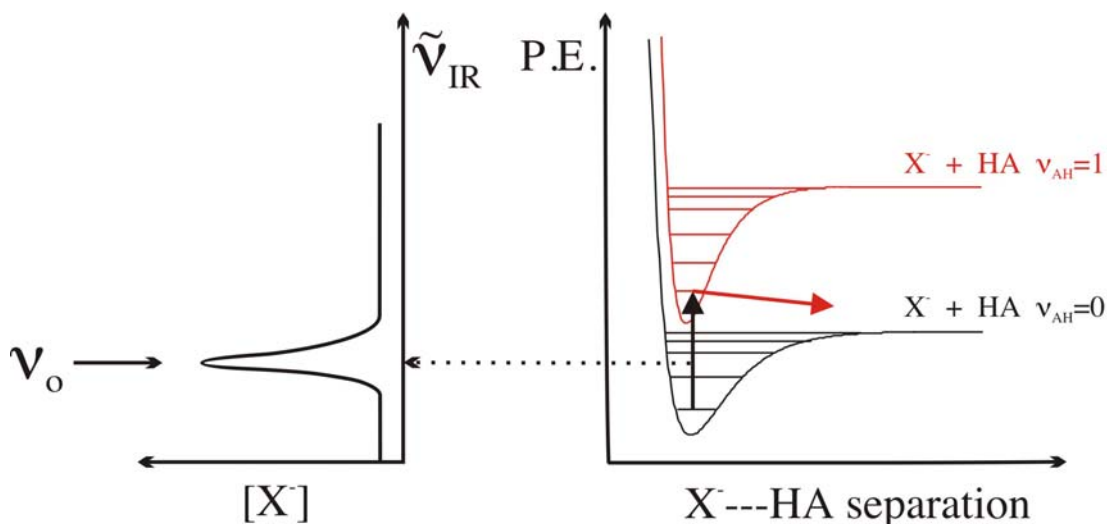

Figure 2.1: *Diagram illustrating the VPS process. The potential energy curves correspond to X^- interacting with molecule HA in $v_{AH} = 0$ and $v_{AH} = 1$ vibrational states. To the left is the resulting spectrum, recorded by monitoring the X^- fragment ions vs IR wavenumber.*

One limitation of VPS is that it is only useful for probing transitions that terminate above the clusters' dissociation threshold. Fig. 2.2 represents two possible situations. In the first case, absorption of an *IR* photon results in dissociation, and the X^- ionic fragment is detected. In the second case, the transition terminates below the X^- + HA ($v_{AH} = 0$) dissociation asymptote and, as fragments are not detected, the transition is not observed. For the second case (shown in Fig. 2.2.b), hot bands involving the low frequency intermolecular vibrations can be excited. Transitions to levels that terminate above the dissociation threshold will lead to detectable ionic fragments. This situation is shown in Fig. 2.3. While a spectrum can be obtained, the fundamental transition v_o is not observed. Generally, the upper state potential energy curve is deeper than the lower state curve, so that the hot band transitions are displaced to higher energy from the v_o transition.
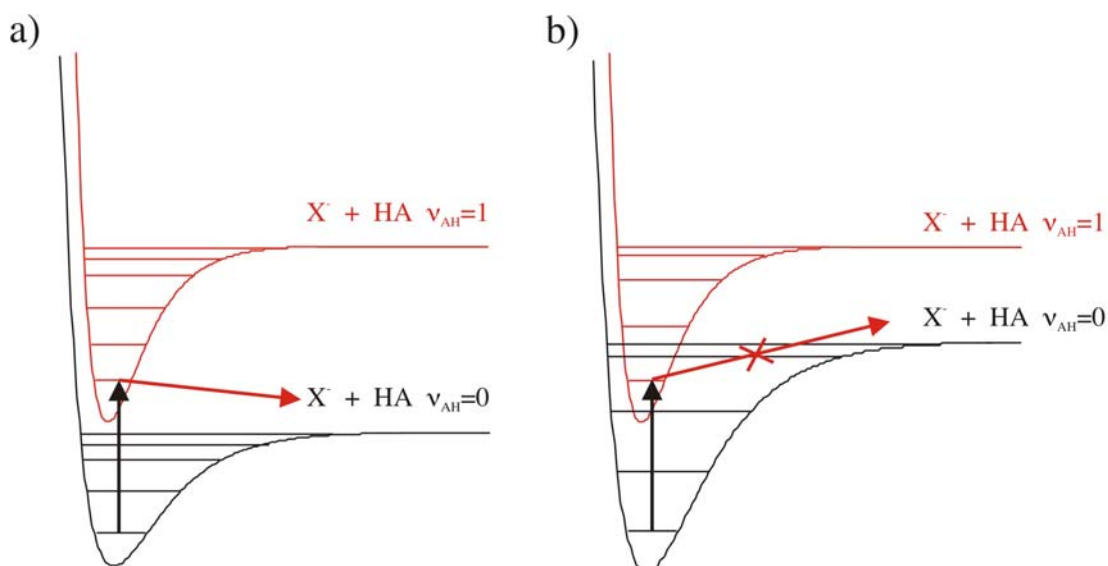
Figure 2.2: *Potential energy curves describing the interaction between the anion X^- and the molecule HA ($v_{AH} = 0$ and 1). a) corresponds to the case where the IR photon energy exceeds the binding energy of the complex and dissociation occurs. b) corresponds to the case where the IR photon energy is less than the binding energy of the complex, and dissociation is not possible from the ground vibrational state.*
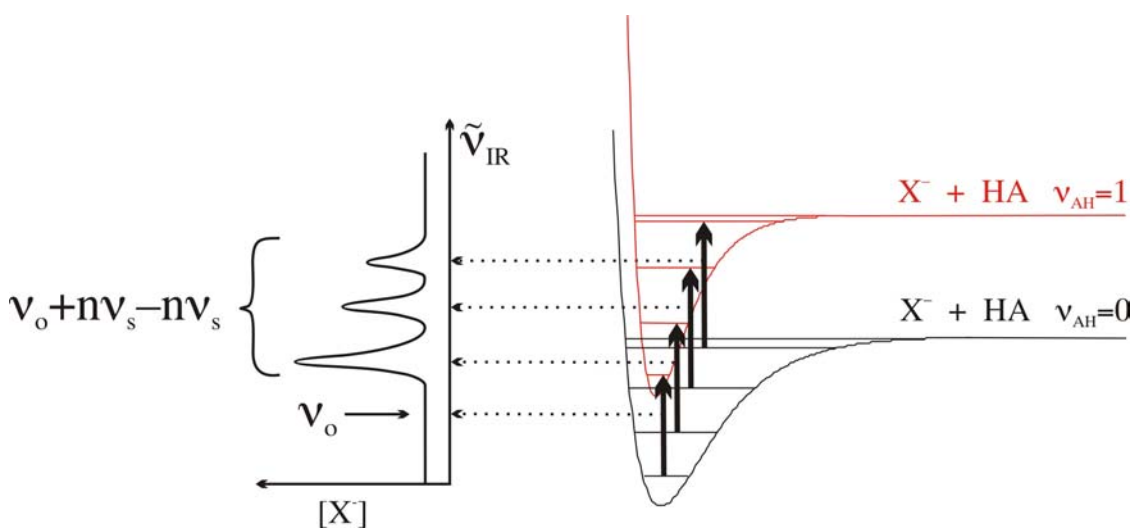
Figure 2.3: *VPS where $D_o^{''} > E_{v_o}$. Hot band transitions of the form $v_{AH} + n v_s - n v_s$ that terminate above the dissociation threshold of the complex lead to dissociation to $X^- + HA$ ($v_{AH} = 0$). The upper state potential is deeper, leading to a greater spacing between the stretching energy levels, so that the hot bands are displaced to higher energy with respect to v_o. The form of the spectrum is illustrated to the left. The fundamental transition v_o is not observed.*

To circumvent problems associated with applying VPS to strongly bound clusters, the dissociation of weakly bound 'spy' atoms or molecules can be used to observe an infrared absorption. Vibrational excitation of the core complex leads to loss of the 'spy' atom, thereby producing a detectable fragment ion. The presence of the loosely bound 'spy' is also advantageous as it effectively limits the internal energy that the core cluster ion can possess, eliminating complexes in highly excited stretching and bending states. The clusters' lower internal energy is manifested in reduced hot band congestion in the spectra, the effects of which are further examined in Chapter 3 with respect to the halide-acetylene dimmer complexes.

The 'spy' atom may perturb the core complex, leading to shifts in the vibrational frequencies. However, the magnitude of the perturbation can be determined by successively solvating the complex with more 'spy' atoms while noting the variation of the vibrational frequencies of the core complex. Rare gas atoms are ideal 'spy' atom candidates, as they are attached to the core complex by weak induction forces. Johnson and coworkers have shown that the presence of multiple argon atoms only produces a marginal perturbation in the halide–water complexes.[3] The argon induced vibrational band shift of the bound O–H stretching mode is $\sim +12$ cm^{-1}/Ar atom for F^-–(H_2O).Ar_n (ref. 4), ~ -3 cm^{-1}/Ar atom for I^-–(H_2O).Ar_n (ref. 5), and < 1 cm^{-1}/Ar atom for the Cl^-–(H_2O).Ar_n complexes (ref. 3).

2.1.1 Additional information from VPS
Predissociation rates

Under some circumstances, VPS provides information on the rate of cluster dissociation following *IR* photon absorption. The lifetime of the upper state depends on the strength of the coupling between the excited stretching mode and the dissociation coordinate.[2] An approximate lower limit for the predissociation rate is provided by the observation that dissociation occurs during the ions' flight through the octopole section of the TMS (section 2.2). When rovibrational structure is resolved, the predissociation rate is sometimes obtainable from the linewidths of the transitions. In the absence of laser power broadening, the linewidths are related to the lifetime of the prepared upper state through Heisenberg's uncertainty principle:

$$\tau \Delta E \geq \hbar \,.$$ [6]

which relates the lifetime τ of the upper state to the uncertainty in the energy of the state (ΔE). This relation can also be expressed as:

$$\tau \geq (2\pi c \Delta \tilde{\nu})^{-1} \approx 5.3 ps/cm^{-1} \qquad [7]$$

where $\Delta \tilde{\nu}$ is the rotational line width (full width at half maximum, fwhm). The output of the OPO has a bandwidth of ~ 0.017 cm^{-1}, so that lifetime broadening of the transitions exceeding 0.01 cm^{-1} is discernible, corresponding to predissociation times less than 530 ps.

It is possible that the rotational lines may be Doppler broadened due to a spread in the ions velocities during their transit through the octopole ion guide. The energy of the ion beam while in the octopole is estimated to be 10.0±0.3 eV. This ±0.3eV spread corresponds to a 1.5% spread in ion velocities leading to a Doppler broadening of 0.003 cm^{-1}. This line broadening is negligible compared with the $\sim$0.017 cm^{-1} bandwidth of the OPO light source (Section 2.2.5). The influence of Doppler broadening is shown to be small by considering that linewidths observed for Br$^-$-D$_2$ are limited by the laser bandwidth (Chapter 4, Section 4.3.6).

Cluster binding energies

Occasionally, accurate binding energies can be determined for the smaller complexes from vibrational predissociation spectra displaying rotational resolution. Transitions terminating below a specific upper state J' may be absent, as the absorbed *IR* photon does not provide the complex with sufficient energy to dissociate. The binding energy of the complex is therefore bracketed by the energies of the (v', $J'-1$) and (v', J') levels. An example, discovered in the course of this work, is the Br$^-$–C$_2$H$_2$ complex.

2.2: Experimental apparatus: Tandem mass spectrometer (TMS) and optical parametric oscillator (OPO)

The TMS apparatus, shown in Fig. 2.4, consists of a cluster ion source, primary quadrupole mass filter, octopole ion guide, secondary quadrupole mass filter and ion detector. The components are connected by electrostatic lenses, which focus the ion beam through the apparatus. The TMS ensemble is housed in differentially pumped high vacuum chambers to reduce the operating pressure and limit dissociative collisions between the cluster ions and background gas molecules. Typically, the pressure in the laser/ion beam interaction region is ~ 2 x 10^{-7} Torr.

Cluster ions are produced in the pulsed electron–impact ion source. The desired cluster ions are selected by the primary quadrupole mass filter, are then deflected 90° by the quadrupole deflector, and enter the octopole ion guide collinear with the counter propagating beam of *IR* radiation. When the frequency of the *IR* radiation is resonant with a vibrational transition, the clusters dissociate producing charged and neutral fragments. The charged photofragments are mass selected by the secondary quadrupole mass filter, and sensed with a microsphere plate detector. The spectra are obtained by recording the intensity of ionic fragments as a function of the *IR* photon wavenumber.
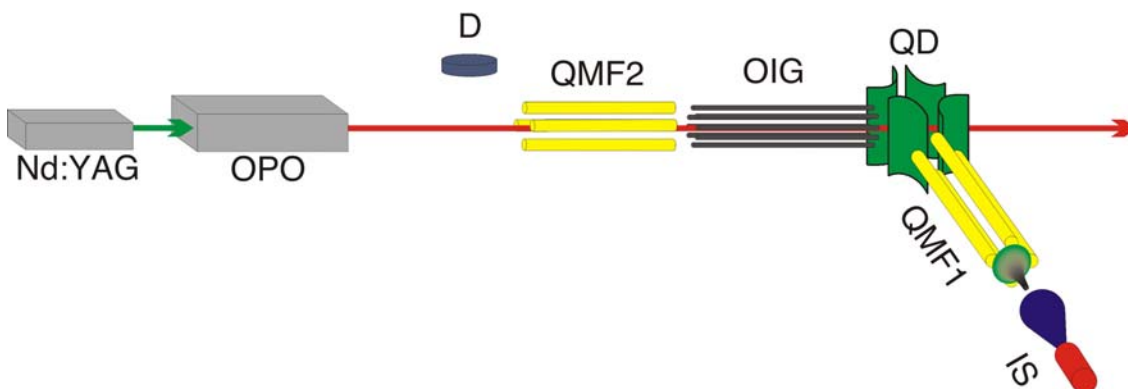

Figure 2.4: *Schematic diagram of the TMS apparatus. The labelled components are the ion source (IS), first and second quadrupole mass filters (QMF1 and QMF2), octopole ion guide (OIG), quadrupole deflector (QD), detector (D), optical parametric oscillator (OPO), and Nd:YAG pump laser (Nd:YAG)*

The following discussion of the TMS apparatus is divided into four sections: cluster ion production, cluster ion selection and beam guiding, ion detection, and the high vacuum pumping regime.

2.2.1: Cluster ion production

The cluster ions are produced in a pulsed electron impact source, shown in Fig. 2.5. The source consists of a pulsed gas nozzle, rhenium filaments as the source of electrons, and a conical skimmer through which the ions are extracted. The body of the source is biased at –40 V, while the conical skimmer is set at ~ –30 V to attract anion clusters through the orifice. The source ensemble is enclosed by an electrostatic cage to

ensure that external electric fields do not affect the plasma. Immediately following the skimmer, a stack of three electrostatic lenses guide the ions into the primary quadrupole mass filter.
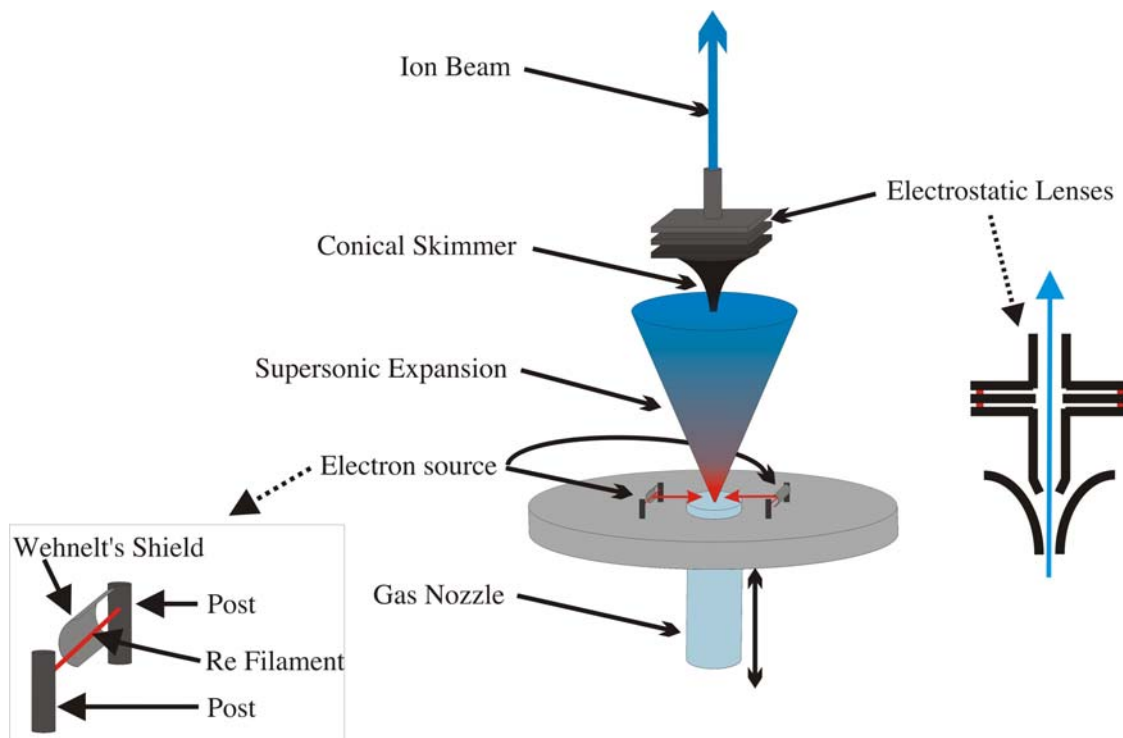
Figure 2.5: *The cluster ion source. The nozzle can be moved to adjust the separation between the orifice and the electron beams.*

Gas is adiabatically expanded from the nozzle into the vacuum and forms a supersonic expansion. The gas cools as it expands, reducing the rotational and vibrational temperatures of the gas to a few degrees K.[6] Low temperatures are vital for forming and stabilising the loosely bound complexes. The expanded gas mixture consists of three components: a halide anion precursor, a ligand gas, and an argon or helium carrier gas. As an example, a gas mixture comprised of 2% acetylene in helium with traces of carbon tetrachloride (CCl_4) is used to produce $Cl^- - (C_2H_2)_n$ clusters. To form larger clusters, with more neutral molecules attached to the anion, the percentage of acetylene in the gas mixture is increased. The halide ion precursors used are NF_3 for F^-, CCl_4 for Cl^-, CH_2Br_2 for Br^-, and CH_3I for I^-. The CCl_4, CH_2Br_2, and CH_3I samples are liquid at room temperature, while NF_3 is gaseous and supplied as a 2% mixture in argon.

The liquid samples are held in a stainless steel bubbler which is repeatedly frozen, evacuated, and thawed to remove dissolved oxygen and nitrogen (freeze–pump–thaw cycle). The sample holder is chilled in an ice/water/salt or dry ice/acetone slurry to control the vapour pressure of the halide anion precursor in the gas mixture. The mixture of the carrier gas and ligand gas is bubbled through the liquid sample to produce the final gas mixture with less than 1% of the halide anion precursor.

The purity of the gas mixture is an important factor for reliable production of cluster ions. Trace impurities, especially unwanted halide ion precursors, remaining in the gas lines from previous experiments can greatly affect production of the desired anion complexes. Saturation of the gas mixture with the halide precursor also leads to unstable production. To remove impurities, the gas lines are repeatedly flushed with argon. The o–ring sealing the gas nozzle is also replaced occasionally, as the halide precursors absorb into this and leak out over time. An inline trap, consisting of a chilled coil of gas line is used to remove water vapour, another contaminant that interferes with cluster production

Electrons intersect the gas expansion, creating a plasma. Cations and anions, present in the plasma, subsequently undergo clustering reactions with neutral atoms and molecules. Electrons are produced via thermionic emission from two rhenium wire filaments (0.2 mm diameter) situated on opposite sides of the nozzle orifice. The filaments are housed in boxes with slits. A pulsed negative voltage is applied to the filaments, and accelerates the electrons through the slits and into the gas expansion. The acceleration voltage applied to the filaments determines the energy of the emitted electrons. The timing and width of the voltage pulse to the filaments is adjusted to temporally overlap the electron beams with the pulsed gas expansion. Cluster production is generally optimised by applying voltages of –200 to –500 V, approximately 10–100 μs after the gas nozzle opens. Due to their proximity to the gas expansion, the filaments degrade rapidly, and usually provide ~ 20 hours of operation.

Cluster production is optimised for small separations between the nozzle orifice and electron beams. This implies that the dominant formation process involves dissociative electron attachment to the halide ion precursor to form the halide anion,[7] followed by three body aggregation reactions to form cluster ions:[8]

$$CCl_4 + e^-(slow) \rightarrow (CCl_4^-)^* \rightarrow Cl^- + CCl_3$$

$$then \tag{1}$$

$$Cl^- + nL + M \rightarrow Cl^- - (L)_n + M$$
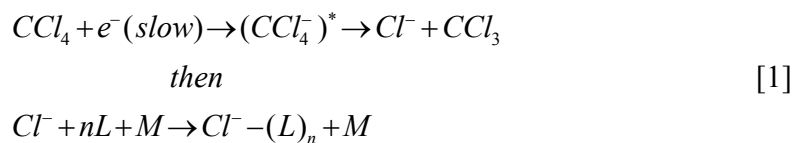
Here, L is the coordinating ligand, and M is a third body which removes excess energy from the nascent complex via collision. Alternatively, if cluster production was optimised at larger separations between the nozzle orifice and electron beams, the formation process would most likely involve dissociative electron attachment to large preformed neutral clusters, followed by solvent molecule evaporation:

$$CCl_4 + nL \rightarrow CCl_4 - L_n + e^-(slow) \rightarrow (CCl_4 - L_n)^{-*} \rightarrow Cl^- - (L)_{n-m} + mL + CCl_3 \tag{2}$$

2.2.2: Cluster ion selection and ion beam guiding

Selection of the parent and photo–fragment cluster ions is achieved using quadrupole mass filters (QMFs). The ions are guided between components of the TMS by stacks of electrostatic lenses, and deflected 90° after the primary QMF by a quadrupole deflector to become collinear with the laser beam. To maximise the spatial overlap of the laser and ion beams, the cluster ions are contained within an octopole ion guide.

Quadrupole mass filters

The primary and secondary QMFs consist of four parallel, circular cross section rods (19 mm diameter, Fig. 2.4), with opposite rods electrically connected. An electrical potential $\varphi(t) = U + V\cos(2\pi f t)$ is applied to one set of rods, where U is a dc voltage, and V is the peak amplitude of a RF voltage with frequency f. To the other set of rods the same potential, but with opposite sign, is applied. The applied potentials affect the trajectory of the ions as they pass though the filter. Ions with the correct mass to charge ratio (m/z) oscillate stably as they travel through the filter, while the remaining ions have unstable trajectories and are ejected. The transmitted mass is determined by U and V, and f. The potentials are supplied by a quadrupole power supply (Model 011–1, Extrel), which varies U and V simultaneously, while holding f constant. More detailed descriptions of the theory for quadrupole filter operation are given in refs. 9–12.

The four rods are also biased with a common dc voltage that is more positive than the source potential. This common voltage controls the kinetic energy of the ions, and hence affects the mass resolution of the filter. If the ions pass too quickly through the filter, adequate mass selection is not achieved and the resolution is diminished. The size of the clusters that can be investigated is limited by the mass range of the quadrupole filters (0–220 amu).

Quadrupole deflector

After passing through the primary QMF, the ion beam is deflected by 90° with an electrostatic quadrupole deflector[13, 14] consisting of four electrodes shown schematically in Fig. 2.6. The potentials applied to the electrodes control the trajectory of the ion beam, steering it from the primary QMF into the octopole ion guide. Top and bottom electrode plates (not shown) are used to control the vertical displacement of the ion beam.
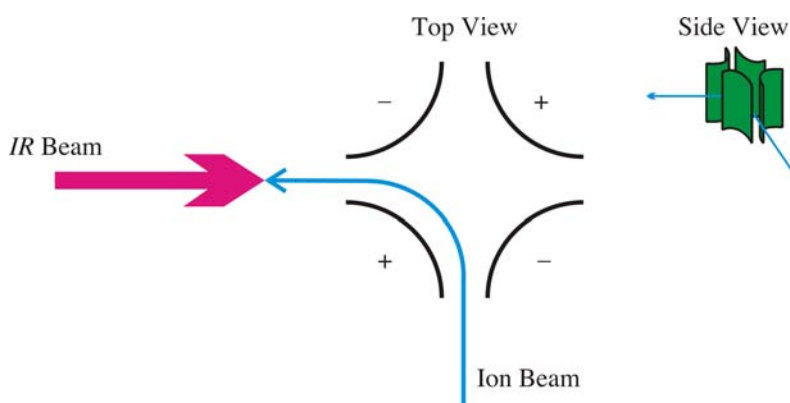
Figure 2.6: Schematic of the quadrupole deflector. After the primary QMF, the ion beam is deflected 90° and enters the octopole ion guide collinear with the IR beam.

Octopole ion guide

The octopole ion guide consists of eight parallel rods (length = 60 cm, rod diameter = 3.2 mm, Fig. 2.4), with alternate rods electrically connected. The two sets of rods are connected to an air spaced copper tube coil, forming an *LC* circuit with resonant frequency of ~ 10 MHz. The copper coil connected to the octopole is the secondary coil of a transformer, in which the primary coil is a single turn of copper tubing that is connected via a matching box (Antenna Tuner, model FC–700, Yaesu Musen) to a commercial *RF* transceiver (HF Transceiver, model FT–840, Yaesu Musen).

The 10 MHz *RF* potential applied to the rods produces an effective radial trapping potential that serves to contain the ion beam, improving its spatial overlap with the *IR*

radiation. A common dc voltage is applied to the eight rods, to control the kinetic energy of the ions as they pass through the ion guide. This allows one to slow the ions, maximising the temporal overlap of the ion beam with the *IR* radiation. Travel times of ~ 100 μs are achieved for ions of mass 60 amu by applying a voltage which is ~ 10 V more positive than the source potential (~ –40 V). A detailed description of octopole design and theory of operation can be found in ref. 15.

2.2.3: Ion detection

The detector assembly (Fig. 2.7) has three main components, a microsphere plate (diameter = 32.8 mm, El–Mul Technologies), scintillator disc and photomultiplier (Hamamatsu, R6094). A glass rod guides photons from the scintillator to the photomultiplier. A repeller plate is situated below the detector stack.
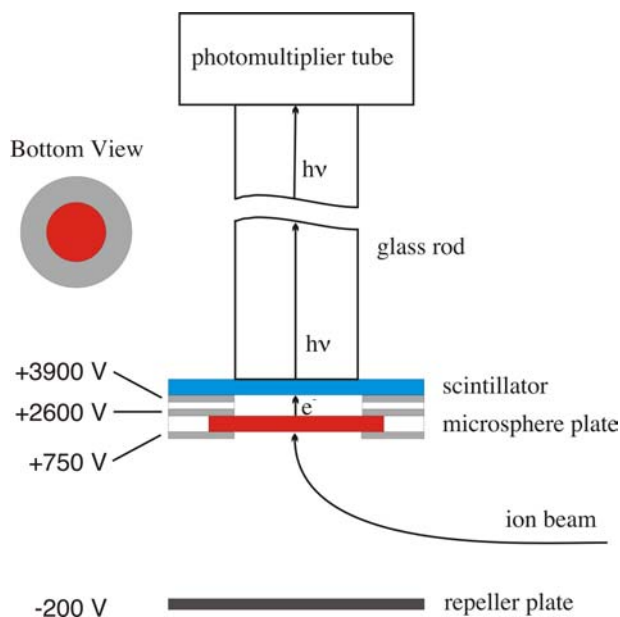
Figure 2.7: *Schematic of the ion detector. Voltages are applied to the electrodes (grey regions). The white regions are electrical insulators.*

Ions transmitted by the secondary QMF are attracted to the front surface of microsphere plate, which is set at a positive potential (+750 V). In addition, a repeller plate biased at –200 V is situated below the front face to direct the negative ions upwards. The ions impinge upon the front face of the microsphere plate, emitting electrons which are attracted through the plate by the larger positive potential applied to the back face. A cascade of electrons reaches the back face for each ion impinging on the front surface.

The electrons are accelerated towards the phosphor impregnated scintillator disc, which is maintained at a larger positive potential. Electrons striking the scintillator disc produce photons that are channelled through the glass rod to the photo–multiplier. The detector sensitivity is controlled by varying simultaneously the voltages applied to the scintillator disc and the back face of the microsphere plate.

The output of the photomultiplier is sent without further amplification to a digital oscilloscope, and a boxcar integrator (SR250 Gated Integrator, Stanford Research Systems). The averaged output (usually averaged over 30 or 100 triggers) is transferred via a GPIB computer interface (SR245, Stanford Research Systems) to a G4 Macintosh computer.

2.2.4 High vacuum pumping regime

The TMS is housed within a series of differentially pumped vacuum chambers. The pumping regime is illustrated in Fig. 2.8.
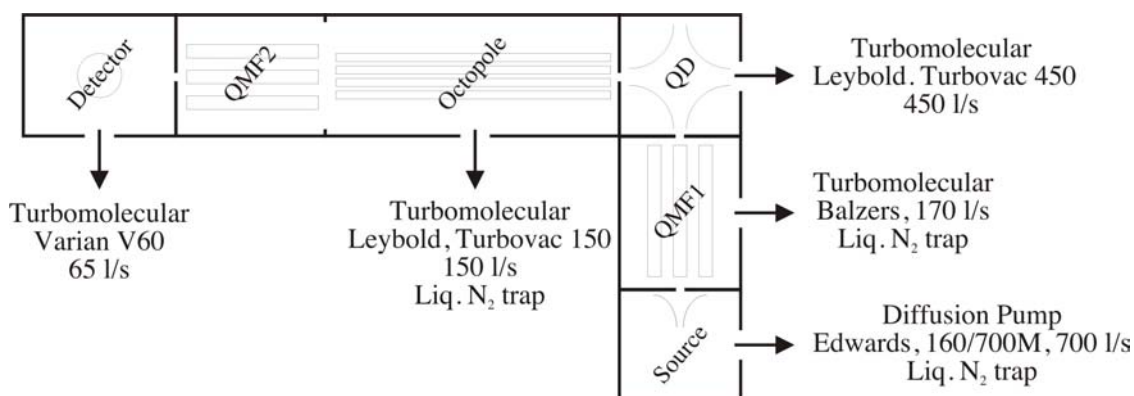
Figure 2.8: *High vacuum pumping regime of the TMS apparatus.*

The ion source chamber is evacuated by a rotary backed, high throughput diffusion pump (Edwards, 160/700M, 700 l/s) used in conjunction with a liquid nitrogen condensation trap. This pumping regime results in background pressures of $\sim 1 \times 10^{-7}$ Torr, while pressures of $\sim 2 \times 10^{-4}$ torr can be maintained during cluster ion source operation. The remaining chambers of the apparatus are separated by baffles, with access provided for the electrostatic lenses which guide the ion beam. These chambers are evacuated by rotary backed turbomolecular pumps (details in Fig. 2.8). The pressure in

the octopole section of the TMS, where the *IR* radiation overlaps the ion beam, is typically less than 2 x 10^{-7} Torr during ion source operation.

2.2.5: Infrared light source. The optical parametric oscillator (OPO)

Infrared radiation is generated by an optical parametric oscillator (OPO, Mirage 3000, Continuum) pumped by a Nd:YAG laser (Powerlite 8000, Continuum). The OPO system employs optical parametric oscillation and optical parametric amplification to convert the Nd:YAG fundamental and second harmonic (1064 and 532 nm) to narrow bandwidth (0.017 cm^{-1}) infrared radiation that is continuously tuneable from 1.45 to 4.0 μm. Potassium titanyl phosphate (KTP) crystals are employed for the parametric conversion, and are angle tuned. The laser system operates in a pulsed mode (20 Hz), with pulse duration of 4–6 nanoseconds.

The narrow band optical parametric oscillator (pumped by 532 nm) operates in the near infrared and establishes the single–longitudinal–mode bandwidth and tunability of the system. Two parametric stages follow the oscillator (pumped by 532 nm and 1064 nm respectively) and successively convert the pump radiation to the 1.45–2.1 μm spectral region, and then to the combined 1.45–2.1 μm and 4.0–2.1 μm spectral regions. The output consists of two photons whose energy sum to that of the final stage 1064 nm pump photon.

The output beam from the OPO therefore has four components: 532 nm radiation, 1064 nm radiation, and the tuneable 1.5 μm and 3.0 μm infrared radiation. A germanium wafer is used to filter out the 1064 nm, 532 nm, and 1.5 μm components, while allowing the tuneable 3 μm radiation to pass through the TMS. The OPO output beam is collimated by two gold plated spherical mirrors (0.75 m focal length), which are adjusted to optimise overlap of the *IR* and ion beams. The *IR* radiation enters and exits the TMS through sapphire windows.

A small portion of the OPO oscillator output is directed to a Fabry–Perot etalon (free spectral range = 0.22 cm^{-1}). The resulting interference pattern, consisting of concentric circular fringes, is displayed on a monitor. When the wavelength of the oscillator is scanned, the circular fringes change circumference, spreading either outwards or contracting inwards depending on the scan direction. A photodiode attached

to the screen of the display monitor records a section of each circular fringe as it sweeps past. The output from the photodiode, which ideally consists of equally spaced peaks, is used to ensure that the oscillator is scanning smoothly.

Determination of the *IR* wavelength is achieved by measuring the output from the first stage of the OPO system (λ_{osc} = 710–840 nm) with a wavemeter (Fizeau Wavelength Meter, New Focus, Model 7711). The wavelength of the Nd:YAG second harmonic was determined to be 532.217 nm. The wavenumbers of the infrared outputs of the OPO system are calculated via the following relations:

$$\tilde{\nu}_1 = (\frac{1}{532.217} - \frac{1}{\lambda_{osc}}) \times 10^7 \ cm^{-1} \qquad [4]$$

$$\tilde{\nu}_2 = (\frac{1}{\lambda_{osc}} - \frac{1}{1064.434}) \times 10^7 \ cm^{-1} \qquad [5]$$

where $\tilde{\nu}_1$ and $\tilde{\nu}_2$ are the wavenumbers of the signal and idler infrared photons, and λ_{osc} is the wavelength (in nm) of the oscillator output. The wavenumbers of the (ro)vibrational transitions are adjusted to account for the Doppler shift arising from the ions' kinetic energy in the octopole section of the TMS.

2.3: Data collection protocol

Data collection is controlled by the graphical programming software LabVIEW (Version 6.0, National Instruments), operating on a Macintosh G4 processor. A LabVIEW virtual instrument (VI) was developed to control data acquisition. A flow chart describing the major operations of the VI is shown in Fig. 2.9. The repetition rate of the data collection loop can be controlled, and is usually set at one cycle per second. The VI allows the user to pause the scan to optimise the laser power and parent cluster ion production.
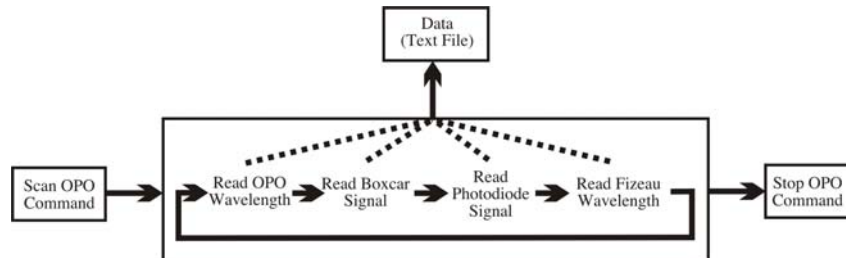
Figure 2.9: *Flow chart describing the data collection program. The output from the program is a text file, shown in Table 2.1.*

The data collection routine commences with a command to scan the OPO laser system. Following this, the main data collection loop is enacted. The first step in the loop is to retrieve a rough estimate of the infrared wavelength from the OPO control computer. The toggled and averaged output (averaged over 30 or 100 triggers) of the SR250 Gated Integrator is then transferred via the SR245 Computer Interface. This signal corresponds to the photo–fragment ion intensity. The next stage is to record the signal from the etalon fringe photodiode. The final step in the data collection loop is to record the OPO oscillator wavelength from the Fizeau wavemeter. The data from each loop is stored in an array. The scan is completed by sending a command to the OPO control computer to stop the OPO scanning. Finally, the data array is saved as a text file, an example of which is in Table 2.1. The data from a number of scans are usually combined, and averaged, to produce the *IR* spectrum.

Table 2.1: *Output from the data collection program. The columns correspond to the approximate OPO oscillator wavelength taken from the OPO control computer, photo–fragment ion intensity, etalon peak intensity, and OPO oscillator wavelength measured by the Fizeau wave meter.*

OPO wavelength (nm)	Ion Intensity (arb. units)	Etalon Intensity (arb. units)	Fizeau wavelength (nm)
746.707	0.520	0.088	743.791
746.706	0.450	0.107	743.791
746.706	0.520	0.132	743.791
746.705	0.770	0.161	743.791
746.705	0.350	0.195	743.790
746.705	0.200	0.229	743.790
746.705	0.070	0.244	743.790
↓	↓	↓	↓
746.082	0.050	0.078	743.167
746.082	0.000	0.078	743.167
746.082	0.050	0.083	743.167

2.4 References:

1. G. E. Ewing, J. Chem. Phys. **72**, 2096 (1980)

2. G. E. Ewing, Faraday Discuss. Chem. Soc. **73**, 325 (1982)

3. J. A. Kelly, J. M. Weber, K. M. Lisle, W. H. Robertson, P. Ayotte and M. A. Johnson, Chem. Phys. Lett. **327**, 1 (2000)

4. P. Ayotte, J. A. Kelly, S. B. Nielsen and M. A. Johnson, Chem. Phys. Lett. **316**, 455 (2000)

5. P. Ayotte, G. H. Weddle, J. Kim and M. A. Johnson, Chem. Phys. **239**, 485 (1998)

6. J. B. Fenn, Int. J. Mass. Spectrom. **200**, 459 (2000)

7. *Electron–molecule interactions and their applications*, edited by L. G. Christophorou (Academic Press, New York, 1984)

8. M. A. Johnson and W. C. Lineberger, in *Techniques For The Study Of Ion–Molecule Reactions*, edited by J. M. Farrar and W. H. Saunders Jr (Wiley, New York, 1988)

9. W. Paul, H. P. Reinhard and U. von Zahn, Z. Physik. **152**, 143 (1958)

10. J. E. Campana, Int. J. Mass Spectrom. Ion Phys. **33**, 101 (1980)

11. E. P. Sheretov, Int. J. Mass. Spectrom. **219**, 315 (2002)

12. E. P. Sheretov, I. V. Philippov, T. B. Karnav, E. V. Fedosov and V. W. Ivanov, Int. J. Mass. Spectrom. **219**, 325 (2002)

13. H. D. Zeman, Rev. Sci. Int. **48**, 1079 (1977)

14. P. R. Mahaffy and K. Lai, Journal of Vacuum Science & Technology, A: Vacuum, Surfaces, and Films **8**, 3244 (1990)

15. D. Gerlich, Adv. Chem. Phys. **82**, 1 (1992)

Chapter 3: The Halide–Acetylene Anion Complexes

3.1 Introduction

The work detailed in this chapter concerns the gas phase complexes formed from halide anions and neutral acetylene molecules. The discussion aims to address the following questions. What is the nature of the bonding interaction between the halide anion and an acetylene molecule? What effect does the halide anion have on the frequencies and *IR* intensities of the acetylene molecule's fundamental vibrations? How does this effect vary as the size of the halide is increased and as more acetylene molecules are attached to the halide? And finally, what are the preferred structures for the larger clusters?

The halide–acetylene complexes have received prior theoretical and experimental attention. Early *ab initio* studies at the SCF/3–21+G and SCF/4–31+G levels predicted a linear hydrogen bonded structure for the F^-–C_2H_2 dimer.[1–3] More recent higher level calculations performed at the CCSD(T) level for Cl^-–C_2H_2, Br^-–C_2H_2, and I^-–C_2H_2 also predicted linear structures and provided vibrational frequencies.[4–6] Rovibrational energy levels have also been calculated for the Cl^-–C_2H_2 complex using an *ab initio* potential energy surface computed at the MP2/aug–cc–pVTZ level.[7] The MP2 *ab initio* potential energy surface suggests that the barrier for traversing from one linear minimum to the other through the repulsive T–shaped structure is much larger than the acetylene rotational constant. This implies that the internal rotation of the acetylene sub unit is essentially quenched and that the complexes are locked into a linear configuration, with only small excursions due to zero point intermolecular bending motions.

Previous *IR* studies of the halide–acetylene complexes using matrix isolation spectroscopy of reaction products between acetylene and cesium–halide salts revealed several absorptions in the 600–3400 cm^{-1} range.[8] The most intense bands for F^-–C_2H_2, Cl^-–C_2H_2, and I^-–C_2H_2 are located at 2873, 3050, and 3182 cm^{-1} respectively. These bands are shifted to lower frequency from the C–H stretches of C_2H_2 and were assigned to the v_3 bound C–H stretch vibration of linear X^-–C_2H_2 complexes. Weaker bands located at 3325 and 3338 cm^{-1} for the F^-–C_2H_2 and Cl^-–C_2H_2 complexes respectively, were assigned to the free C–H stretch mode. Importantly, the matrix vibrational frequencies are likely to be affected by perturbations from co–deposited

Cs$^+$ counterions, the argon matrix, and possibly by other reaction products. In addition, the matrix isolation technique does not allow spectroscopic investigation of larger X$^-$–(C$_2$H$_2$)$_n$ clusters as the number of acetylene units bound to the anion cannot be reliably controlled. These limitations are avoided in the gas phase studies described in this chapter.
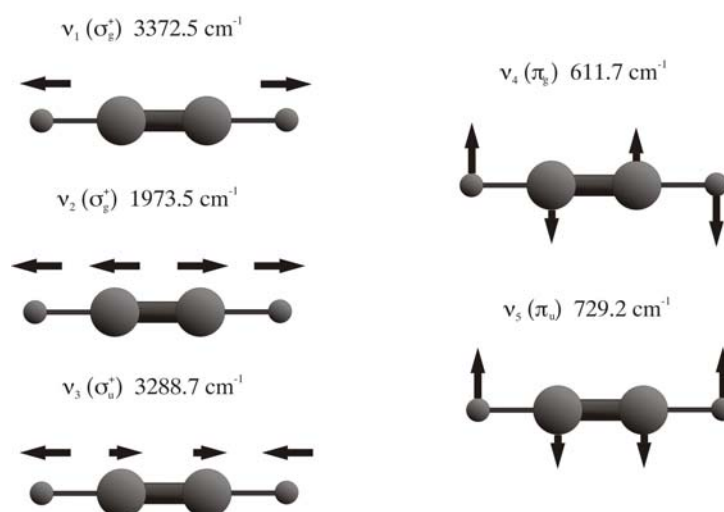
Structural and vibrational properties

The dominant cohesive interactions between a halide anion and C$_2$H$_2$ molecule are the charge–quadrupole and charge–induced dipole forces:[9]

$$V_{lr}(R,\theta) = \frac{Q\Theta}{2(4\pi\varepsilon_o)R^3} \times (3\cos^2\theta - 1) - \frac{1}{2}\frac{Q^2(\alpha_{\parallel}\cos^2\theta + \alpha_{\perp}\sin^2\theta)}{(4\pi\varepsilon_o)^2 R^4} \qquad [1]$$

where Q is the charge on the anion, Θ is the acetylene quadrupole moment, $\alpha_{\parallel}$ and $\alpha_{\perp}$ are the parallel and perpendicular acetylene polarisability components, R is the intermolecular separation, and θ is the angle between the C$_2$H$_2$ internuclear axis and intermolecular bond. The charge–quadrupole and charge–induced dipole interactions both favour linear hydrogen bonded complexes, consistent with the linear geometry predicted from *ab initio* calculations.

It is useful to begin the discussion of the vibrational properties of the halide–acetylene complexes by examining the vibrational modes of the bare acetylene molecule. Acetylene, a linear D$_{\infty h}$ molecule, possesses the modes illustrated in Fig. 3.1.

ν_1 (σ_g^+) 3372.5 cm^{-1}

ν_2 (σ_g^+) 1973.5 cm^{-1}

ν_3 (σ_u^+) 3288.7 cm^{-1}

ν_4 (π_g) 611.7 cm^{-1}

ν_5 (π_u) 729.2 cm^{-1}

Figure 3.1: *Atomic displacements for the five normal vibrational modes of the acetylene molecule. Vibrational frequencies are taken from refs. 10 and 11.*

The modes correspond to the symmetric C–H stretching mode (ν_1 (σ_g^+)), the C≡C stretching mode (ν_2 (σ_g^+)), the antisymmetric C–H stretching mode (ν_3 (σ_u^+)), and the doubly degenerate *trans* and *cis* bending modes (ν_4 (π_g)) and ν_5 (π_u)). Only the *ungerade* ν_3 and ν_5 modes involve a change in dipole moment and are *IR* active.

The local symmetry of the C_2H_2 molecule is reduced from $D_{\infty h}$ to $C_{\infty v}$ in the linear X^-–C_2H_2 complex. There are ten vibrational modes for the complexes (Fig. 3.2) with the three bending modes being doubly degenerate. The modes can be separated into five high frequency modes that principally involve distortions of the acetylene molecule, and two low frequency modes that involve distortion of the halide–acetylene intermolecular bond.
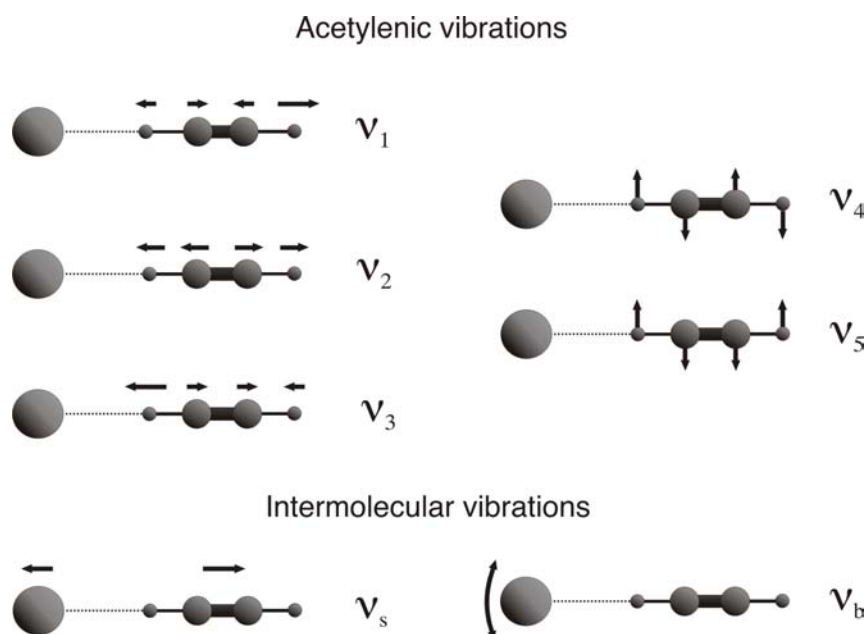
Figure 3.2: *Vibrational modes for a linear halide–acetylene complex. The modes are separated into those that entail distortions of the acetylene molecule, and modes involving distortion of the intermolecular bond. The numbering of the acetylenic modes reflects their parentage in bare acetylene.*

The five high frequency modes of the X^-–C_2H_2 complexes are labelled according to the vibrational mode of C_2H_2 to which they most closely correspond. The ν_1 mode predominantly involves motion of the free or terminal hydrogen and correlates with the *IR* inactive symmetric C–H stretch mode of C_2H_2. The C≡C stretching mode, labelled ν_2, correlates with the *IR* inactive C≡C stretch mode of C_2H_2. The CCSD(T) calculations[4–6] predict that both of these modes become slightly *IR* active and are shifted to lower frequency from the bare acetylene frequencies.

The ν_3 mode of the halide–acetylene complex principally involves motion of the H–bonded C–H group, and correlates with the *IR* active antisymmetric C–H stretch mode of C_2H_2. The CCSD(T) calculations[4–6] predict that association of the acetylene molecule with the halide anion has a profound effect on the ν_3 mode, with an increase in its *IR* intensity and decrease in its frequency. These are characteristic effects for a molecule engaged in a hydrogen bond.[12] The red shift of the ν_3 band is usually indicative of the strength of the intermolecular interaction with a large shift correlating with a strong intermolecular interaction. Indeed, the calculated ν_3 frequencies for $Cl^-–C_2H_2$, $Br^-–C_2H_2$, and $I^-–C_2H_2$ ($\nu_3 = 2877, 2964$ and 3050 cm^{-1}) correlate with the calculated binding energies ($D_e = 3750, 3126$ and 2550 cm^{-1}).[4–6]

The two doubly degenerate bending modes of the acetylene molecule (ν_4 and ν_5) are also affected by the presence of the halide anion, and are predicted to shift to higher frequency since the lateral motion of the shared proton is constrained in the complexes.

The intermolecular stretching and bending modes, labelled ν_s and ν_b respectively, involve distortion of the weak halide–acetylene bond and are expected to be the lowest frequency modes. For $Cl^-–C_2H_2$, $Br^-–C_2H_2$, and $I^-–C_2H_2$, the CCSD(T) calculations of Botschwina *et al* predict intermolecular stretching and bending frequencies of $\nu_s = 153, 117, 95$ cm^{-1} and $\nu_b = 146, 132, 120$ cm^{-1}.[4–6]

Due to the considerations outlined above, the mid–infrared spectra of the halide–acetylene dimers should contain a strong absorption corresponding to excitation of the ν_3 mode and a much weaker absorption due to excitation of the ν_1 mode.

For the larger halide–acetylene clusters, $X^-–(C_2H_2)_n$, the frequency of the ν_3 mode gives information on the cluster structures as the stretching potential for the shared proton is sensitive to the local halide–acetylene bonding environment. If the anion is located in the interior of the cluster, with roughly equivalent acetylene ligands, the spectra should feature a single ν_3 band. If less symmetric solvation structures are preferred, the spectra are expected to be more complex, displaying multiple ν_3 bands arising from inequivalent acetylene ligands.

The remainder of this chapter begins with a brief description of the experimental conditions employed for the production and interrogation of the halide–acetylene complexes. Gas phase mid–infrared spectra of the halide–acetylene dimer

complexes are then presented. Comparisons between spectra of the $X^- - C_2H_2$ and $X^- - C_2H_2.Ar$ complexes allow the ν_3 frequencies for $Cl^- - C_2H_2$, $Br^- - C_2H_2$, and $I^- - C_2H_2$ to be determined. Quantitative structural and energetic details are deduced for the $Br^- - C_2H_2$ complex from the analysis of a spectrum displaying partial rotational structure. Spectra for the larger $X^- - (C_2H_2)_n$ clusters are presented and used to deduce cluster structures. New features observed in spectra of the larger clusters provide evidence for the onset of the second solvation shell and for the existence of multiple isomeric forms.

3.2 Experimental

The halide–acetylene complexes are produced using a gas mixture consisting of traces of the halide ion precursors (NF_3, CCl_4, CH_2Br_2, and CH_3I) in 1:50 C_2H_2:He for the smaller clusters ($n < 5$), and in pure C_2H_2 for the larger clusters ($n \geq 5$). To produce the $Cl^- - C_2H_2.Ar_n$, $Br^- - C_2H_2.Ar$, and $I^- - C_2H_2.Ar$ clusters, gas mixtures consisting of 1:49:50 C_2H_2:He:Ar with traces of the halide anion precursor were employed. A representative mass spectrum of $Br^- - (C_2H_2)_n$ clusters produced by the ion source is shown in Fig. 3.3. Species containing bromide are conspicuous from the 1:1 isotope abundance of ^{79}Br:^{81}Br.
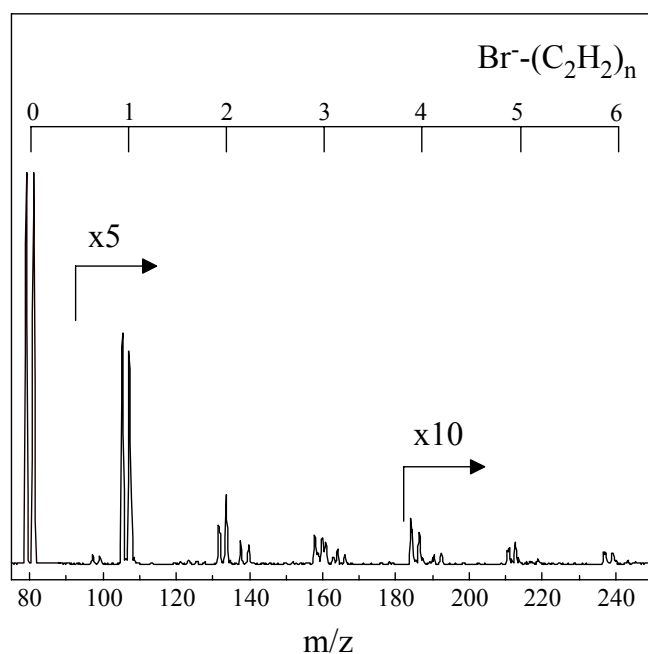

Figure 3.3: *Mass spectrum of $Br^- - (C_2H_2)_n$ clusters produced from 1:50 C_2H_2:He with traces of CH_2Br_2. Also apparent are clusters containing acetone, $Br^- - ((CH_3)_2CO).(C_2H_2)_n$. Impurity acetone is present in the C_2H_2 gas.*

3.3 Halide–acetylene dimer complexes

IR spectra for the Cl^-–C_2H_2, Br^-–C_2H_2, and I^-–C_2H_2 dimer complexes are presented in Fig. 3.4. Spectra of the analogous argon solvated complexes, X^-–$C_2H_2.Ar$, are presented in Fig. 3.5. Due to the range of the OPO *IR* light source (> 2500 cm^{-1}) no transitions were observed for the F^-–C_2H_2 complex. In any case it is likely that an *IR* photon with energy less than 2500 cm^{-1} is insufficient to dissociate the F^-–C_2H_2 complex which is predicted to be quite strongly bound ($D_e \sim 7000$ cm^{-1}; ref. 1).
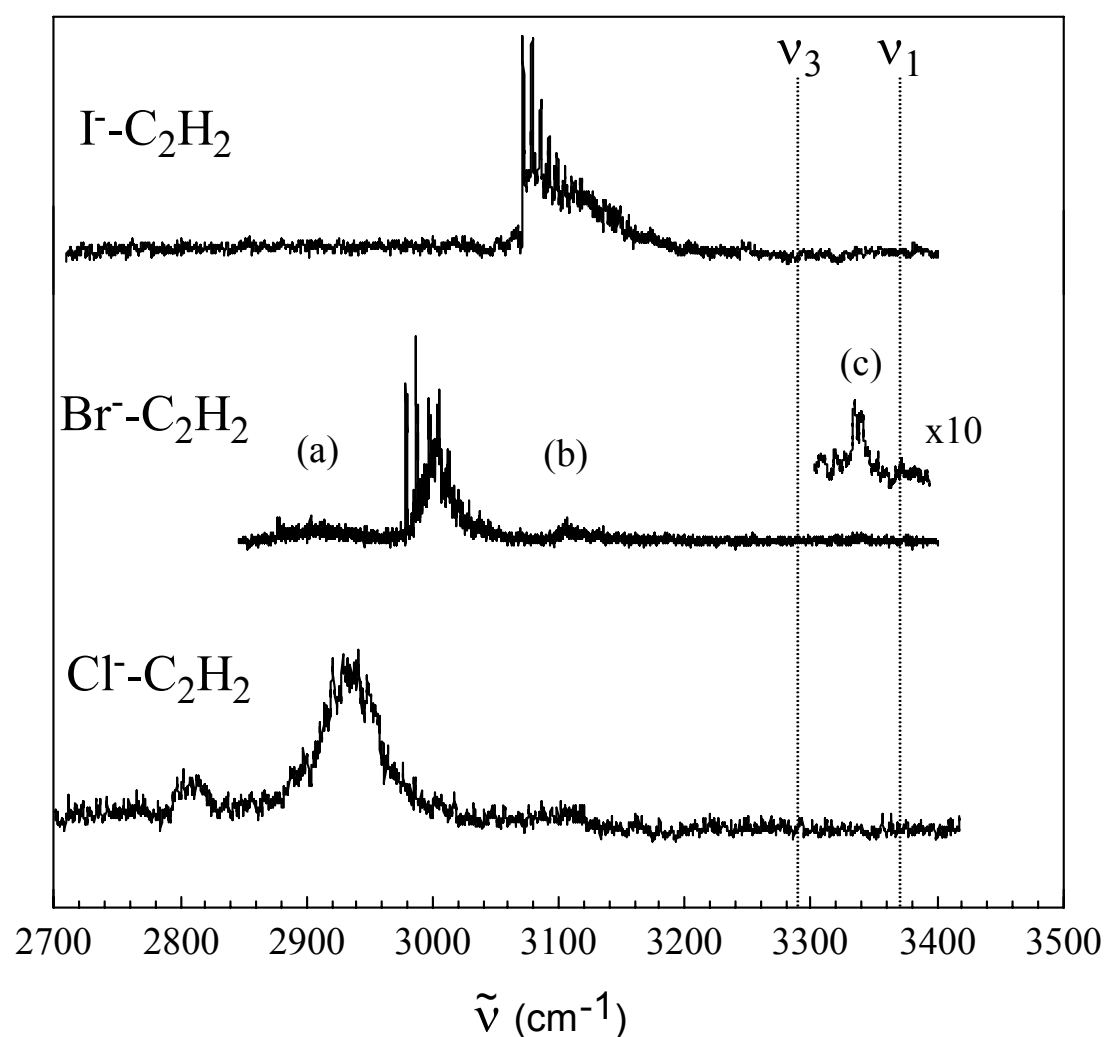
Figure 3.4: *Infrared spectra of $^{35}Cl^-$–C_2H_2, $^{79}Br^-$–C_2H_2, and I^-–C_2H_2 dimers. Frequencies of the symmetric v_1 and antisymmetric v_3 C–H stretches of C_2H_2 are indicated by the dotted lines.[10, 11] Bands marked (a) and (b) in the Br^-–C_2H_2 spectrum are assigned to difference and combination tones involving the intermolecular modes, eg. $v_3 \pm v_{s/b}$. The band marked (c) is assigned to the v_1 free C–H stretch mode of Br^-–C_2H_2.*
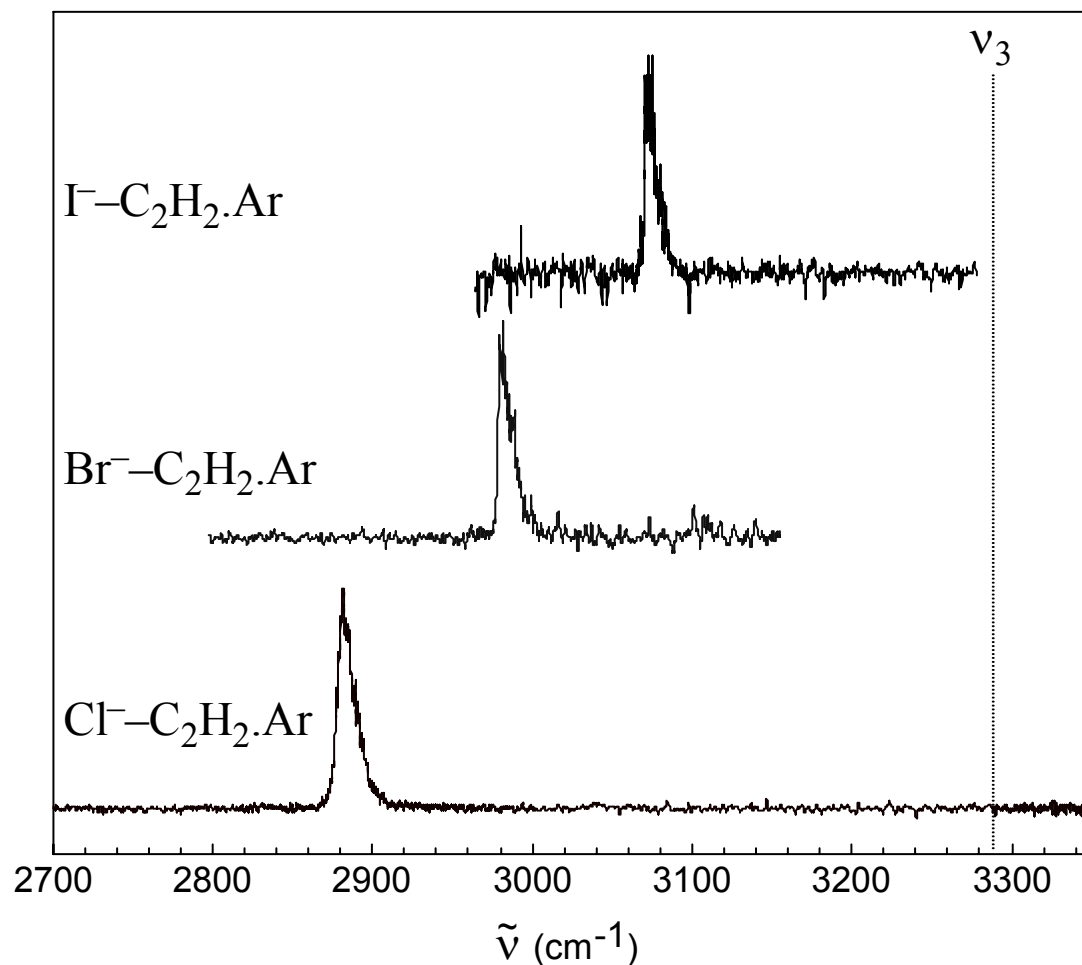
Figure 3.5: *Infrared spectra of $^{35}Cl^{-}$–C_2H_2.Ar, $^{79}Br^{-}$–C_2H_2.Ar, and I^{-}–C_2H_2.Ar complexes recorded by monitoring the intensity of the X^{-}–C_2H_2 fragment. The frequency of the antisymmetric v_3 stretch of C_2H_2 is indicated by dotted line.[11]*
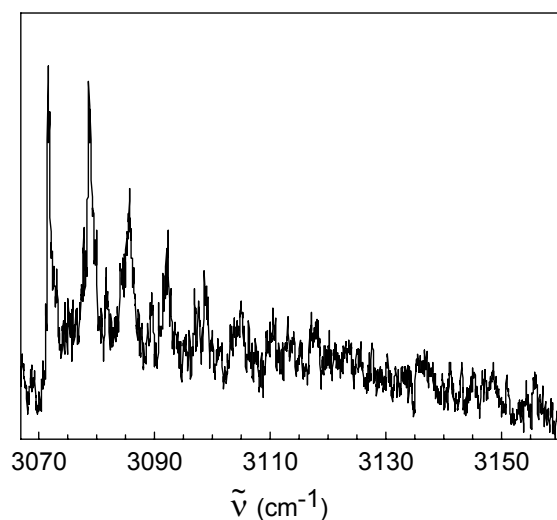
3.3.1 Band assignments

The spectra of the X^{-}–C_2H_2 and X^{-}–C_2H_2.Ar complexes are dominated by an intense band that is shifted to lower frequency from the antisymmetric and symmetric C–H stretching modes of the bare acetylene molecule (3288.7 and 3372.5 cm^{-1} respectively; refs. 10 and 11). The band, which occurs at 2882, 2982, and 3075 cm^{-1} for the Cl^{-}–C_2H_2.Ar, Br^{-}–C_2H_2.Ar, and I^{-}–C_2H_2.Ar complexes, is assigned to the v_3 mode which principally involves stretching motion of the H–bonded C–H group. The vibrational red shift of the band constitutes compelling evidence that the complexes adopt linear structures, as predicted by *ab initio* calculations.[10, 11] The X^{-}–C_2H_2 and X^{-}–C_2H_2.Ar spectra are similar for $X^{-} = Br^{-}$ and I^{-}, however for Cl^{-} there are distinct differences, the origin of which will be discussed shortly.

An extremely weak band is observed at 3340 cm^{-1} in the spectrum of the Br^{-}–C$_2$H$_2$ dimer. This band is assigned to the ν_1 mode, which involves motion of the terminal hydrogen. This assignment is supported by the CCSD(T) calculations of Botschwina *et al*,[4] which predict a frequency of 3354 cm^{-1} and an *IR* intensity which is 2% that of the ν_3 band. The corresponding ν_1 transition was not detected in the Cl^{-}–C$_2$H$_2$ and I^{-}–C$_2$H$_2$ spectra due to poorer S/N ratios.

Two other weak bands are observed in the Br^{-}–C$_2$H$_2$ dimer spectrum (marked (a) and (b) in Fig. 3.4). The band at 3105 cm^{-1}, displaced by +127 cm^{-1} from the ν_3 band, is assigned to a combination of ν_3 and one of the two intermolecular modes ($\nu_3 + \nu_s$ or $\nu_3 + \nu_b$). The broad hump to lower energy from ν_3 (centred at 2910 cm^{-1}) is most probably due to overlapping hot bands such as $\nu_3 - \nu_s$, $\nu_3 + \nu_s - 2\nu_s$, $\nu_3 - \nu_b$, $\nu_3 + \nu_b - 2\nu_b$ etc.

3.3.2 Form of the ν_3 bands

The ν_3 bands of Br^{-}–C$_2$H$_2$ and I^{-}–C$_2$H$_2$ feature a sharp onset to lower energy which is characteristic of a P–branch head, implying that excitation of the shared proton leads to a contraction and stiffening of the X^{-}–C$_2$H$_2$ intermolecular bond. This behaviour is typical for proton–bound ionic complexes and has been observed for other cation and anion systems.[13–17] Both spectra also exhibit a series of sharp peaks extending to higher energy separated by 5–7 cm^{-1} for I^{-}–C$_2$H$_2$, and 7–8 cm^{-1} for Br^{-}–C$_2$H$_2$ (wavenumbers for these transitions are given in Appendix 1). An expanded view of the ν_3 band region for I^{-}–C$_2$H$_2$ is shown in Fig. 3.6. The regular spacing of the peaks, and the fact that they are absent in the spectra of the argon solvated complexes (Fig. 3.5), suggest that they may be due to a sequence of vibrational hot bands involving the intermolecular vibrations (eg., $\nu_3+\nu_s-\nu_s$, $\nu_3+\nu_b-\nu_b$, $\nu_3+\nu_s+\nu_b-\nu_s-\nu_b$).

Figure 3.6: *Infrared spectrum of the I^{-}–C$_2$H$_2$ over the 3070–3160 cm^{-1} range illustrating sharp peak structure extending to higher energy.*

$\tilde{\nu}$ (cm^{-1})

A schematic representation of the hot band transitions involving the intermolecular stretch (ν_s) is given in Fig. 3.7. The lower and upper potential energy curves represent respectively, a halide ion interacting with an acetylene molecule with zero and one quanta in the ν_3 vibrational mode. The energy levels supported by the curves correspond to the intermolecular stretching levels ($n\nu_s$). The appearance of the P–branch head in the spectra implies that the excited state potential energy curve is deeper, narrower, and has a shorter intermolecular separation than the ground state curve. The vibrational hot band transitions $\nu_3+\nu_s-\nu_s$, $\nu_3+2\nu_s-2\nu_s$... are therefore displaced to higher energy with respect to the ν_3 transition, consistent with the structure observed in the spectra. Differences between ground and excited state frequencies should be small, leading to closely spaced hot bands. In the case of the I^-–C_2H_2 complex, the CCSD(T) calculations performed by Botschwina *et al*[4] predict spacings for the $\nu_3+n\nu_s-n\nu_s$ sequence band series that match the experimental spacings to within ± 0.7 cm^{-1}.

$X^- + C_2H_2$ ($\nu_3 = 1$)

$X^- + C_2H_2$ ($\nu_3 = 0$)

X^---- C_2H_2 separation
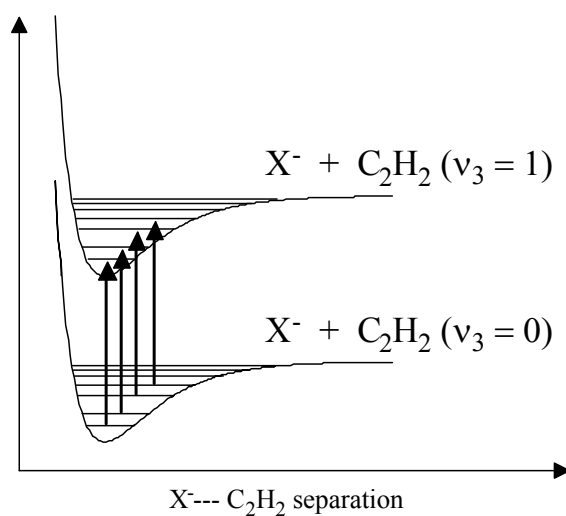
Figure 3.7: *Representation of the X^-– C_2H_2 ground and excited state potential energy curves explaining the hot band structure seen in the Br^- –C_2H_2 and I^-–C_2H_2 spectra. Energy levels correspond to the intermolecular stretch with the transitions being ν_3, $\nu_3+\nu_s-\nu_s$, $\nu_3+2\nu_s-2\nu_s$, $\nu_3+3\nu_s-3\nu_s$, and $\nu_3+4\nu_s-4\nu_s$.*

An alternative though less satisfactory explanation for the series of sharp peaks is that they correspond to a vibrational progression in either the intermolecular stretching or bending modes (eg, $\nu_3+\nu_s$, $\nu_3+2\nu_s$, $\nu_3+3\nu_s$ or $\nu_3+\nu_b$, $\nu_3+2\nu_b$, $\nu_3+3\nu_b$ etc.). This seems unlikely for two reasons. Firstly, the separation between peaks (5–10 cm^{-1}) is much smaller than the anticipated frequencies of the intermolecular stretching and bending vibrations. Botschwina *et al*[4] have calculated intermolecular frequencies of $\nu_s = 119$ cm^{-1} and $\nu_b = 132$ cm^{-1} for Br^-–C_2H_2 and frequencies of $\nu_s = 95$ cm^{-1} and $\nu_b = 120$ cm^{-1} for I^-–C_2H_2. Experimental values in the 100–300 cm^{-1} range have been

observed for ν_s and ν_b in spectroscopic studies of similar proton bound cation complexes.[18, 19] The assignment to a vibrational progression is also questionable in light of the regularity in the peak spacing. It is unlikely that such a regular spacing could be associated with transitions involving anharmonic intermolecular vibrations.

3.3.3 Cl⁻–C₂H₂: Too strongly bound for VPS?

The sharp band onset and progression of narrow peaks observed for the Br⁻–C₂H₂ and I⁻–C₂H₂ complexes are not evident in the spectrum of Cl⁻–C₂H₂ (Fig. 3.4). Instead, two broad bands occur in the 2750–3050 cm^{-1} region. The symmetric profile of the more intense band suggests that it may be composed of overlapping hot bands. In contrast, the spectrum of Cl⁻–C₂H₂.Ar (Fig. 3.5) contains a single narrow band situated midway between the two bands seen for Cl⁻–C₂H₂. It seems likely that the binding energy of Cl⁻–C₂H₂ exceeds that of the absorbed *IR* photon, and dissociation can only occur for complexes already possessing sufficient internal energy to make up the deficit. The calculations of Botschwina *et al*,[5] which indicate that D_o~3600 cm^{-1} and the ν_3 frequency is 2877 cm^{-1}, support this contention. The Cl⁻–C₂H₂ VPS spectrum therefore does not display the fundamental ν_3 transition.

To have confidence in the ν_3 value for Cl⁻–C₂H₂ obtained from the Cl⁻–C₂H₂.Ar spectrum, it is necessary to investigate the perturbation caused by the attached Ar atom. To this end, spectra of the Cl⁻–C₂H₂.Ar₁ and Cl⁻–C₂H₂.Ar₂ complexes were recorded, and are presented in Fig. 3.8. The shift of the ν_3 band is ~ +6 cm^{-1}/Ar atom, demonstrating that the presence of the argon atom(s) has minimal impact on the ν_3 vibrational mode. Extrapolation of the ν_3 frequencies obtained from the spectra of the Cl⁻–C₂H₂.Arₙ complexes establishes the ν_3 frequency for the Cl⁻–C₂H₂ core complex as 2876 ± 5 cm^{-1}. This agrees reasonably well with the predicted frequency of 2843 cm^{-1} from the rovibrational calculations of Meuwly *et al*,[7] and compares extremely well with the predicted frequency of 2877 ± 10 cm^{-1} from CCSD(T) calculations of Botschwina *et al*.[5]
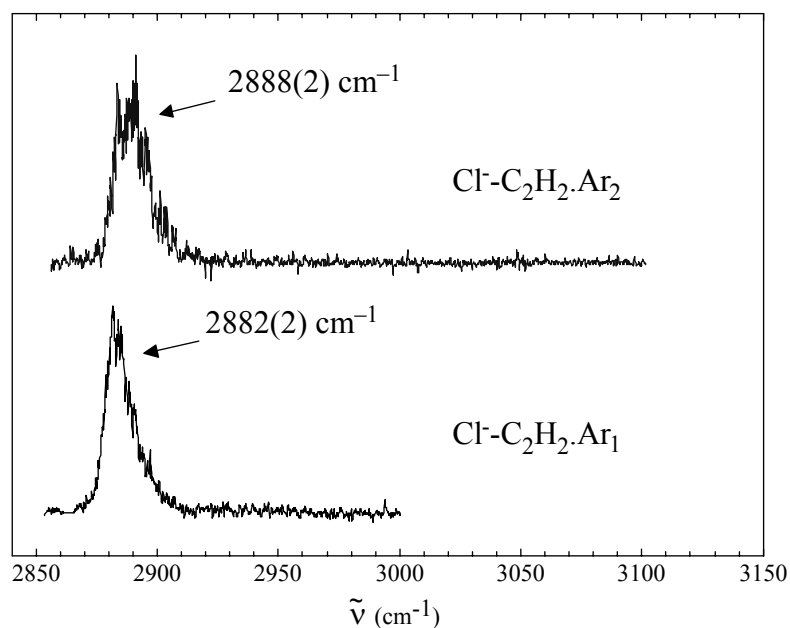
Figure 3.8: *Infrared spectra of the Cl^-–$C_2H_2.Ar_n$ complexes with n = 1–2. The prominent peak shown is the ν_3 stretching band of the core Cl^-–C_2H_2 complex.*

The small argon induced band shift is consistent with the results of analogous studies on the argon solvation of the gas phase halide–water complexes performed by Johnson and coworkers. In these systems the halide is bound quite strongly to the water molecule through a single hydrogen bond, forming an asymmetric C_s structure. The argon induced vibrational band shift of the bound O–H stretching mode is ~ +12 cm^{-1}/Ar atom for F^-–$(H_2O).Ar_n$,[20] ~ –3 cm^{-1}/Ar atom for I^-–$(H_2O).Ar_n$,[21] and < 1 cm^{-1}/Ar atom for the Cl^-–$(H_2O).Ar_n$ complexes.[22]

3.3.4 ν_3 band shifts

The magnitude of the ν_3 vibrational band shift depends on the identity of the halide anion, decreasing in the order $Cl^- > Br^- > I^-$ ($\Delta\nu_3 = -413, -311,$ and -216 cm^{-1} respectively). The red shift reflects a destabilisation of the H–bonded C–H group that can be rationalised as the result of electron density transfer from the halide anion into the σ^* anti–bonding orbital of the C–H group.[23] This effect is expected to diminish for the larger halides due to the increased distance between the anion and C_2H_2. The weakening of the C–H bond is also associated with partial transfer of the intermediate proton from the acetylene molecule towards the halide anion. The extent of the proton transfer and magnitude of the vibrational band shift correlates with the proton affinity (PA) of the halide ion, which decreases down the group (PA = 1395, 1354,

and 1315 kJ.mol^{-1} for Cl$^-$, Br$^-$, and I$^-$ respectively; refs. 24–26) consistent with the experimental ν_3 band shifts.

3.3.5 Comparison with matrix IR spectra

It is worthwhile comparing the gas phase results for the X$^-$–C$_2$H$_2$ dimers with those from Ar matrix *IR* spectra of reaction products between the cesium–halide salts and acetylene.[8]   Comparisons are only possible for the iodide and chloride complexes, as the bromide–acetylene complex was not characterised in the matrix studies and the fluoride–acetylene complex was not studied in the gas phase. The ν_3 band shifts for the matrix spectra are much less than the corresponding gas phase values. For Cl$^-$–C$_2$H$_2$ the shifts are –413 and –239 cm^{-1} for the gas phase and matrix spectra respectively, while for I$^-$–C$_2$H$_2$ the shifts are –217 and –107 cm^{-1}. The large discrepancies are probably due to complexes in the matrix being perturbed by the co–deposited Cs$^+$ counterions or other reaction products. The gas phase values are indubitably more reliable as the complexes do not suffer from environmental perturbations.

3.4 Structural and energetic details for Br$^-$–C$_2$H$_2$ from a rotationally resolved spectrum

The ν_3 band of the Br$^-$–C$_2$H$_2$ complex displays partial rotational resolution which allows quantitative energetic and structural information to be derived. An expanded view of the 2978–2988 cm^{-1} region of the spectrum is presented in Fig. 3.9. The form of the spectrum is unusual, with a gap between P–branch features and seven isolated R–branch lines lying to higher energy. This remarkable form can be explained by noting that for photodissociation to occur, the energy of the absorbed *IR* photon needs to exceed the dissociation energy of the complex. The features are therefore presumed to form part of a rotationally resolved band in which transitions terminating below a threshold upper state J' (hereafter referred to as J'_{min}) are absent as they lie below the Br$^-$ + C$_2$H$_2$ (v = 0) dissociation asymptote. The *IR* predissociation spectrum of the Ar–HN$_2^+$ complex in the 2480–2800 cm^{-1} range displays three separate bands possessing similar forms.[16]
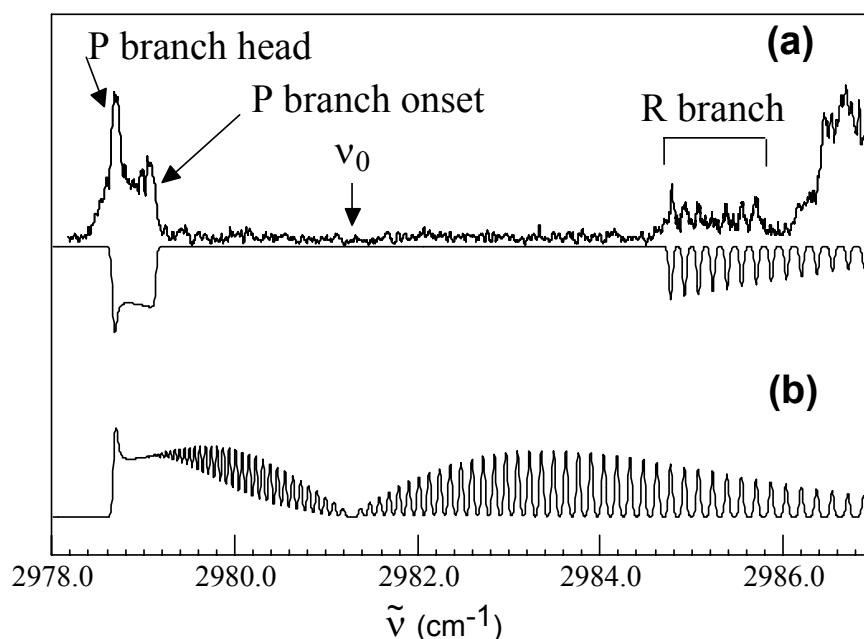
Figure 3.9: *Expanded view of the* Br^-–C_2H_2 *dimer spectrum. (a) is the experimentally observed spectrum with simulated spectrum inverted below (transitions to* $J' < 28$ *absent). (b) A full simulated spectrum.*

To analyse the ν_3 band of Br^-–C_2H_2, the frequencies of the P–branch head, the P–branch onset and the seven R–branch lines were fitted to a standard pseudo–diatomic Σ–Σ energy level expression:

$$\nu_{obs} = \nu_0 + B'[J'(J'+1)] - B''[J''(J''+1)] \tag{2}$$

One problem with the fitting procedure is determination of the correct rotational line numbering. The fitting procedure was run with a number of J'_{min} values as input. Fig. 3.10 shows a plot of standard deviation for the fits *vs* J'_{min}. The optimum value for J'_{min} is 28 indicating that P(29) and R(27) are the first observed transitions in the P and R branches respectively. Fitted rotational constants and assignments for the spectral features are given in Table 3.1.
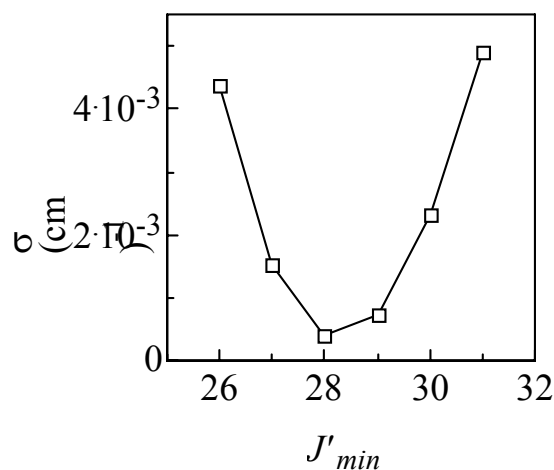
Figure 3.10: *Standard deviations of fits to* Br^-–C_2H_2 *spectral data (Table 3.1) as a function of* J'_{min} *(the minimum upper state* J' *level for which dissociation is possible).*

Table 3.1: *Wavenumbers and assignments for features in the* Br^-–C_2H_2 *spectrum shown in Fig. 3.9. Differences between measured and fitted values and fitted spectroscopic constants are included.*

Wavenumber (cm^{-1})	Measured–Fitted (x 10^{-3} cm^{-1})	Assignment
2978.67	1	P(53)
2979.20	–3	P(29)
2984.78	10	R(27)
2984.92	–2	R(28)
2985.07	–6	R(29)
2985.22	0	R(30)
2985.38	–8	R(31)
2985.55	3	R(32)
2985.70	–8	R(33)

v_o = 2981.28(1) cm^{-1}

B'' = 0.04884(8) cm^{-1}

ΔB = 9.3 x 10^{-4} cm^{-1}

J'_{min} = 28

The spectroscopic constants were used to simulate a spectrum, assuming a rotational temperature of 50 K. The inverted spectrum shown in Fig. 3.9(a) corresponds to transitions terminating at $J' \geq 28$ levels, while the full simulated spectrum is shown in Fig. 3.9(b). While the agreement between simulation and experiment is quite good, there are some discrepancies. The simulation neither reproduces the shape of the P–branch head region nor does it account for the missing R–branch lines after $J' = 33$ in the experimental spectrum. The difference in P–branch head contour may arise from the fact that the simulation assumes a Boltzmann distribution for the population of the rotational energy levels. There is evidence that the ions generated by the cluster ion source are not in thermal equilibrium and that the higher J levels are not as efficiently cooled in the expansion as the lower J levels. This point is discussed in refs. 19 and 27 and also in Chapter 4 with regard to the Br^-–D_2 complex. The rotational lines terminating at the $J' = 33$ and 34 levels may be absent from the experimental spectrum due to perturbing interactions with nearby rovibrational levels. While it is difficult to identify the interacting 'dark' states, one possible candidate might be v_2 in combination with multiple quanta of v_s or v_b. Similar effects have been observed in the *IR* spectra of analogous cation complexes.[15, 16, 28]

The rotational constants derived from the analysis of the spectrum can be used to estimate the vibrationally averaged intermolecular separation between the Br^- ion and the C_2H_2 centre of mass using:

$$R_{cm} = \sqrt{\frac{F}{\mu_{com}} \cdot \left(\frac{1}{B_{com}} - \frac{1}{B_{mon}}\right)} \qquad [3]$$

$F = 16.85763$ is the conversion factor between the moment of inertia ($amu.\text{Å}^2$) and the rotational constant (cm^{-1}), B_{mon} is the rotational constant of acetylene, B_{com} and μ_{com} are rotational constant and reduced mass of the complex. Eqn. [3] yields separations between the halide anion and the midpoint of the acetylene molecule of 4.11 and 4.07 Å for the $v_3 = 0$ and $v_3 = 1$ vibrational states. Assuming an undistorted C_2H_2 monomer unit, the distances between the intermediate proton and the Br^- anion are 2.45 and 2.41 Å respectively. The ground state experimental values compare well with a centre of mass separation of 4.18 Å and intermolecular separation of 2.48 Å predicted by the CCSD(T) calculations of Botschwina *et al.*[4]

The fact that photodissociation of the $Br^-–C_2H_2$ dimer complex occurs from $J' = 28$ but not from $J' = 27$ allows the dissociation energy of the complex to be estimated. Using the fitted parameters, the $J' = 27$ and 28 levels of the $v_3 = 1$ manifold correspond to energies of 3018.9 and 3021.7 cm^{-1}. However, as the complexes dissociate from rotationally excited levels, the fragments separate with translational energy, and as a result the calculated dissociation energy needs to be corrected. This correction was found to be important in the case of the $Ar–HN_2^+$ complex[16] but turns out to be negligible for $Br^-–C_2H_2$.

In the absence of tunnelling, the translational energy of the fragments is related to the initial angular momentum through classical conservation laws. The first available dissociation channel occurs at the top of the J dependent centrifugal barrier of the $Br^- + C_2H_2$ ($v = 0$) rotationally corrected intermolecular potential. The translational energy can be estimated by considering the long range part of the centrifugally corrected intermolecular potential which is given by the sum of the centrifugal, charge–quadrupole and charge–induced dipole potentials:

$$V_{lr}(R,\theta) = \frac{\hbar^2 J(J+1)}{2\mu_{com}R^2} + \frac{Q\Theta}{2(4\pi\varepsilon_o)R^3} \times (3\cos^2\theta - 1) - \frac{1}{2}\frac{Q^2(\alpha_\parallel \cos^2\theta + \alpha_\perp \sin^2\theta)}{(4\pi\varepsilon_o)^2 R^4} \qquad [4]$$

Assuming that the acetylene and intermolecular axes remain aligned during fragmentation ($\theta = 0$), and using literature values of the quadrupole moment and

polarizabilities ($\Theta = 2.209$ x 10^{-39} Cm^2, $\alpha_\| = 5.17$ x 10^{-40} and $\alpha_\perp = 3.14$ x 10^{-40} C^{2}m^{2}J^{-1}; ref. 9), then the top of the barrier in the $J = 28$ rotationally corrected potential occurs at $R_{cm} = 345$ Å, and corresponds to an energy of only 0.002 cm^{-1} above the Br$^-$ + C$_2$H$_2$ ($v = 0$, $J = 0$) asymptote. It is clear that for such low J values the charge–quadrupole potential ($1/R^3$) dominates the centrifugal potential ($1/R^2$) to very long range and the resulting translational energy of the fragments is small. By considering the ranges of the parameters (v_o, B' and J'_{min}) that result in reasonable fits to the *IR* spectrum, the dissociation energy of the Br$^-$–C$_2$H$_2$ complex can be estimated as $D_o = 3020 \pm 3$ cm^{-1}. At this stage, this probably represents the most accurate experimentally determined dissociation energy for a gas phase anion complex. This experimental binding energy compares favourably with the prediction of D_o~2994 cm^{-1} of Botschwina and coworkers from recent CCSD(T) calculations.[4]

3.5 Spectra of larger $F^-–(C_2H_2)_n$, $Cl^-–(C_2H_2)_n$, $Br^-–(C_2H_2)_n$ and I^- $–(C_2H_2)_n$ clusters

The discussion now turns to the larger $X^-–(C_2H_2)_n$ clusters. Infrared spectra of $Cl^-–(C_2H_2)_n$, $Br^-–(C_2H_2)_n$, $F^-–(C_2H_2)_n$, and $I^-–(C_2H_2)_n$ are presented in Figs. 3.11 to 3.14. Due to limitations in the mass range of the second quadrupole mass filter, and difficulties with cluster ion production, the largest clusters that could be studied were $F^-–(C_2H_2)_6$, $Cl^-–(C_2H_2)_9$, $Br^-–(C_2H_2)_8$, and $I^-–(C_2H_2)_4$. The ν_3 absorptions of the $F^-–C_2H_2$ and $F^-–(C_2H_2)_2$ clusters occur below the low frequency end of the OPO scan range (2500 cm^{-1}) and were not observed. The spectra of the smaller complexes (n $\leq$ 5) were recorded by monitoring the n–1 dissociation channel. For the larger complexes, the n–2 or n–3 channels were monitored yielding spectra with improved S/N ratios as the background fragment ion signal from collision induced dissociation to these channels is much less than into the n–1 channel. Spectroscopic data including band positions, band widths (full width at half maximum band height, fwhm) and band shifts from the ν_3 band of bare acetylene (3288.7 cm^{-1}; ref. 10) are given in Table 3.1.
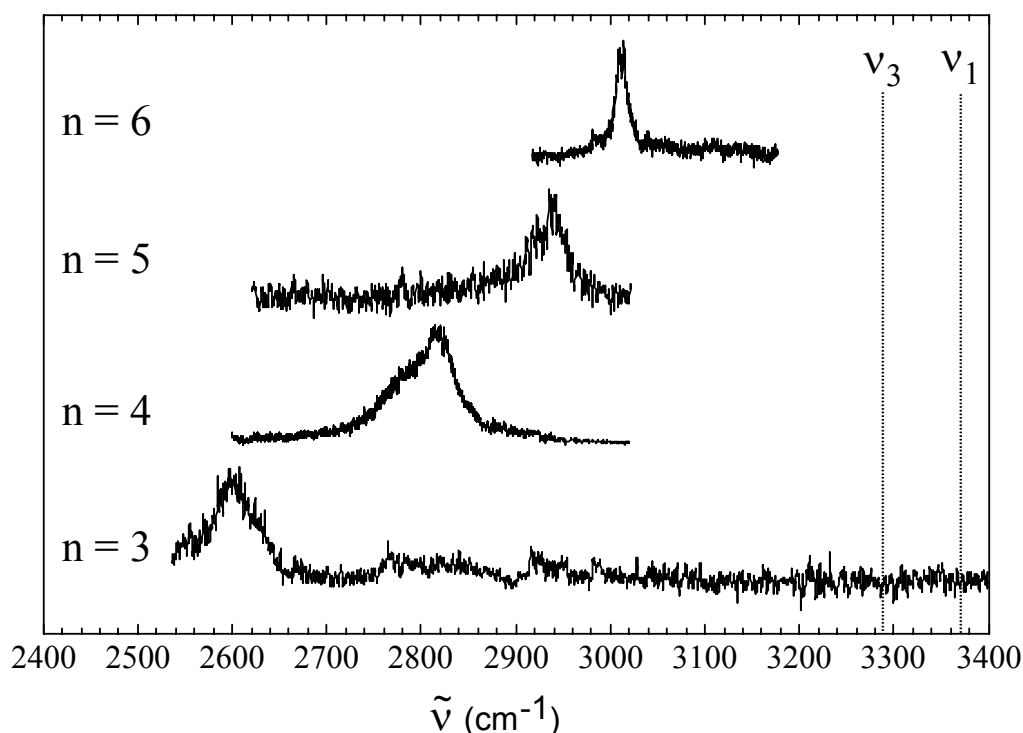
Figure 3.11: *Infrared spectra of $F^-–(C_2H_2)_n$ complexes where n = 3–6. Data are given in Table 3.2. Positions of the ν_3 antisymmetric and ν_1 symmetric stretches of bare acetylene are indicated by dotted lines (3288.7 and 3374 cm^{-1} respectively; refs. 10 and 11).*
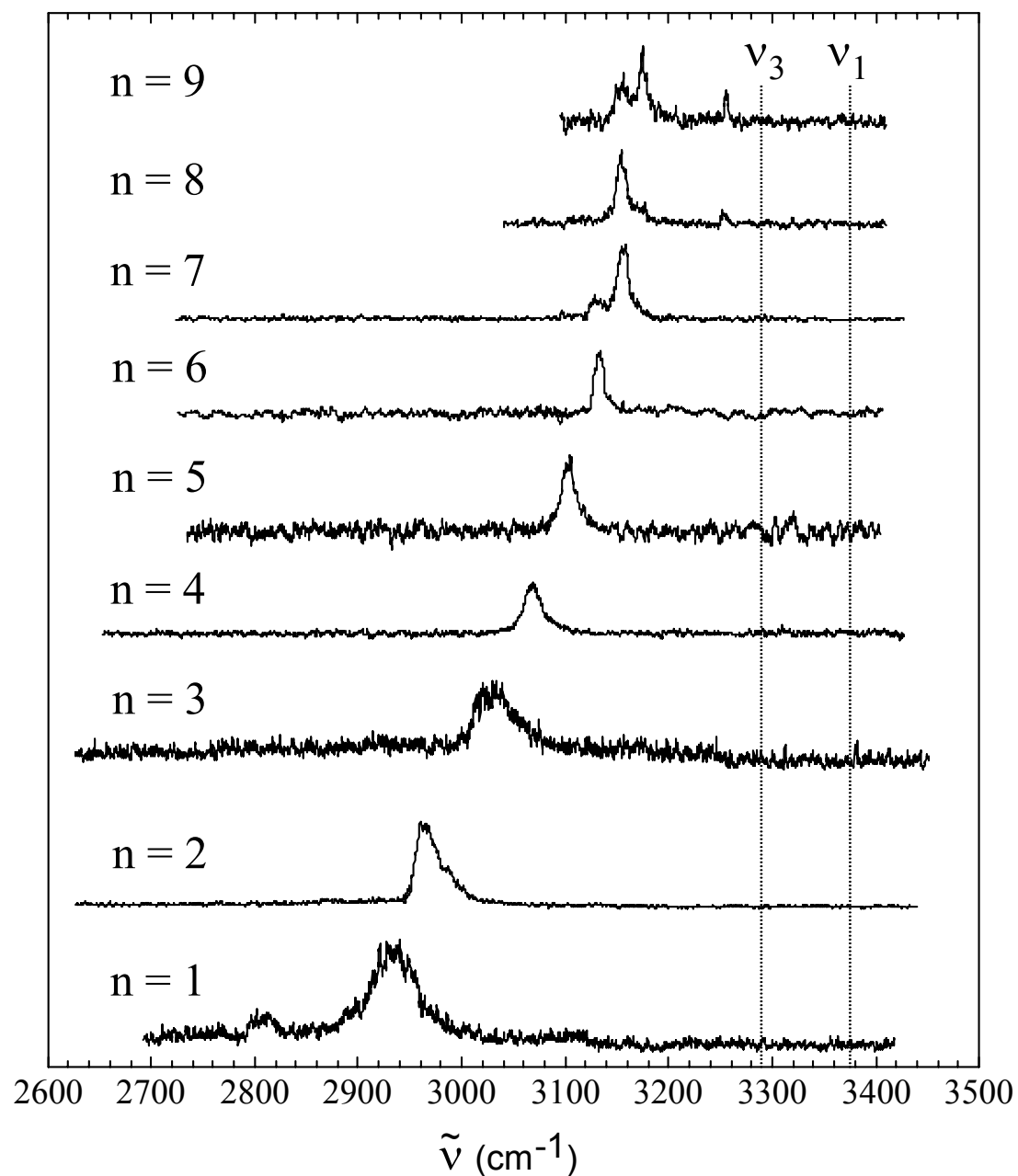
Figure 3.12: *Infrared spectra of $Cl^-–(C_2H_2)_n$ complexes where n = 1–9. Data are given in Table 3.2. Positions of the ν_3 antisymmetric and ν_1 symmetric stretches of bare acetylene are indicated by dotted lines (3288.7 and 3374 cm^{-1} respectively; refs. 10 and 11).*
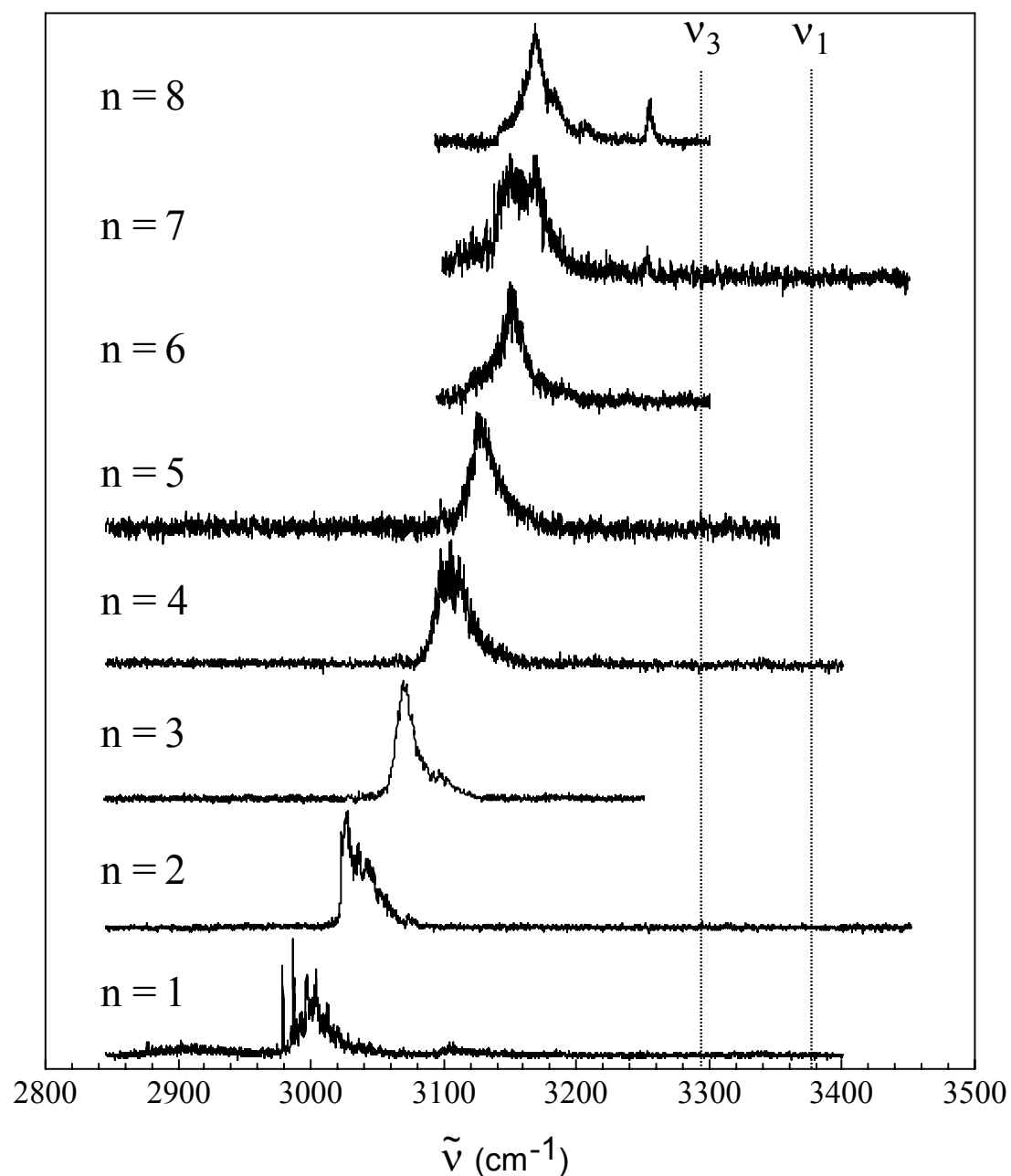
Figure 3.13: *Infrared spectra of Br⁻–(C₂H₂)ₙ complexes where n = 1–8. Data are given in Table 3.2. Positions of the ν_3 antisymmetric and ν_1 symmetric stretches of bare acetylene are indicated by dotted lines (3288.7 and 3374 cm⁻¹ respectively; refs. 10 and 11).*
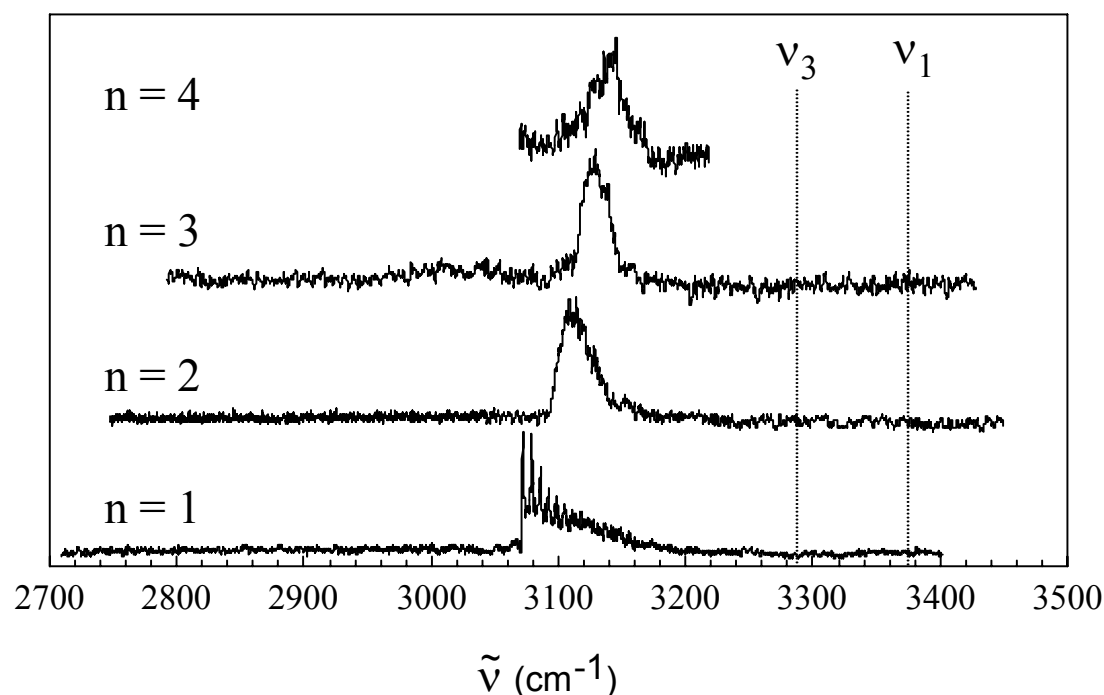
Figure 3.14: *Infrared spectra of I^-–$(C_2H_2)_n$ complexes where n = 1–4. Data are given in Table 3.2. Positions of the ν_3 antisymmetric and ν_1 symmetric stretches of bare acetylene are indicated by dotted lines (3288.7 and 3374 cm^{-1} respectively; refs. 10 and 11).*

3.5.1 Band assignments

The infrared spectra of the X^-–$(C_2H_2)_n$ clusters with $n \leq 6$ feature a single narrow absorption that is shifted to lower frequency from the C–H stretches of bare acetylene. The band, which is assigned to the ν_3 stretches of the ligand acetylene molecules, shifts progressively to higher frequency with increasing cluster size. The ν_1 band observed in the Br^-–C_2H_2 spectrum is not seen in the spectra of the larger clusters. This transition is predicted to be weak for the X^-–C_2H_2 dimers,[4] and should become even more feeble as the clusters become larger, due to the diminution in strength of the halide–acetylene interactions.

Table 3.2: *Vibrational band frequencies, shifts from the ν_3 band of C_2H_2, and band widths (fwhm) for the X^-–$(C_2H_2)_n$ complexes (X^- = F^-, Cl^-, Br^- and I^-). All data are in units of cm^{-1}.*

Cluster	F^-–$(C_2H_2)_n$			Cl^-–$(C_2H_2)_n$			Br^-–$(C_2H_2)_n$			I^-–$(C_2H_2)_n$		
	ν_o	$\Delta\nu$	fwhm	ν_o	$\Delta\nu$	fwhm	ν_o	$\Delta\nu$	fwhm	ν_o	$\Delta\nu$	fwhm
1	–	–	–	2810	−479	20	2981.28	−307	20	3073	−216	80
				2938	−351	50	3340*	−33	10			
X⁻–C₂H₂.Ar	–	–	–	2882	−407	12	2982	−307	10	3075	−214	8
2	–	–	–	2965	−324	28	3040	−249	30	3112	−177	30
3	2600	−689	~100	3029	−260	37	3080	−209	25	3129	−160	25
4	2810	−479	70	3069	−220	20	3110	−179	30	3138	−157	30
5	2940	−349	40	3103	−186	15	3130	−159	20	–	–	–
6	3015	−274	20	3132	−157	10	3150	−139	20	–	–	–
7	–	–	–	3131	−158	13	3150	−139	20	–	–	–
				3155	−134	12	3170	−119	20			
							3255#	−34	8			
8	–	–	–	3155	−134	11	3170	−139	20	–	–	–
				3173	−116		3255#	−34	8			
				3253#	−36	7						
9	–	–	–	3154	−135	11	–	–	–	–	–	–
				3174	−115	12						
				3255#	−34	5						
Matrix†	2873	−416		3050	−239		–	–	–	3182	−107	

* Free C–H stretch for the Br^-–(C_2H_2) dimer. The ν_1 band of C_2H_2 occurs at 3372.5 cm^{-1}; ref. 11

† *IR* matrix values from ref. 8.

\# These bands correspond to absorptions by outer shell acetylene ligands

3.5.2 Cluster structures

The simplicity of the spectra for $n \leq 6$ (each spectrum contains a single, narrow vibrational band) suggests that the clusters adopt interior solvation structures, with the acetylene ligands being roughly equivalent to one another. Interior cluster structures are expected since two acetylene ligands bound to the anion through linear hydrogen bonds should repel each other due to repulsive quadrupole–quadrupole and induced dipole–induced dipole forces. Fig. 3.15 illustrates proposed structures that have linear $X^- - C_2H_2$ bonds, with the C_2H_2 ligands arranged so as to minimise the ligand–ligand repulsive forces. The structures are linear for $X^- - C_2H_2$ and $X^- - (C_2H_2)_2$, trigonal planar for $X^- - (C_2H_2)_3$, tetrahedral for $X^- - (C_2H_2)_4$, trigonal bipyramidal for $X^- - (C_2H_2)_5$, and octahedral for $X^- - (C_2H_2)_6$. These complexes are expected to be extremely floppy with substantial zero point bending excursions.
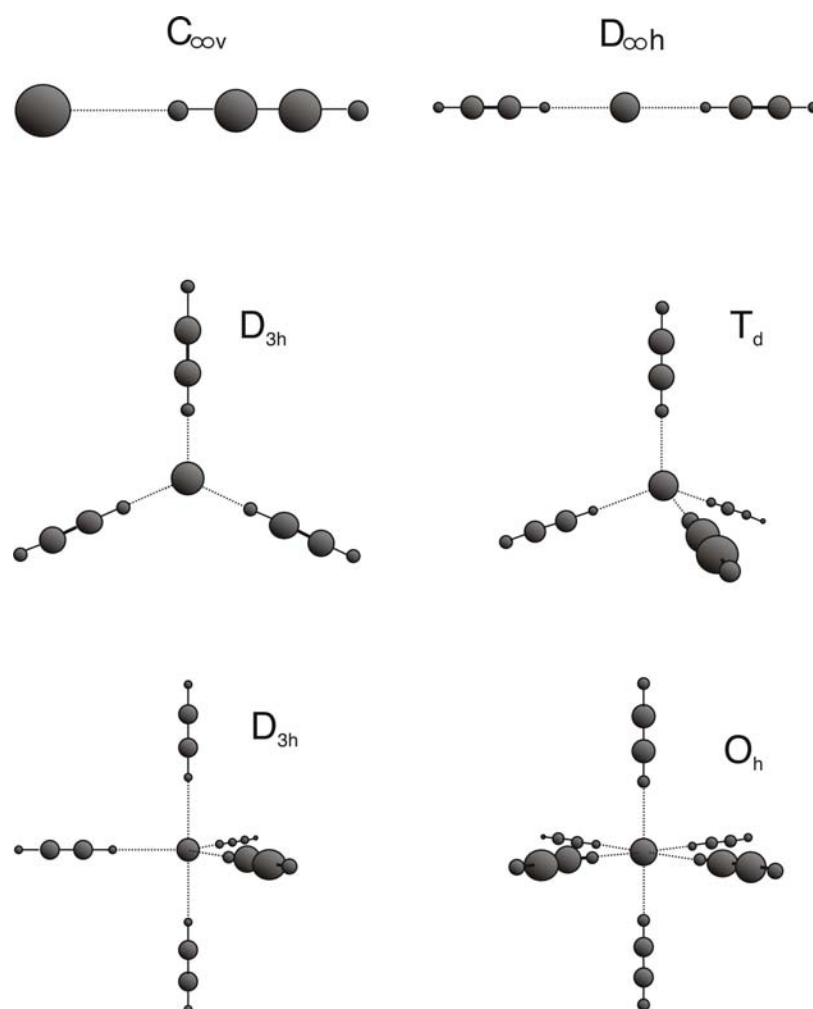
Figure 3.15: *Structures proposed for the $X^- - (C_2H_2)_n$ complexes (n = 1–6). The structures are based on consideration of the dominant anion–ligand cohesive interactions and ligand–ligand repulsive interactions.*

The observed infrared spectra of the X^-–$(C_2H_2)_{1-6}$ clusters are consistent with the structures shown in Fig. 3.15. The n = 1, 2, 3, 4, and 6 clusters should each possess a single *IR* active collective ν_3 stretching mode (doubly degenerate for n = 3 and triply degenerate for n = 4 and 6). For the trigonal bipyramidal X^-–$(C_2H_2)_5$ complex, the non–equivalent axial and equatorial ligands, are associated with two *IR* active collective ν_3 stretching modes (one singly degenerate and the other doubly degenerate). The appearance of a single relatively narrow band in the X^-–$(C_2H_2)_5$ spectra suggests that the axial and equatorial C_2H_2 ligands are similarly perturb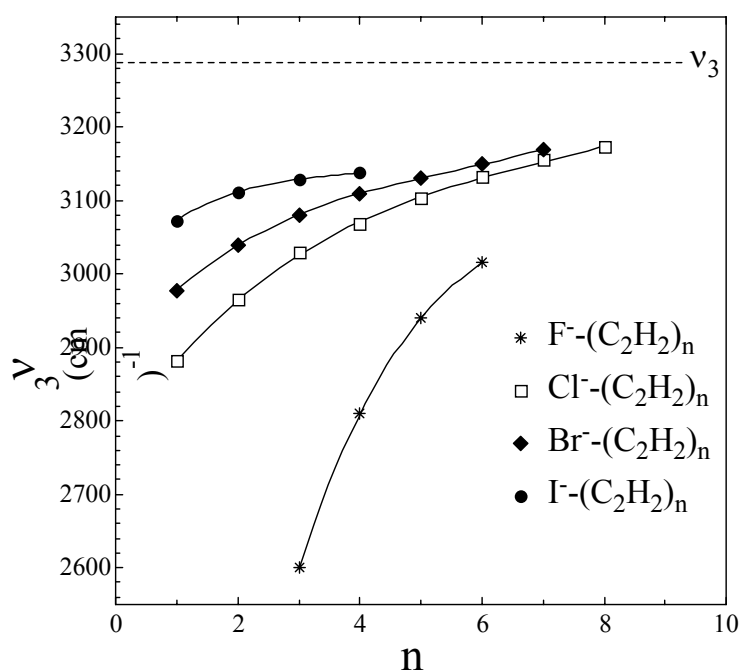ed by the anion. It is also possible that the barrier for interconversion of the axial and equatorial ligands is extremely low, rendering the five ligands effectively equivalent to one another.

3.5.3 Variation of ν_3 with cluster size

The variation of the ν_3 frequency with cluster size is illustrated in Fig. 3.16. The frequencies of the ν_3 modes in the clusters depend on the local bonding environment. The shift of the ν_3 band to higher frequency with the addition of ligands indicates that the intermolecular bonds to the acetylenes progressively weaken, and that the perturbations to the H–bonded C–H groups diminish. This effect can be rationalised by the same argument that was used to explain the origin of the ν_3 vibrational band shift itself. As the clusters become larger there will be a reduction in the electron density transferred to the σ^* antibonding orbital localised on the H–bonded C–H group of any one particular C_2H_2 molecule, and a corresponding decrease in the redshift of the ν_3 band.

Figure 3.16: *Plot of the ν_3 frequency clusters size for F^-–$(C_2H_2)_n$, Cl^-–$(C_2H_2)_n$, Br^-–$(C_2H_2)_n$, and I^-–$(C_2H_2)_n$ with n < 9. The dashed line corresponds to the frequency of the ν_3 antisymmetric C–H stretch of bare acetylene.*

It is evident from Fig. 3.16 that the incremental shifts of the ν_3 bands with ligand number depends on the identity of the halide anion, being largest for the F^-–$(C_2H_2)_n$ clusters and decreasing down the group ($F^- > Cl^- > Br^- > I^-$). As the ligands are in closest proximity to the anion in the F^-–$(C_2H_2)_n$ clusters, it is not surprising that the acetylenic vibrations are most radically altered in these complexes.

Extrapolation of the plot for the F^-–$(C_2H_2)_n$ series allows the unobserved F^-–(C_2H_2) and F^-–$(C_2H_2)_2$ ν_3 band positions to be estimated as ~2000 and 2350 cm^{-1} respectively. The ν_3 frequency of 2873 cm^{-1} for the F^-–(C_2H_2) complex obtained via *IR* matrix spectroscopy[8] certainly overestimates the gas phase value due to perturbations from either co–deposited Cs$^+$ counterions or additional reaction products. Indeed, in the gas phase the ν_3 band of F^-–$(C_2H_2)_3$ occurs at 2600 cm^{-1}, 273 cm^{-1} below the ν_3 band of F^-–(C_2H_2) in an argon matrix.

3.5.4 Trends in ν_3 band contours and widths

There are noticeable trends in the ν_3 vibrational band contours and widths with increasing cluster size (Figs. 3.11 to 3.14 and Table 3.2). The bands lose the prominent P–branch head seen in the Br^-–C_2H_2 and I^-–C_2H_2 dimer spectra and become narrower. For example, in the I^-–$(C_2H_2)_n$ series the band width for the n = 1 cluster is ~80 cm^{-1} and the band has a prominent P–branch head and a high energy tail. In contrast, for the n = 4 cluster the band has a width of ~30 cm^{-1} and a symmetric contour. Similar effects are apparent in the spectra of the other cluster series.

These changes can be explained by considering the diminishing effect of the ν_3 mode on the halide–acetylene interaction potential with increasing cluster size. As mentioned previously, the prominent P–branch heads observed in the spectra of Br^-–C_2H_2 and I^-–C_2H_2 (Fig 3.4) indicate that excitation of ν_3 leads to a contraction and stiffening of the halide–acetylene intermolecular bonds. The upper state intermolecular potential energy curve is therefore deeper and narrower than the ground state curve and hence vibrational hot bands involving the intermolecular stretch extend to higher energy from the ν_3 band (corresponding to the sharp peaks observed in spectra of Br^-–C_2H_2 and I^-–C_2H_2). For the larger clusters, excitation of ν_3 has a smaller effect on the X^-....C_2H_2 interaction potential so that the hot bands more closely overlap one another, resulting in narrower overall band profiles.

Other factors probably also contribute to the narrowing of the ν_3 bands as the clusters become larger. Firstly, the decrease in the cluster rotational constants results in more closely spaced rovibrational transitions. Secondly, as the clusters become larger the binding energy of the acetylene ligands to the anion core declines. This limits the maximum internal energy of the cluster, thereby reducing the spectral congestion arising from vibrational hot bands. The very narrow bands observed for the X^-–C_2H_2.Ar complexes, in which the Ar atom is easily detached (compared to the C_2H_2), are explained by the same argument.

It is interesting to note that the ν_3 bands observed for the F^-–$(C_2H_2)_3$ and F^-–$(C_2H_2)_4$ clusters are particularly broad. The ν_3 band shifts are large ($\Delta\nu_3 > -450$ cm^{-1}) indicative of a strong interaction between the anion and the acetylene ligands. It is possible that dissociation of cold complexes from absorption of a single *IR* photon is not possible and that the bands are broadened as they originate from vibrationally warm complexes. It is not until the F^-–$(C_2H_2)_5$ complex that the band width has decreased below 50 cm^{-1}, comparable to band widths observed for the other halide–acetylene clusters.

3.5.5 Spectroscopic evidence for second solvation shell formation

Steric crowding eventually limits the number of C_2H_2 ligands that can be accommodated in the inner solvation shell. Indeed there is evidence that the ligands begin to occupy the second solvation shell for clusters larger than X^-–$(C_2H_2)_6$ as illustrated in the spectra of Cl^-–$(C_2H_2)_n$ and Br^-–$(C_2H_2)_n$ with n $\geq$ 6 (Figs. 3.17 and 3.18). In addition to the dominant ν_3 band associated with the inner solvation shell C_2H_2 sub–units there is a weak transition to higher frequency at ~3255 cm^{-1} in the spectra of Cl^-–$(C_2H_2)_8$, Cl^-–$(C_2H_2)_9$, Br^-–$(C_2H_2)_7$, and Br^-–$(C_2H_2)_8$. This weaker band is assigned to the ν_3 vibrations of acetylene molecules that interact less strongly with the Br^- and Cl^- ions, and which are likely to be situated in the second solvation shell. The dominant cohesive forces for the acetylene molecule(s) in the second shell should still arise from charge–quadrupole and induction interactions with the halide. This, together with the fact that the acetylene–acetylene interaction potential favours a slipped parallel arrangement for the acetylene dimer,[29] makes it likely that the second shell ligand slips between inner shell acetylenes while being prevented from making intimate contact with the halide anion core due to steric crowding. A possible

structure for the $X^--(C_2H_2)_7$ cluster with six inner shell and one outer shell C_2H_2 ligand (a [6,1] isomer) is shown in Fig. 3.19.a.
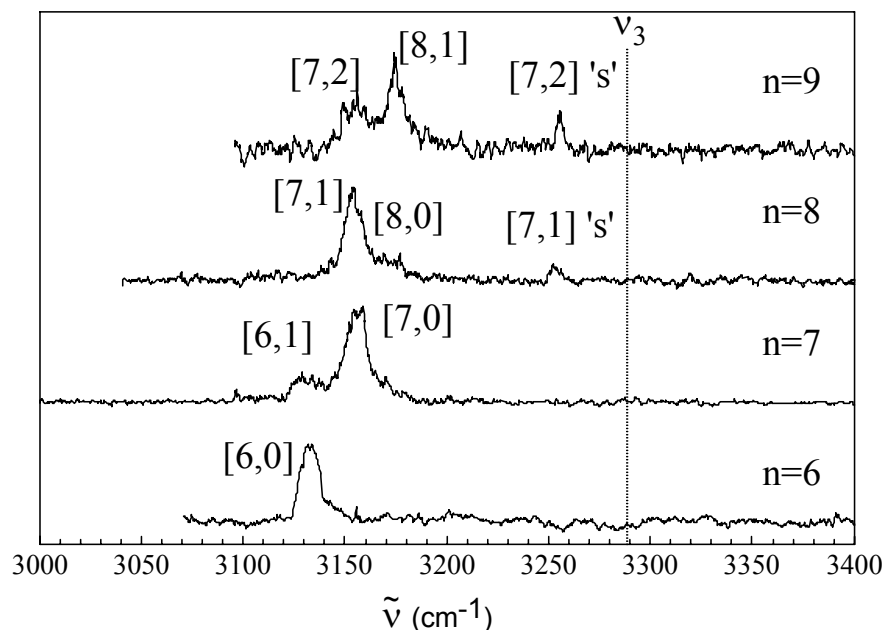
Figure 3.17: *Infrared spectra of $Cl^--(C_2H_2)_n$ clusters (n = 6–9). Bands are labelled using [n,m] notation, where n and m correspond to the number of inner and outer shell acetylene ligands respectively. Bands marked 's' correspond to v_3 absorptions of 2nd shell acetylenes. The dotted line indicates the v_3 frequency of bare C_2H_2 ($3288.7 cm^{-1}$; ref 10)*
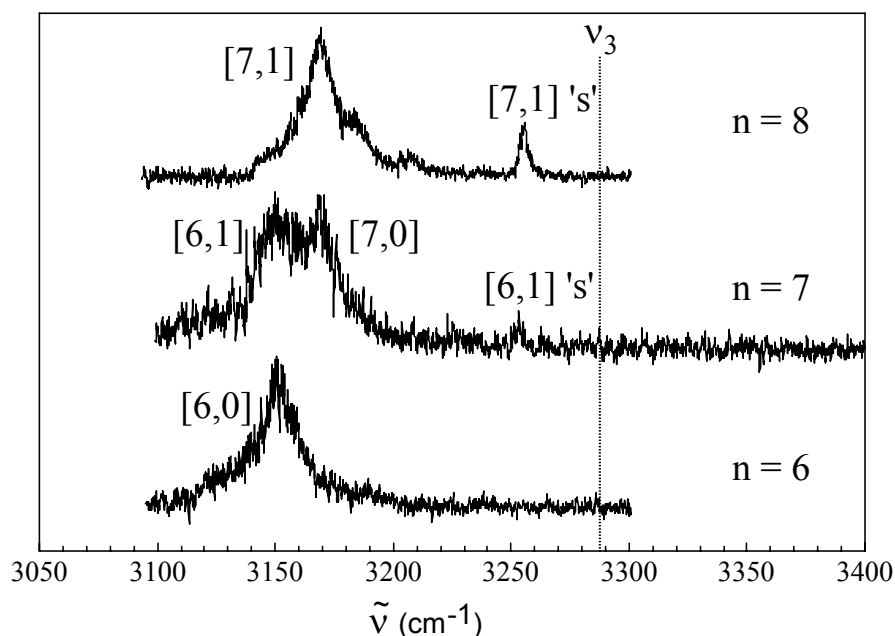
Figure 3.18: *Infrared spectra of $Br^--(C_2H_2)_n$ clusters (n = 6–8). Bands are labelled using [n,m] notation, where n and m correspond to the number of inner and outer shell acetylene ligands respectively. Bands marked 's' correspond to v_3 absorptions of 2nd shell acetylenes. The dotted line indicates the v_3 frequency of bare C_2H_2 ($3288.7 cm^{-1}$; ref 10)*
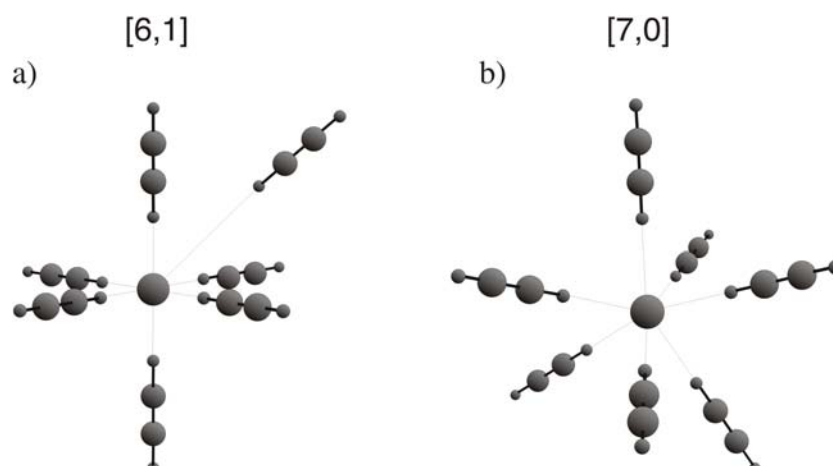
Figure 3.19: *Structures of the [6,1] and [7,0] isomers of X^-–$(C_2H_2)_7$. The acetylene ligand situated furthest from the anion core in the [6,1] isomer should be associated with a ν_3 band, close to the ν_3 antisymmetric C–H stretch of bare C_2H_2.*

As well as the [6,1] isomer shown in Fig. 3.19.a, there is evidence for a [7,0] isomer of the X^-–$(C_2H_2)_7$ cluster in which all seven C_2H_2 ligands are bound to the halide core (Fig. 3.19.b). The main indication for this comes from the fact that for both Cl^-–$(C_2H_2)_7$ and Br^-–$(C_2H_2)_7$, the main ν_3 band is split into two components (Figs. 3.17 and 3.18). The lower energy component occurs at the same frequency as the X^-–$(C_2H_2)_6$ absorption and is assigned to a [6,1] isomer. The frequency of the higher energy component can be anticipated by extrapolating the ν_3 frequencies of the $n = 1$–6 complexes, and is assigned to the [7,0] isomer in which all seven ligands occupy first solvation shell sites. The main ν_3 band in the Br^-–$(C_2H_2)_8$ spectrum consists of a single peak at the same frequency as the ν_3 band of the Br^-–$(C_2H_2)_7$ [7,0] isomer, suggesting the predominance of a single [7,1] isomeric form for $n = 8$. The Cl^-–$(C_2H_2)_8$ spectrum shows evidence of [7,1] and [8,0] isomers, while for Cl^-–$(C_2H_2)_9$ both [7,2] and [8,1] isomers are evident.

There is reason to believe that the second solvation shell is initiated at a slightly earlier stage for Br^-–$(C_2H_2)_n$ than for Cl^-–$(C_2H_2)_n$. For example, in the Br^-–$(C_2H_2)_7$ spectrum the [6,1] and [7,0] peaks have similar intensities while for Cl^-–$(C_2H_2)_7$ the [7,0] peak clearly dominates. In addition, while only a single [7,1] peak is apparent in the Br^-–$(C_2H_2)_8$ spectrum, for Cl^-–$(C_2H_2)_8$ the [7,1] and [8,0] peaks have similar intensities. The number of ligands occupying the first solvation shell in previously characterized halide–ligand complexes generally increases with the size of the halide ion, although the dependence is slight. For example, photoelectron spectra

of Br^-–$(CO_2)_n$ and I^-–$(CO_2)_n$ clusters suggest that the first solvation shell contains 8 and 9 solvent units respectively,[30] while the first solvent shells of Cl^-–$(CH_3CN)_n$, Br^-–$(CH_3CN)_n$ and I^-–$(CH_3CN)_n$ complexes contain in each case 11–12, 12, and 12–13 solvent units.[31]   In these systems the earlier onset of the second solvation shell for clusters containing smaller halides has been explained as due to steric crowding.

3.6 Summary

Infrared spectra of the halide–acetylene complexes, recorded in the vicinity of the C–H stretching bands, provide insights into the structures of the X^-–C_2H_2 dimer complexes and the larger X^-–$(C_2H_2)_n$ clusters. Spectra of the halide–acetylene dimers are consistent with linear H–bonded structures as expected from the highly directional nature of the dominant charge–quadrupole and charge–induced dipole long range forces. Structural details were estimated for the Br^-–C_2H_2 dimer from a rotationally resolved spectrum. Ground and vibrationally excited centre–of–mass separations of 4.11 and 4.07 Å were determined, corresponding to distances between the Br^- and intermediate proton of 2.45 and 2.41 Å respectively. Transitions terminating at levels below $J' = 28$ were absent from the spectrum allowing a binding energy of $D_o = 3020\pm3$ cm^{-1} to be determined for the Br^-–C_2H_2 complex.

The linear hydrogen bonding motif between the halide and acetylene molecule was shown to prevail for clusters with up to nine acetylene ligands bound to the anion. Structures were deduced from the monotonic variation of the ν_3 stretching band with increasing cluster size. For clusters with two or more C_2H_2 ligands bound to the anion the C_2H_2–C_2H_2 attractive forces are overwhelmed by the repulsive quadrupole–quadrupole and induced dipole–induced dipole interactions, which lead to interior solvation structures. Initiation of the second solvation shell was observed for the Br^-–$(C_2H_2)_n$ and Cl^-–$(C_2H_2)_n$ clusters, with the number of C_2H_2 ligands occupying the first solvation shell estimated to be 6 or 7. The second shell C_2H_2 ligands are postulated to slip between the inner ligands, but are prevented from making intimate contact with the halide core by steric crowding.

3.7 References

1. P. v. R. Schleyer and A. J. Kos, Tetrahedron **39**, 1141 (1983)

2. M. Roy and T. B. McMahon, Can. J. Chem. **63**, 708 (1985)

3. J. J. Rabasco and S. R. Kass, J. Am. Soc. Mass Spectrom. **3**, 91 (1992)

4. P. Botschwina and H. Stoll, Phys. Chem. Chem. Phys. **3**, 1965 (2001)

5. P. Botschwina and R. Oswald, J. Chem. Phys. **117**, 4800 (2002)

6. P. Botschwina, T. Dutoi, M. Mladenovic, R. Oswald, S. Schmatz and H. Stoll, Faraday Disc. **118**, 433 (2001)

7. M. Meuwly, P. P. Wolynec and E. J. Bieske, J. Chem. Phys. **116**, 4948 (2002)

8. M–L. H. Jeng and B. S. Ault, J. Phys. Chem. **95**, 2687 (1991)

9. A. D. Buckingham, *Permanent and Induced Molecular Moments and Long–Range Intermolecular Forces*, edited by J. O. Hirschfelder (Wiley and Sons, New York, 1967)

10. W. J. Lafferty and R. T. Thibault, J. Mol. Spectrosc. **14**, 79 (1964)

11. G. Herzberg, *Molecular Spectra and Molecular Structure II: Infrared and Raman Spectra of Polyatomic Molecules* (Krieger, Malabar, 1991)

12. G. C. Pimentel and A. L. McClellan, *The Hydrogen Bond* (W.H. Freeman, New York, 1960)

13. P. S. Weiser, D. A. Wild, P. P. Wolynec and E. J. Bieske, J. Phys. Chem. **104**, 2562 (2000)

14. D. A. Wild, Z. M. Loh, P. P. Wolynec, P. S. Weiser and E. J. Bieske, Chem. Phys. Lett. **332**, 531 (2000)

15. S. A. Nizkorodov, J. P. Maier and E. J. Bieske, J. Chem. Phys. **103**, 1297 (1995)

16. S. A. Nizkorodov, Y. Spinelli, E. J. Bieske, J. P. Maier and O. Dopfer, Chem. Phys. Lett. **265**, 303 (1997)

17. M. Meuwly, S. A. Nizkorodov, J. P. Maier and E. J. Bieske, J. Chem. Phys. **104**, 3876 (1996)

18. S. A. Nizkorodov, O. Dopfer, T. Ruchti, M. Meuwly, J. P. Maier and E. J. Bieske, J. Phys. Chem. **99**, 17118 (1995)

19. S. A. Nizkorodov, J. P. Maier and E. J. Bieske, J. Chem. Phys. **102**, 5570 (1995)

20. P. Ayotte, J. A. Kelly, S. B. Nielsen and M. A. Johnson, Chem. Phys. Lett. **316**, 455 (2000)

21. P. Ayotte, G. H. Weddle, J. Kim and M. A. Johnson, Chem. Phys. **239**, 485 (1998)

22. J. A. Kelly, J. M. Weber, K. M. Lisle, W. H. Robertson, P. Ayotte and M. A. Johnson, Chem. Phys. Lett. **327**, 1 (2000)

23. S. Scheiner, *Hydrogen Bonding. A Theoretical Perspective* (Oxford University Press, Oxford, U.K., 1997)

24. J. D. D. Martin and J. W. Hepburn, J. Chem. Phys. **109**, 8139 (1998)

25. C. Blondel, P. Cacciani, C. Delsart and R. Trainham, Phys. Rev. A. **40**, 3698 (1989)

26. D. Hanstorp and M. Gustafsson, J. Phys. B. **25**, 1773 (1992)

27. T. Ruchti, A. Rohrbacher, T. Speck, J. P. Connelly, E. J. Bieske and J. P. Maier, Chem. Phys. **209**, 169 (1996)

28. S. A. Nizkorodov, M. Meuwly, J. P. Maier, O. Dopfer and E. J. Bieske, J. Chem. Phys. **108**, 8964 (1998)

29. I. L. Alberts, T. W. Rowlands and N. C. Handy, J. Chem. Phys. **88**, 3811 (1988)

30. D. W. Arnold, S. E. Bradforth, E. H. Kim and D. M. Neumark, J. Chem. Phys. **102**, 3510 (1995)

31. G. Markovich, L. Perera, M. L. Berkowitz and O. Cheshnovsky, J. Chem. Phys. **105**, 2675 (1996)

Chapter 4: The Halide–Hydrogen Anion Complexes

4.1 Introduction

This chapter concerns gas phase complexes formed from halide anions and neutral hydrogen molecules, and aims to address the following questions. What are the structures for these complexes? What effect does complex formation have on the H–H stretching frequency? How does this effect vary when the size of halide anion is increased and when the number of ligands around the halide anion is increased?

The earliest investigations of the halide–hydrogen systems focussed on the reactive collisions between H_2 isotopomers and the F^-, Cl^-, and Br^- ions. These studies provided cross sections for the dominant reactive processes.[1, 2] Complexes formed between the alkali–halides and H_2 isotopomers deposited in rare gas matrices have been investigated via *IR* spectroscopy.[3–5] The spectra display ν_{HH} vibrational bands that are shifted to lower frequency with respect to the bare H_2 stretch. The minor dependence of the ν_{HH} band frequency on the identity of the alkali metal was taken as evidence that the hydrogen molecule is predominantly bound to the anion of the alkali halide ion pair. Nevertheless, positive counterions may perturb the hydrogen molecules. Therefore, gas phase vibrational frequencies should be more reliable as the complexes will not suffer from environmental perturbations.

The F^-–H_2 and Cl^-–H_2 anion complexes have been investigated via photoelectron spectroscopy.[6–9] The spectroscopic transitions terminate on the potential energy surfaces for the neutral $F + H_2 \rightarrow HF + H$ and $Cl + H_2 \rightarrow HCl + H$ reactions, thereby providing information on the neutral X–H_2 transition states. *Ab initio* calculations for F^-–H_2 predicted a linear H–bonded minimum energy structure.[10] Rovibrational energy levels have been determined for the F^-–H_2, F^-–D_2 and F^-–T_2 isotopomers using a potential energy surface calculated at the MP2(full)/6–311++G(2df,2pd) level.[11]

Structural and vibrational properties

The dominant cohesive interactions between a halide anion and H_2 molecule are due to the charge–quadrupole and charge–induced dipole forces. The long range potential energy for the interaction is described by:[12]

$$V_{lr}(R,\theta) = \frac{Q\Theta}{2(4\pi\varepsilon_o)R^3} \times (3\cos^2\theta - 1) - \frac{1}{2}\frac{Q^2(\alpha_{||}\cos^2\theta + \alpha_{\perp}\sin^2\theta)}{(4\pi\varepsilon_o)^2 R^4} \tag{1}$$

where Q is the charge on the anion, Θ the quadrupole moment, $\alpha_{||}$ and $\alpha_{\perp}$ are the parallel and perpendicular polarisability components, R is the intermolecular separation and θ is the angle between the H–H and intermolecular bonds. The charge–quadrupole and charge–induced dipole interactions favour linear hydrogen bonded complexes, consistent with the linear geometry predicted for the F^-–H_2 complex.[10, 11]

The question arises, what effect does the presence of the halide anion have on the vibrational properties of the hydrogen molecule? Complex formation with a halide anion reduces the local H_2 symmetry to $C_{\infty v}$. The linear halide–hydrogen complexes posses the vibrational modes shown in Fig. 4.1. These modes correspond to the H–H stretching mode (ν_{HH}), the intermolecular stretching mode (ν_s), and the doubly degenerate intermolecular bending mode (ν_b). Boldyrev *et al*[11] have calculated harmonic intermolecular stretching and bending frequencies of $\nu_s = 384$ cm^{-1} and $\nu_b = 976$ cm^{-1} for the F^-–H_2 complex.
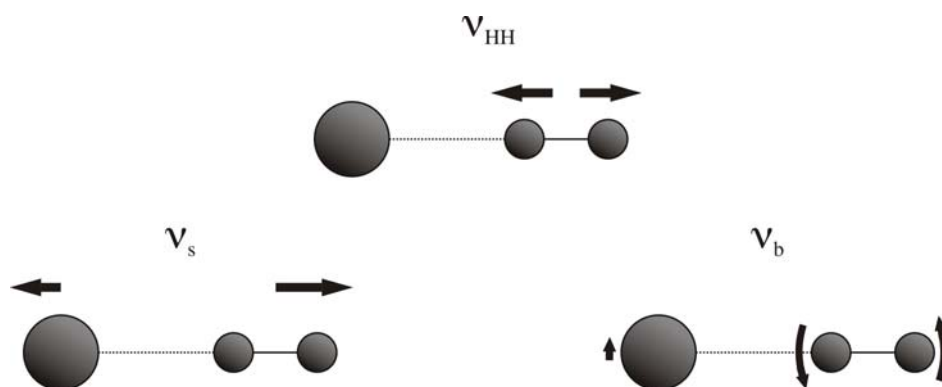
Figure 4.1: *Atomic displacements for the vibrational modes of a linear X^-–H_2 complex (ν_b is doubly degenerate).*

The ν_{HH} mode corresponds to the H–H stretching motion. This mode is predicted to shift to lower frequency and become *IR* active upon complex formation. Both effects are characteristic of hydrogen bonding.[13] The magnitude of the ν_{HH} band shift reflects the strength of the intermolecular interaction, with larger band shifts correlating with stronger intermolecular interactions.

Due to the large rotational constant of H_2, the internal rotation of the diatomic is not entirely quenched and the halide–hydrogen complexes are floppy in the intermolecular bending coordinate. Tunnelling between equivalent linear minima through a T–shaped transition state affects the structural and vibrational properties of the complexes, and is manifested through a splitting of the rovibrational energy levels into doublets. At the limit of an infinite barrier for internal rotation, the tunnelling doublets coincide. In contrast for entirely unhindered internal rotation the tunnelling doublets correspond to the rotational energy levels of the bare H_2 molecule and hence will be separated by $\sim 2b_{HH} = 118$ cm^{-1}. In reality, the tunnelling barrier lies between these two extremes and depends upon the vibrational state of the H_2 molecule, due to the vibrational dependence of the diatomic electrical properties.[14] Rovibrational calculations demonstrate that tunnelling between equivalent hydrogen bonded minima is indeed significant for the F^-–H_2 and F^-–D_2 complexes.[11] The size of the tunnelling barrier is predicted to be ~ 2400 cm^{-1} leading to ground state tunnelling doublets which are separated by 2.9×10^{-3} cm^{-1} for F^-–H_2 and 4.7×10^{-5} cm^{-1} for F^-–D_2. One might anticipate that for the longer, weaker intermolecular bonds characteristic of the Cl^-–H_2, Br^-–H_2, and I^-–H_2 complexes, the tunnelling barrier will be smaller, and hence the doublet splitting will be larger.

A significant part of the material presented in this chapter involves using the spectroscopic data to construct empirical radial intermolecular potential energy curves describing the $X^- + H_2$ and $X^- + D_2$ interactions. The form of the potential curves near the minimum is determined from RKR inversion of the spectroscopic data. At long range the potential curve is determined from the dominant electrostatic and induction potentials averaged over the internal rotation of the H_2/D_2 sub–unit. This treatment assumes a Born–Oppenheimer type separation of the intermolecular stretch vibration and the H–H stretch and intermolecular bend motions. These potential energy curves enable one to estimate properties that are not directly obtainable from the *IR* spectra, such as dissociation energies and frequencies for the intermolecular stretching vibrations.

For larger clusters, in which several H_2 molecules are attached to the anion core, variations in the vibrational properties of the ligands should provide information on the nature of the ion–ligand and ligand–ligand interactions, and help determine the preferred

solvation structures. If the anion is surrounded by roughly equivalent H_2 ligands, the ν_{HH} stretching frequencies of the ligands are expected to move smoothly back towards the stretch frequency of bare H_2. In contrast, if asymmetric solvation structures are formed, the complexity of the spectra is expected to increase due to the different ν_{HH} stretching frequencies of the non–equivalent H_2 ligands.

The remainder of this chapter begins with a brief description of the experimental conditions employed to produce and interrogate the halide–hydrogen gas phase complexes. Mid–infrared spectra of the halide–hydrogen complexes recorded in the vicinity of the H–H and D–D stretching bands are then presented. Next, the rovibrational features are analysed to give quantitative, vibrationally averaged, structural details. The rotational constants are then used to construct empirical one dimensional radial intermolecular potential energy curves. Finally, the mid–infrared spectra of the larger F^- –$(D_2)_n$ and Cl^-–$(D_2)_n$ complexes are presented. The preferred solvation structures are deduced from the evolution of the spectra as increasing numbers of H_2 ligands are coordinated to the halide anion.

4.2 Experimental

The chloride and bromide–hydrogen complexes were produced from a gas mixture consisting of the halide ion precursors CCl_4 and CH_2Br_2 seeded in a mixture of 1:20 H_2/D_2:Ar for the chloride and bromide complexes. The more weakly bound I^-–H_2 complex was difficult to produce. In this case, a gas mixture consisting of CH_3I seeded in pure hydrogen was employed.

The spectra were recorded by monitoring the abundance of charged halide fragments as a function of the *IR* photon energy. The measured line positions were adjusted to account for the Doppler shift arising from the ions ~10 eV energy in the octopole region of the apparatus. The corrections were +0.10 cm^{-1} for $^{35}Cl^-$–H_2, +0.07 cm^{-1} for $^{35}Cl^-$–D_2 and $^{81}Br^-$–H_2 and +0.05 cm^{-1} for $^{79}Br^-$–D_2 and I^-–H_2.

4.3 Infrared spectra of X^-–H_2 & X^-–D_2 complexes, X^- = Cl^-, Br^-, I^-

The infrared spectra of the halide–hydrogen and halide–deuterium complexes recorded in the vicinity of the H–H and D–D stretches are presented in Figs. 4.2 and 4.3. Data from the spectra, including band positions, and band shifts from the $\nu_{HH/DD}$ stretch of bare H_2 and D_2, are given in Table 4.1.

The spectra shown in Figs. 4.2 and 4.3 correspond to the $^{35}Cl^-$–H_2, $^{35}Cl^-$–D_2, $^{81}Br^-$–H_2, $^{79}Br^-$–D_2, and $^{127}I^-$–H_2 isotopomers. A spectrum of the $^{37}Cl^-$–H_2 isotopomer was also recorded, and the data are included in Table 4.1. The differences in the data for the $^{35}Cl^-$–H_2 and $^{37}Cl^-$–H_2 isotopomers are consistent with a pseudo–diatomic model, which predicts that the B rotational constants for $^{35}Cl^-$–H_2 should be 0.3–0.4% larger than for $^{37}Cl^-$–H_2.

The S/N ratios for the spectra deteriorate for the I^-–H_2 and I^-–D_2 complexes due to a decrease in the *IR* intensity of the H–H stretch. Furthermore, the smaller binding energies for these complexes lead to difficulties in producing sufficient ion populations. The I^-–D_2 spectrum is of particularly poor quality and consequently only an approximate band origin could be determined.
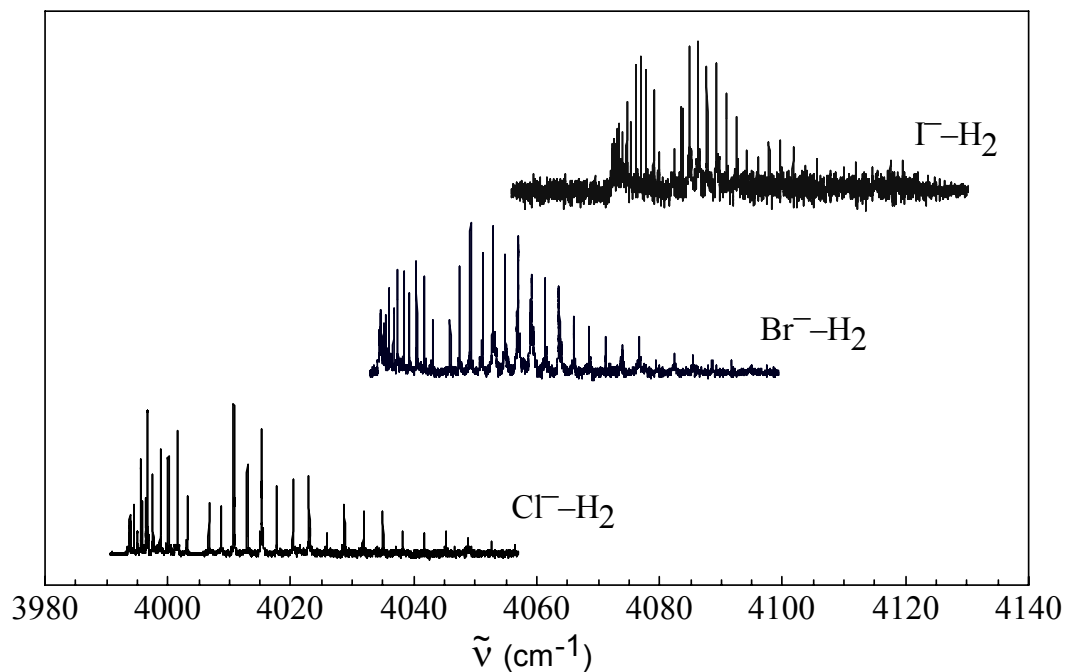
Figure 4.2: *Infrared spectra of the $^{35}Cl^-$–H_2, $^{81}Br^-$–H_2, and I^-–H_2 anion complexes. Spectroscopic data including band positions, band shifts and rotational constants are presented in Table 4.1.*
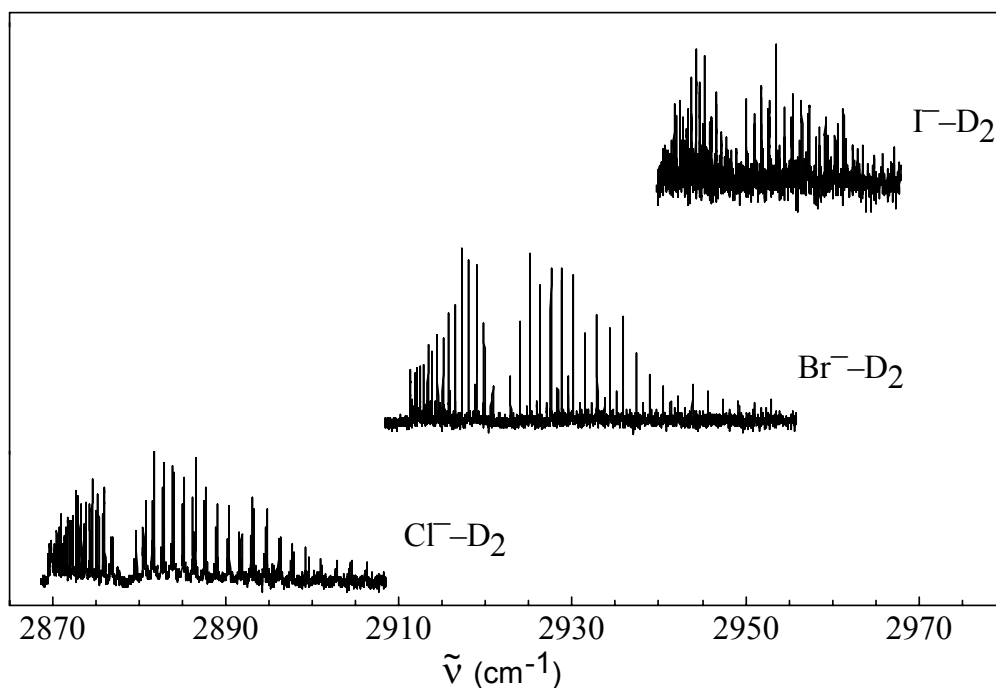
Figure 4.3: *Infrared spectra of the $^{35}Cl^-$–D_2, $^{79}Br^-$–D_2, and I^-–D_2 anion complexes. Spectroscopic data including band positions, band shifts and rotational constants are presented in Table 4.1.*

Table 4.1: Spectroscopic data for the X^-–H_2 and X^-–D_2 complexes where $X^- = Cl^-$, Br^- and I^-. Included are band positions (ν_o), shifts from the bare H_2 and D_2 stretching frequencies ($\Delta\nu_o$), rotational constants (B), centrifugal distortion constants (D), vibrationally averaged intermolecular separations (R_{cm}), harmonic stretch force constants (k_s), and harmonic stretching frequencies (ω_s).

	$^{37}Cl^-$–$H_2(o)$	$^{35}Cl^-$–$H_2(o)$	$^{37}Cl^-$–$D_2(o)$	$^{37}Cl^-$–$D_2(p)$	$^{81}Br^-$–$H_2(o)$	$^{79}Br^-$–$D_2(o)$	$^{79}Br^-$–$D_2(p)$	I^-–$H_2(o)$	I^-–$D_2(o/p)$
ν_o (cm^{-1})	4004.74(8)	4004.84(8)	2878.75(8)	2878.51(8)	4044.46(8)	2907.45(8)	2906.89(8)	4081.11(8)	2934(1)
$\Delta\nu_o$ (cm^{-1})†	−150.5	−150.4	−114.8	−113.0	−110.8	−86.1	−84.6	−74.1	−57
B'' (cm^{-1})	0.853(2)	0.8555(8)	0.4610(5)	0.4612(5)	0.7084(8)	0.3730(8)	0.3734(2)	0.5683(14)	−
D'' (x10^{-5} cm^{-1})	9.3(1.0)	9.7(4)	2.21(17)	2.16(17)	8.4(2)	1.96(44)	1.86(6)	6.7(4)	−
B' (cm^{-1})	0.919(2)	0.9207(8)	0.4841(5)	0.4841(5)	0.7566(8)	0.3897(4)	0.3902(2)	0.6023(12)	−
D' (x10^{-5} cm^{-1})	9.0(1.0)	9.0(3)	2.12(14)	2.06(14)	7.5(2)	1.62(44)	1.72(5)	6.0(4)	−
R''_{cm} (Å)	3.195(5)	3.195(3)	3.159(2)	3.159(2)	3.461(2)	3.414(4)	3.413(1)	3.851(5)	−
R'_{cm} (Å)	3.072(7)	3.077(4)	3.081(3)	3.081(3)	3.347(2)	3.339(4)	3.337(1)	3.739(4)	−
k''_s (N/m)	3.0(2)	2.9(1)	3.7(3)	3.8(3)	1.94(5)	2.4(7)	2.5(1)	1.27(9)	−
k'_s (N/m)	3.8(2)	3.8(1)	4.5(3)	4.6(3)	2.64(5)	3.2(7)	3.1(1)	1.68(13)	−
ω''_s (cm^{-1})	162(10)	159(4)	132(6)	134(6)	129(2)	102(12)	105(2)	104(4)	−
ω'_s (cm^{-1})	184(10)	185(4)	145(6)	147(6)	151(2)	120(12)	117(2)	120(5)	−

† Band shifts for X^-–$D_2(o)$ complexes are relative to the $Q_1(0)$ transition of *ortho*–D_2.
 Band shifts for X^-–$D_2(p)$ and X^-–$H_2(o)$ are given relative to the $Q_1(1)$ transitions of *ortho*–H_2 and *para*–D_2 respectively.[15]

4.3.1 Band assignments

The spectra presented in Figs. 4.2 and 4.3 are similar in appearance, suggesting that the complexes adopt the same geometry. The spectra contain a single vibrational band that is shifted to lower frequency from the position of the H_2 and D_2 stretch bands. Survey scans to lower frequency failed to detect other transitions, permitting an assignment of the observed bands to the $\nu_{HH/DD}$ fundamental stretching vibration. The bands display rotational resolution, and have the form of a Σ–Σ transition with a prominent head in the P–branch. The P–branch head formation is typical of proton bound anion and cation systems,[16–19] and implies that excitation of the mode leads to a contraction of the intermolecular bond. The distinctive Σ–Σ form of the bands suggests that all the complexes adopt a linear equilibrium geometry, which is expected from a consideration of the dominant electrostatic and induction long range forces and has been predicted for the F^-–H_2 complex from *ab initio* calculations.[10, 11] If, in contrast, the complexes adopted a T–shaped equilibrium structure, the infrared spectra would contain Σ–Σ and Π–Π subbands associated with complexes containing H_2 (or D_2) in the $j = 0$ and $j = 1$ states. The Π–Π band would exhibit a characteristic Q–branch as has been observed for the D_2–DCO^+ and H_2–HCO^+ cation complexes.[20, 21]

The wavenumbers of the rovibrational lines were fitted to a standard pseudo–diatomic energy level expression:

$$\nu_{obs} = \nu_0 + B'[J'(J'+1)] - D'[J'(J'+1)]^2$$
$$-B''[J''(J''+1)] + D''[J''(J''+1)]^2 \quad [2]$$

where ν_0 is the band origin, B'' and B' the lower and upper state rotational constants, D'' and D' are the lower and upper state centrifugal distortion constants. Inclusion of cubic distortion terms in the analysis slightly improved the quality of the fits, however the errors in the cubic constants were generally the same order of magnitude as the constants themselves. Constants obtained from the fits are given in Table 4.1, while a full list of transition wavenumbers and residuals ($\nu_{obs} - \nu_{fit}$) can be found in Appendix 1.

The rotational constants are used to estimate vibrationally averaged intermolecular separations, harmonic intermolecular stretching frequencies and force constants for the complexes in the ground and excited vibrational states ($v = 0$ and 1).

The separations between the halide anion X^- and the diatomic centre of mass, effectively averaged over the intermolecular stretching and bending motions of the complex, are estimated from:

$$R_{cm} = \sqrt{\frac{F}{\mu_{com}}\left(\frac{1}{B_{com}} - \frac{\langle 1 + \cos^2\theta \rangle}{2 b_{mon}}\right)}$$ [3]

where $F = 16.85763$ is the conversion factor between the moment of inertia (in amu Å^2) and the rotational constant (in cm^{-1}), b_{mon} is the H_2/D_2 rotational constant ($b''_{HH} = 59.34$ cm^{-1}, $b'_{HH} = 56.37$ cm^{-1}, $b''_{DD} = 29.91$ cm^{-1}, $b'_{DD} = 28.85$ cm^{-1}; ref. 15), B_{com} is the rotational constant for the complex, μ_{com} is the reduced mass of the complex (in amu) and θ is the angle between the diatomic and the intermolecular bonds. The $\langle 1 + \cos^2\theta \rangle$ term, which is included to account for the system sampling non–linear configurations due to zero point energy bending motions, was estimated using the hindered rotor model discussed in Section 4.7. Differences between R_{cm} values calculated using these $\langle 1 + \cos^2\theta \rangle$ estimates and those assuming a linear complex (ie, with $\langle 1 + \cos^2\theta \rangle = 2$) are the same order of magnitude as the errors derived using the upper and lower bounds for the B_{com} rotational constants. The R_{cm} values are given in Table 4.1, with errors calculated by setting the rotational constants to their error limits.

Harmonic intermolecular stretching frequencies for the complexes in the $v = 0$ and 1 states are estimated from the B and D rotational constants using the expression:[22]

$$\omega_s = \sqrt{\frac{4 B_{com}^3}{D_{com}}\left(1 - \frac{B_{com}}{b_{mon}}\right)}$$ [4]

while harmonic stretching force constants were calculated from:

$$k_s = \mu_{com}(2\pi c\,\omega_s)^2$$ [5]

4.3.2 Vibrational band shifts

The ν_{HH} vibrational band shifts for the halide–hydrogen complexes decrease as the halide anion becomes larger. The band shift can be rationalised as resulting from partial transfer of the intermediate proton towards the halide which weakens the H–H bond and decreases the frequency of the stretching motion. The extent of proton transfer correlates with the proton affinity (PA) of the halide ion, which decreases down the group

(PA = 1395, 1354, and 1315 kJ/mol for Cl^-, Br^-, and I^- respectively; refs. 23–25). The halide–hydrogen complexes can be considered as a proton shared between two bases (the halide X^- and H^- ions) with the general form $X^- - -H^+ - -H^-$. The difference in the proton affinities of X^- and H^- ions is large, and hence the complexes can be thought of as a halide tethered to a perturbed H_2 molecule. For the Cl^- ion the difference in proton affinities is smallest (PA = 1395 and 1675 kJ/mol for Cl^- and H^- respectively; refs. 24 and 26). The intermediate proton will be closest to the halide anion, and therefore the Cl^- –H_2 complex will exhibit the largest vibrational shift consistent with the spectra (Table 4.1).

The vibrational band shift can also be attributed to electron transfer from the halide anion to the vacant σ^* antibonding orbital of the H_2 molecule.[27] The magnitude of this effect is again expected to decrease down the group, since, as the halide becomes larger the intermolecular separation increases and electron transfer will be inhibited.

4.3.3 Structural trends

The data clearly shows that the intermolecular bond becomes longer and weaker with increasing halide size. The vibrationally averaged intermolecular separations deduced from the rotational constants are R''_{cm} = 3.195 Å, 3.461 Å, and 3.851 Å for Cl^-–H_2, Br^-–H_2, and I^-–H_2, and R''_{cm} = 3.159 Å and 3.414 Å for Cl^-–D_2 and Br^-–D_2 respectively. The harmonic stretching force constants for the intermolecular bonds also vary in the expected way with k_s'' = 2.9, 1.9, and 1.3 N/m for Cl^-–H_2, Br^-–H_2 and I^-–H_2 respectively and k_s'' = 3.7 and 2.4 N/m for Cl^-–D_2 and Br^-–D_2 respectively.

The halide–hydrogen intermolecular interaction is profoundly affected by excitation of the H–H or D–D stretching mode. The intermolecular bond contracts and stiffens, resulting in the formation of the P–Branch head observed in the spectra. The bond contraction and ratios of stretching force constants derived from the rotational constants are ΔR_{cm} = –0.118, –0.115, and –0.112 Å, ks'/ks'' = 1.3, 1.4, and 1.3 for Cl^-–H_2, Br^-–H_2, and I^-–H_2 respectively. For the Cl^-–D_2 and Br^-–D_2 complexes, the values are ΔR_{cm} = –0.078 and –0.075 Å, and k'_s/k''_s = 1.2 and 1.3 respectively. These effects can be explained in terms of the increased quadrupole moment and polarizabilities of the H_2 and D_2 molecules in the v = 1 state (see Table 4.3).

4.3.4 ortho/para effects in the X$^-$–D$_2$ spectra

Comparison of the X$^-$–H$_2$ and X$^-$–D$_2$ spectra reveals an importance difference; the spectra of the X$^-$–H$_2$ complexes contain a single Σ–Σ band, whereas the spectra of the X$^-$–D$_2$ complexes contain two overlapping Σ–Σ sub–bands. The single Σ–Σ bands observed in the X$^-$–H$_2$ spectra are assigned to complexes with *ortho*–H$_2$ bound to the anion. The two sub–bands observed in the Cl$^-$–D$_2$ and Br$^-$–D$_2$ spectra are assigned to complexes containing either *ortho* or *para*–D$_2$. Fig. 4.4 presents expanded regions of the Cl$^-$–D$_2$ and Br$^-$–D$_2$ spectra clearly showing the sub–bands separated by 0.24 and 0.57 cm^{-1} respectively. Neither the separation between doublets nor the ratio of the intensities changes discernibly throughout the spectra.
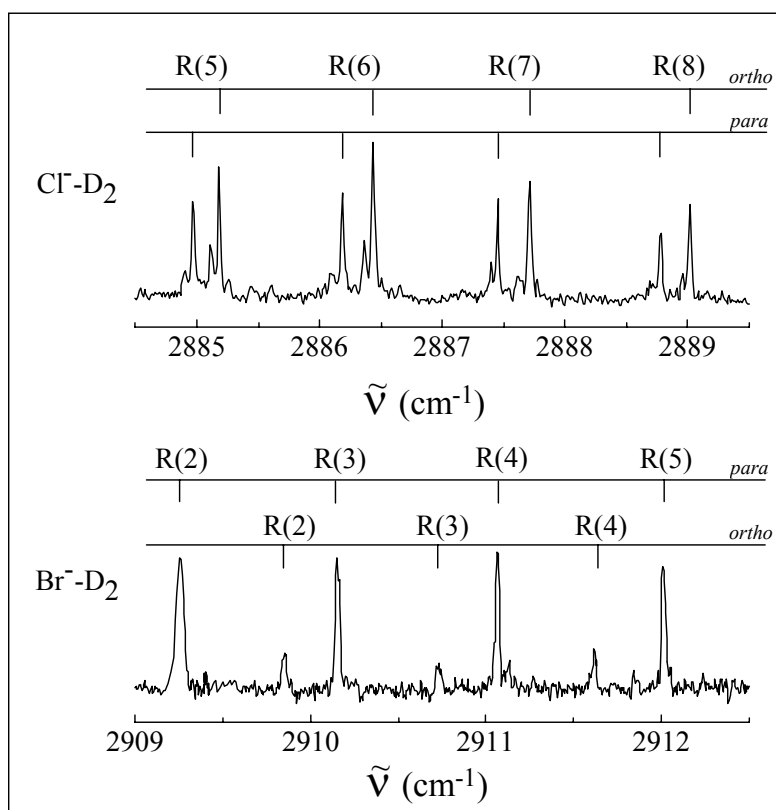
Figure 4.4: *Expanded views of the infrared spectra of the Cl$^-$–D$_2$ and Br$^-$–D$_2$ complexes clearly showing two separate Σ–Σ subbands.*

Two factors lead to the appearance of only one band in the spectra of the X$^-$–H$_2$ complexes. Firstly, due to the nuclear spin statistical weights, the ratio of *ortho:para* molecules in pure H$_2$ is 3:1, where the *ortho* form of H$_2$ corresponds to odd j levels, while the *para* form corresponds to even j levels. Secondly, the complexes formed from *ortho*–

H_2 will be more strongly bound than those formed from *para*–H_2 by approximately twice the H_2 rotational constant. This because the energy of the dissociation asymptote for the *ortho* containing complex:

$$X^- \text{-} H_2(o) \rightarrow X^- + H_2(o) \qquad\qquad [6]$$

where $j = 1$ in the *ortho*–H_2 fragment lies $\sim 2b''_{HH}$ above the energy of the dissociation asymptote of the corresponding $j = 0$ *para*–H_2 channel. Therefore, the ligand exchange reaction:

$$H_2(o) + X^- \text{-} H_2(p) \rightarrow X^- \text{-} H_2(o) + H_2(p) \qquad\qquad [7]$$
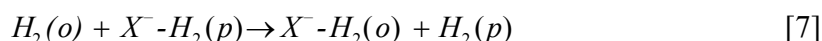
is exothermic by $\sim 2b''_{HH}$ and as a consequence during cluster production in the supersonic expansion *para*–H_2 containing complexes are efficiently converted to *ortho*–H_2 containing complexes.

The nuclear spin statistical weights of D_2 differ from those of H_2. The population ratio of *ortho* to *para* forms is 2:1, where in this case *ortho*–D_2 is associated with even j levels and *para*–D_2 with odd j levels. Furthermore, due to the smaller rotational constant of D_2 compared with H_2, the ligand exchange reaction (Eqn. [7]) is less exothermic, as $2b''_{DD} \approx 60$ cm^{-1} compared with $2b''_{HH} \approx 120$ cm^{-1}. There will be a greater proportion of complexes containing even j, *ortho*–D_2, in the X^-–D_2 ion cluster population compared to the proportion of complexes containing even j, *para*–H_2, in the X^-–H_2 ion population.

The assignment of the sub–bands in Fig. 4.4 to the *ortho* or *para*–D_2 containing complexes can be made by considering Fig. 4.5 which depicts the lowest symmetric (*ortho*) and antisymmetric (*para*) tunnelling levels for the angular potential resulting from the interaction between X^- and D_2 in the $v = 0$ and 1 states (at constant intermolecular separation). The D_2 quadrupole moment increases in the $v = 1$ state ($\Delta\Theta = 1.64 \times 10^{-41}$ Cm^2; ref. 14) resulting in an increased tunnelling barrier height, and a decrease in the tunnelling energy level splitting. Transitions of the *para*–D_2 containing complexes will occur to lower energy, and the observed splitting represents the *difference* in energy level splitting between the upper and lower states.
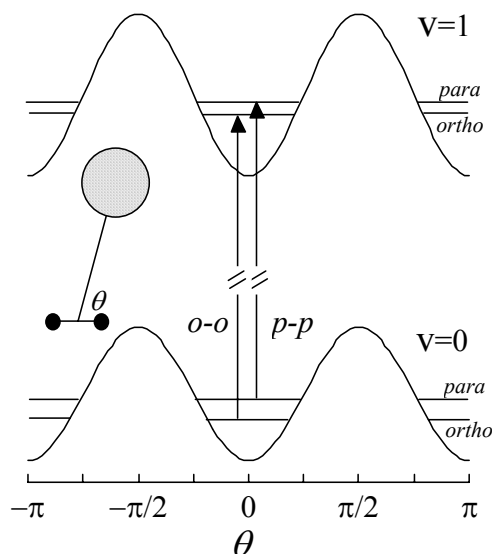
Figure 4.5: *Angular potential energy curves for X⁻ interacting with D_2 in the $v = 0$ (lower) and $v = 1$ (upper) vibrational states. As the splitting between the lowest ortho (symmetric) and para (antisymmetric) levels decreases in the upper state, the p–p transition occurs at slightly lower energy than the corresponding o–o transition.*

4.3.5 Rotational and vibrational temperatures of the complexes.

The P–branch line intensities from the $Br^-–D_2(p)$ spectrum have been used to gauge the rotational temperature of the complexes. A Boltzmann plot is presented in Fig. 4.6. The intensities of lines from a number of individual scans were averaged to account for laser power fluctuations and weighted according to the Hönl–London and degeneracy factors appropriate for the $\Delta J = -1$ transitions of a linear molecule.
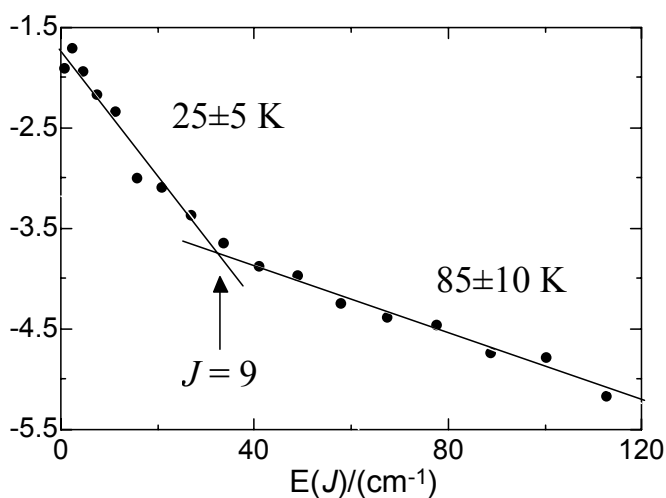
Figure 4.6: *Boltzmann plot for P–branch rovibrational lines of $Br^-–D_2(p)$. The population distribution is non–Boltzmann with high and low J distributions corresponding to temperatures of 25 and 85 K respectively.*

The population of rotational energy levels is not well described by a Boltzmann distribution. Rather, the levels with $J \leq 9$ correspond to a temperature of 25 ± 5 K, while the levels with $J > 9$ correspond to a temperature of 85 ± 10 K. Analogous non–Boltzmann distributions have been observed for cation complexes formed in similar ion sources.[18, 28]   The existence of two populations can be explained by the decrease in efficiency of the collisional energy transfer process for complexes in higher rotational levels. The absence of vibrational hot bands of the form $\nu_{HH}+n\nu_s-n\nu_s$ or $\nu_{HH}+n\nu_b-n\nu_b$ in the spectra suggest that the vibrational temperature of the complexes is also relatively low, compared with the $Br^--C_2H_2$ and $I^--C_2H_2$ complexes (Chapter 3).

4.3.6 Vibrational predissociation rates.

The widths of individual rotational lines can be used to determine the timescale for the dissociation process. Linewidths were determined from scans over individual rovibrational transitions at reduced *IR* laser power to decrease the effect of power broadening. The rotational lines were fitted to Voigt profiles, corresponding to a convolution of Gaussian and Lorentzian components. The Gaussian component accounts for the bandwidth of the *IR* light source (0.017 cm^{-1}), while the Lorentzian component corresponds to the intrinsic lineshape of the lifetime broadened transition. Table 4.2 summarises the Lorentzian widths and corresponding excited state lifetimes for the X^-–H_2 and X^-–D_2 complexes.

Table 4.2: *Widths of Lorentzian components of rotational lines from IR spectra of the X^-–H_2 and X^-–D_2 complexes. Upper state lifetimes of the complexes are also included.*

	X^-–(H_2)		X^-–(D_2)	
	Lifetime broadening (cm^{-1})	τ (ps)	Lifetime broadening (cm^{-1})	τ (ps)
Cl	0.032(5)	165	0.010(5)	530
Br	0.021(6)	250	< 0.01	> 530
I	0.016(7)	330	–	–

The lifetime of the vibrationally excited complexes clearly increases with the size of the halide anion. The predissociation rate depends on the strength of the coupling

between the H–H bond stretch and the dissociation coordinate. If the coupling is strong, energy transfer into the weak intermolecular bond will be rapid, leading to broad spectral lines. The coupling and linewidths decrease for the complexes involving the heavier halides, which have weaker, longer intermolecular bonds. It is interesting to note that the linewidths for the Br^-–D_2 complex are limited by the bandwidth of the *IR* light source $(0.017 \, cm^{-1})$ indicating that the Lorentzian component is less than $0.01 \, cm^{-1}$. This corresponds to an upper state lifetime exceeding 530 ps.

4.4 Radial intermolecular potential energy curves

4.4.1 Introduction

The spectroscopic data presented earlier in this chapter allow one dimensional radial intermolecular potential energy curves to be developed. These potential energy curves further characterise the intermolecular interactions in the halide–hydrogen complexes, providing information that is not available directly from the spectra, including estimates of the binding energies and anharmonic intermolecular stretching frequencies. The form of the potentials near the bottom of the well is determined by inversion of the spectroscopic data using the Rydberg–Klein–Rees (RKR) procedure,[29, 30] while the long range potential is determined by consideration of the long range interaction between a point negative charge and H_2 molecule.

When modelling the long range portion of the potential energy curves, the assumption that the complex remains linear as the halide and H_2 fragments separate is not valid due to the large rotational constants of the H_2 and D_2 diatomics. As a result the long range radial potential needs to be adjusted to account for the complexes sampling less attractive configurations, due to internal rotation of the diatomic fragment. This issue is addressed by solving the hindered rotor Hamiltonian describing the atom–diatomic interaction at fixed intermolecular separation. The lowest energy eigenvalue of the Hamiltonian defines an effective angle–averaged radial intermolecular potential. This procedure is similar to the Born–Oppenheimer (BO) separation of electronic and nuclear motions. The BO treatment assumes that the slower radial motion is governed by an effective potential derived by averaging the long–range electrostatic and induction potential energies over the more rapid bending motion.

4.4.2 Potential energy curve construction

At long range, the dominant potential energy terms arise from the charge–quadrupole and charge–induced dipole interactions: [12]

$$V_{LR}(R,\theta) = \frac{Q\Theta(3\cos^2\theta - 1)}{8\pi\varepsilon_o R^3} - \frac{1}{2}\frac{Q^2(\alpha_{\parallel}\cos^2\theta + \alpha_{\perp}\sin^2\theta)}{4\pi\varepsilon_o R^4} \qquad [8]$$

where R is the separation between the X^- and the H_2 centre of mass, θ the angle between the H–H bond and the vector joining the bond midpoint and the X^- anion, Θ is the H_2 quadrupole moment, and $\alpha_{\parallel}$ and $\alpha_{\perp}$ are the parallel and perpendicular polarizabilities of H_2. Calculated values for Θ, $\alpha_{\parallel}$ and $\alpha_{\perp}$ for H_2 in the v = 0 and v = 1 vibrational states are taken from ref. 14. The electrostatic and induction interactions favour linear ($\theta = 0$ or 180^0) over T–shaped structures ($\theta = 90$ or 270^0).

To determine the angle–averaged radial potential energy, the space fixed hindered rotor Hamiltonian:

$$\hat{H} = b\hat{\mathbf{j}}^2 + B\hat{\mathbf{l}}^2 + V(\theta) \qquad [9]$$

is solved to determine the lowest eigenvalue at a series of separations (2.7, 2.8, 2.9, 3.0, 3.1, 3.2, 3.3, 3.5, 3.8, 4.3, 5, 6, 8, 12 and 20 Å). In Eqn. [9], $\hat{\mathbf{j}}$ and $\hat{\mathbf{l}}$ are angular momentum operators pertaining to rotation of the diatomic (rotational constant b) and the entire complex (rotational constant B) respectively. The angular potential $V(\theta)$ is determined at each separation from Eqn. [8].

Solution of the hindered rotor Hamiltonian is assisted by casting the long range potential in the form:

$$V_{lr}(R) = V_0(R) + V_2(R)P_2(\cos(\theta)) \qquad [10]$$

where $P_2(\cos(\theta))$ is the second order Legendre polynomial. The basis set is constructed as the sum of spherical harmonic products:

$$\psi_{jl}^{JM} = \sum_{m_j m_l}\left\langle jlm_jm_l\middle|JM\right\rangle Y_{jm_j}Y_{lm_l} \qquad [11]$$

where $\left\langle jlm_jm_l\middle|JM\right\rangle$ are the Clebsch–Gordan coefficients, Y_{jm_j} and Y_{lm_l} are the spherical harmonic functions describing the rotation of the H_2 diatomic and the X^-–H_2 complex respectively.

A basis set with functions up to $j = 15$ is sufficient to converge the lowest eigenvalues to less than 10^{-5} cm^{-1}. For a homonuclear diatomic the Hamiltonian matrix separates into two blocks involving even and odd j terms. These terms correspond to complexes containing *para* and *ortho*–H$_2$ or *ortho* and *para*–D$_2$ respectively. The lowest eigenvalues are fitted by a sum of third, fourth and fifth order inverse power terms:

$$V_{LR}^{BO}(R) = a_o - \frac{a_3}{R^3} - \frac{a_4}{R^4} - \frac{a_5}{R^5} \qquad\qquad [12]$$

to define the Born–Oppenheimer (BO) long–range radial potential. The dissociation limit (a_o) is set to zero for *ortho*–D$_2$ while it is $2b_{HH}$ for *ortho*–H$_2$ and $2b_{DD}$ for *para*–D$_2$.

It is worth noting that the intermolecular potential energy determined from the hindered rotor Hamiltonian agrees with the energy levels of H$_2$ Stark shifted by the electric field emanating from a point negative charge, computed by Poll and Hunt.[31] The two sets of data are compared in Fig. 4.7.
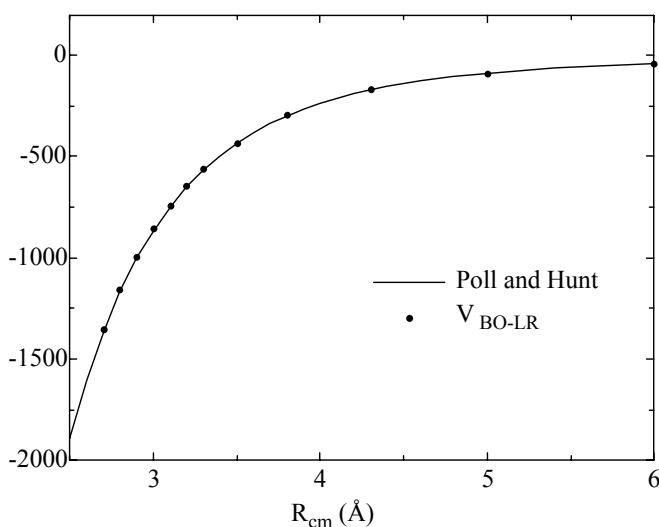
Figure 4.7: *Comparison of the $V_{BO–LR}$ potential for H$_2$ interacting with a point negative charge obtained from the hindered rotor model and the Stark shifted energy levels of H$_2$ predicted by Poll and Hunt.[31]*

The form of the potential near the bottom of the curve is determined using the RKR procedure described in refs. 29 and 30 and is represented by a Morse potential:

$$V_m(R) = a_o + D_e(e^{-2\beta(x-1)} - 2e^{-\beta(x-1)}) \qquad\qquad [13]$$

where $x = R/R_e$. The Morse parameters (D_e, β, and R_e) are determined using the iterative rotational RKR procedure, with the spectroscopically determined rotational constants and centrifugal distortion constants (B and D) used as input. The RKR

procedure generates inner and outer turning points on the set of rotationally modified potential energy curves:

$$V_M(R,J) = V_M(R) + \frac{\beta^2 I(J+1)}{R_0^2 + R^2} \qquad [14]$$

where R is the distance between the diatomic centre of mass and the X^- anion, $\beta = \sqrt{h/8\pi^2 \mu c}$, and R_o is related to the diatomic moment of inertia (I) and the reduced mass of the X^-–H_2 pseudo–diatomic (μ) by $R_o = \sqrt{\langle I\cos^2\theta\rangle/\mu}$. Note that the centrifugal term has been altered to account for the extended nature of the diatomic. Estimates for $\langle\cos^2\theta\rangle$ obtained from the hindered rotor wavefunctions at the vibrationally averaged intermolecular separations are given in Table 4.3. The turning points on the rotationally corrected potentials are readily related to those on the rotationless potential. Expressions for the turning points in terms of the derivatives of the reference potential and the spectroscopically determined rotational constants are given in refs. 29 and 30. An harmonic approximation is used initially to estimate inner and outer turning points to which Eqn. [13] is least square fitted by adjusting D_e, β, and R_e. Using this fitted potential, more accurate expressions for the vibrational dependence of $E(v,J)$ and $B(v,J)$ are obtained. With these, an improved set of turning points are determined which are again fitted by adjusting D_e, β, and R_e in Eqn. [13]. This iterative procedure is continued until convergence is achieved. At each iteration, the RKR points were offset so that the fitted Morse function matched the long range $V_{LR}^{BO}(R)$ potential at a certain $R_j(Å)$ value.

The complete radial intermolecular potential is constructed by joining the Morse potential to the angle averaged long–range potential:

$$V_{Total}(R) = f(R)V_M(R) + g(R)V_{LR}^{BO}(R) \qquad [15]$$

where $f(R)$ and $g(R)$ are the switching functions:

$$f(R) = 0.5(\tanh(w(R_j - R)) + 1),$$
$$g(R) = 0.5(\tanh(w(R - R_j)) + 1). \qquad [16]$$

Here w is a parameter that determines the width of the switching functions (set to 10 Å^{-1}) and R_j is the abscissa of the joining point which is generally chosen to be approximately 0.2 Å beyond the outer–most RKR turning point. It was found however that the properties of the potential curves are relatively insensitive to variations of $\pm$ 0.2 Å for R_j.

Fourteen BO–RKR potential curves were generated corresponding to the Cl⁻, Br⁻, and I⁻ anions interacting with $H_2(o)$ and $D_2(o/p)$ in the v = 0 and v = 1 states. Parameters for the potential energy curves are provided in Table 4.3. The rotational RKR procedure was verified by solving the radial Schrödinger equation for each of the potential energy curves using LEVEL 7.0 (ref. 32). For all the potential curves, the ground state energies agreed with the energy of the $J = 0$ RKR turning points to within 1 cm⁻¹. Table 4.4 lists the D_o, D_e, and R_e values for the fourteen BO–RKR potential energy curves together with the energies of the first five intermolecular stretching levels. Errors in D_o, D_e, and R_e are estimated by running the rotational RKR program with the input rotational constants (B and D) set at their error limits.

Two points regarding the radial potential energy curves are worth emphasising. Firstly, it should be remembered that the D_e and D_o values for the radial potential energy curves of the complexes containing *ortho*–H_2 or *para*–D_2 are taken with respect to the H_2/D_2 $j = 1$ asymptote. Dissociation energies with respect to the H_2/D_2 $j = 0$ asymptote should be approximately $2b_{HH} \approx 120$ cm⁻¹ and $2b_{DD} \approx 60$ cm⁻¹ less. Secondly, it should be noted that the D_e values for the one dimensional radial curves include a contribution from the intermolecular bending zero–point energy. The values will therefore be smaller than the well depths of corresponding two dimensional surfaces.

4.4.3 Improvements to the potentials

There are several avenues for improving the intermolecular potentials. The effects of dispersion and higher order electrostatic and induction interactions on the long range $X^- + H_2$ interaction potential could be included in Eqn. [8]. These effects will be substantially smaller than the charge–quadrupole and charge–induced dipole interactions, but can be expected to increase the binding energy slightly.

There may also be concerns arising from the fact that the long–range potential curve is joined to the RKR generated Morse potential at a separation where there may be significant repulsive contributions to the potential energy. In this regard, the potential curves would be improved by employing spectroscopic data pertaining to higher intermolecular stretch states (nv_s). These data would define RKR points further out on the radial potential where the influence of the repulsive part to the intermolecular potential is less significant.

Table 4.3: *Parameters for BO–RKR radial potential curves (Eqn. [15]) for X⁻–H₂ and X⁻–D₂ with the diatomic in the v = 0 and v = 1 states. Quadrupole moments and polarizabilities are taken from ref. 14 and b_{mon} taken from ref. 15. The joining point (R_j) was 3.8 Å for Cl⁻–H₂ and Cl⁻–D₂, 4.25 Å for Br⁻–H₂, 4.0 Å for Br⁻–D₂ and 4.60 Å for I⁻–H₂. A value of w = 10 Å⁻¹ was used for all potential curves.*

	^{35}Cl⁻–H₂		^{81}Br⁻–H₂		I⁻–H₂		^{35}Cl⁻–D₂(o)		^{35}Cl⁻–D₂(p)		^{79}Br⁻–D₂(o)		^{79}Br⁻–D₂(p)	
	v = 0	v = 1	v = 0	v = 1	v = 0	v = 1	v = 0	v = 1	v = 0	v = 1	v = 0	v = 1	v = 0	v = 1
b_{mon} (cm⁻¹)	59.34	56.37	59.34	56.37	59.34	56.37	29.91	28.85	29.91	28.85	29.91	28.85	29.91	28.85
Θ (x10⁻⁴⁰ C m²)	2.169	2.401	2.169	2.401	2.169	2.401	2.135	2.299	2.135	2.299	2.135	2.299	2.135	2.299
$\alpha_{\|\|}$ (x10⁻⁴⁰ C²m² J⁻¹)	1.115	1.243	1.115	1.243	1.115	1.243	1.096	1.185	1.096	1.185	1.096	1.185	1.096	1.185
$\alpha_\perp$ (x10⁻⁴⁰ C²m² J⁻¹)	0.781	0.834	0.781	0.834	0.781	0.834	0.774	0.810	0.774	0.810	0.774	0.810	0.774	0.810
$<\cos^2\theta>$	0.75	0.78	0.72	0.76	0.70	0.71	0.82	0.84	0.82	0.84	0.80	0.81	0.80	0.82
D_e (cm⁻¹)	574	722	437	550	312	385	570	679	630	742	419	514	474	556
β	3.96	3.89	4.116	4.061	4.480	4.399	4.38	4.26	4.18	4.11	4.43	4.57	4.23	4.22
R_e (Å)	3.130	3.020	3.385	3.279	3.757	3.656	3.111	3.037	3.114	3.040	3.359	3.289	3.361	3.290
a_0 (cm⁻¹)	118.7	112.7	118.7	112.7	118.7	112.7	0	0	59.8	57.7	0	0	59.8	57.7
a_3 (x 10³ cm⁻¹ Å³)	5.596	5.789	5.712	5.797	5.714	5.799	0	0	3.296	2.955	0	0	3.293	3.016
a_4 (x 10⁴ cm⁻¹ Å³)	5.079	5.870	4.995	5.866	4.994	5.865	5.931	6.743	6.858	7.862	5.932	6.739	6.682	7.820
a_5 (x 10⁴ cm⁻¹ Å³)	3.283	3.587	3.431	3.594	3.432	3.596	5.180	4.931	1.008	0.450	5.180	4.947	1.003	0.525

Table 4.4: *Properties of the X^-–H_2 and X^-–D_2 clusters, with the diatomic in the $v = 0$ and $v = 1$ states, derived from the BO–RKR potential energy curves (Eqn. [15]) with the parameters listed in Table 4.3. Errors in R_e, D_e, and D_o are estimated by generating BO–RKR curves with the input rotational constants set at their error limits. The vibrational band shift Δv is the difference in D_o values for the $v = 0$ and $v = 1$ potential curves. R_e is expressed in Å, while all other values are expressed in cm^{-1}.*

	$^{35}Cl^-$–H_2		$^{81}Br^-$–H_2		I^-–H_2		$^{35}Cl^-$–$D_2(o)$		$^{35}Cl^-$–$D_2(p)$		$^{79}Br^-$–$D_2(o)$		$^{79}Br^-$–$D_2(p)$	
	$v = 0$	$v = 1$	$v = 0$	$v = 1$	$v = 0$	$v = 1$	$v = 0$	$v = 1$	$v = 0$	$v = 1$	$v = 0$	$v = 1$	$v = 0$	$v = 1$
R_e	3.130(2)	3.020(2)	3.384(2)	3.279(2)	3.757(4)	3.656(3)	3.111(2)	3.037(2)	3.114(2)	3.040(2)	3.359(4)	3.289(4)	3.361(1)	3.290(1)
D_e	574(10)	722(10)	436(5)	550(7)	312(8)	385(10)	570(15)	679(15)	630(15)	742(15)	419(20)	514(20)	474(4)	556(4)
D_o	488(10)	623(10)	365(5)	468(7)	253(8)	319(10)	499(15)	602(15)	559(15)	665(15)	364(20)	450(20)	418(4)	495(4)
Δv	…	135	…	103	…	66	…	103	…	106	…	86	…	77
E(1,0)	151	176	123	144	97	111	127	140	129	142	98	115	101	112
E(2,0)	271	320	216	259	163	193	234	260	239	266	180	211	187	209
E(3,0)	355	427	277	338	194	245	318	360	329	370	241	286	254	287
E(4,0)	411	403	317	392	229	278	380	435	397	451	286	341	306	348
E(5,0)	447	553	341	427	242	298	425	491	449	515	317	381	343	393

4.4.4 BO–RKR potential energy curves

As an example, the BO–RKR potential energy curve for $Br^- + H_2(o)$ (v = 0) is presented in Fig. 4.8. As shown in the inset, the differences between the RKR points and the fitted function (Eqn. [15]) divided by the well depth D_e are less than 3×10^{-3}.
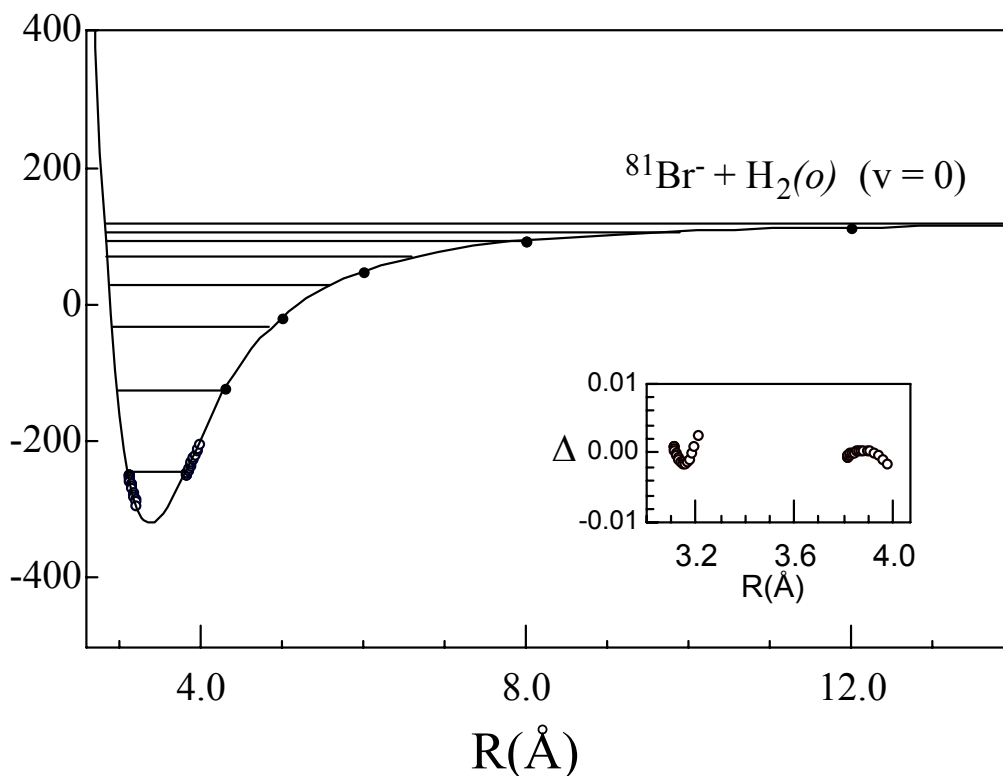
Figure 4.8: *Effective radial potential energy curve for the $^{81}Br^- + H_2(o)$ (v = 0) interaction The RKR points are indicated by open circles, while the long range points obtained by diagonalizing the hindered rotor Hamiltonian (Eqn. [9]) are shown as solid circles. The short range Morse curve is joined to the long range BO curve at $R_j = 4.25$ Å. Parameters for the curve are provided in Table 4.3.*

The potential energy curve supports eight intermolecular stretching levels. The spacing between the two lowest levels suggests an intermolecular stretching frequency of $v_s = 123$ cm^{-1}, slightly less than the harmonic stretching frequency ($\omega_s = 129$ cm^{-1}) derived from the B and D values through Eqn. [4]. The equilibrium centre of mass separation is predicted to be 3.384 Å, approximately 0.08 Å shorter than the vibrationally averaged intermolecular separation deduced from the rotational constants and Eqn. [3]. The predicted binding energy is $D_o = 365$ cm^{-1}.

As mentioned previously, the effect of exciting the H–H or D–D stretch vibration is to shorten and stiffen the intermolecular bond. This is manifested in the spectra through P–branch head formation. The change in intermolecular interaction between the bromide anion and H_2 in the $v = 0$ and $v = 1$ vibrational states is apparent in Fig. 4.9, where it is obvious that the excited state curve is narrower and deeper compared with the lower state curve.
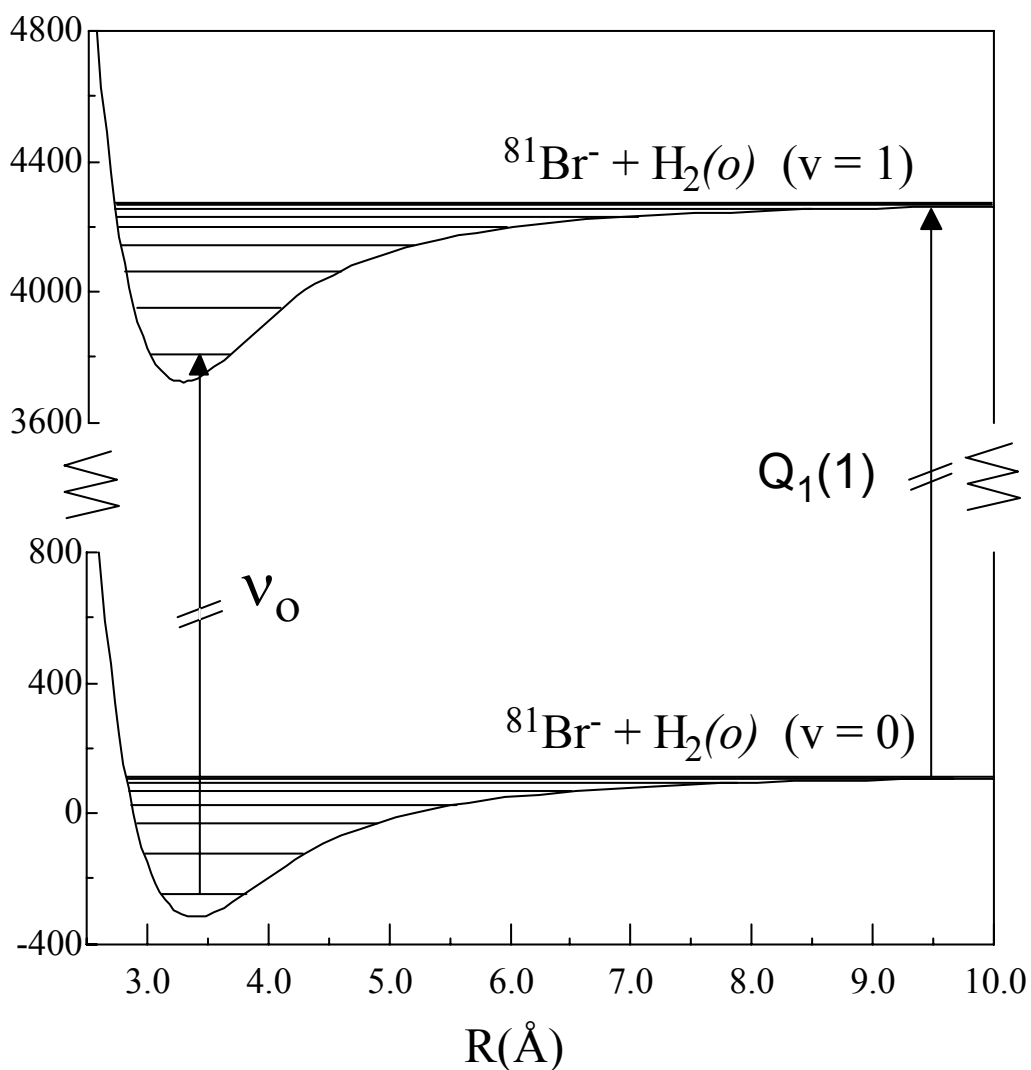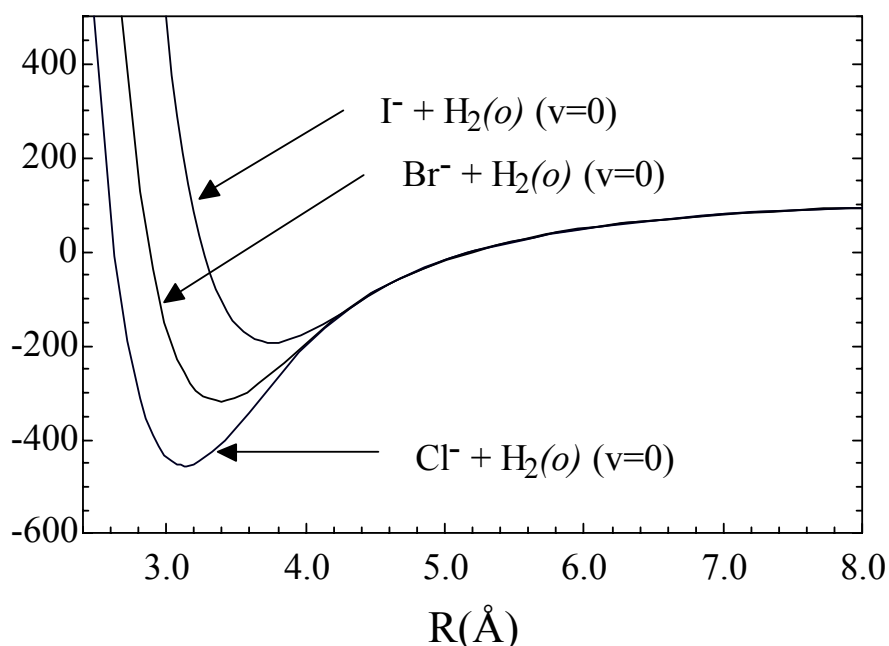

Figure 4.9: *BO–RKR potential energy curves for $Br^- + H_2(o)$ ($v = 0$) and $Br^- + H_2(o)$ ($v = 1$). Asymptotes of the $v = 1$ and $v = 0$ curves are separated by the energy of the H_2 $Q_1(1)$ transition (4155.25 cm^{-1}).[15] Parameters for both potentials are listed in Table 4.3.*

4.4.5 Comparison of halide–H₂ interactions

The radial intermolecular potential energy curves allow comparison of the vibrational band–shifts, intermolecular bond–lengths, and dissociation energies for the complexes as the halide anion is varied. The $\nu_{HH/DD}$ vibrational band shift can be interpreted as the difference between the binding energy for X^- interacting with the H_2/D_2 molecule in the $\nu_{HH/DD} = 0$ and $\nu_{HH/DD} = 1$ states. Encouragingly, the vibrational band shifts predicted from the BO–RKR potential curves only slightly underestimate the measured values. For example, $\Delta\nu_{BO-RKR} = -135$, -103, and -66 cm^{-1} compared to $\Delta\nu_{exp} = -150.4$, -110.8, and -74.1 cm^{-1} for $Cl^-–H_2$, $Br^-–H_2$ and $I^-–H_2$ respectively.

The dependence of the halide–hydrogen intermolecular interaction on the identity of the halide is perhaps most obvious when the BO–RKR radial intermolecular potentials for the X^- anions interacting with *ortho*–H_2 and *para*–D_2 are plotted in Figs. 4.10 and 4.11 respectively. While the long–range intermolecular interactions are almost identical (a consequence of their construction), the curves become noticeably shallower and have a larger equilibrium separation as the halide ion becomes larger.

Figure 4.10: *RKR–BO potential energy curves describing the $^{35}Cl^-$ + $H_2(o)$, $^{81}Br^-$ + $H_2(o)$ and I^- + $H_2(o)$ interactions. Parameters for the potentials are listed in Table 4.3.*
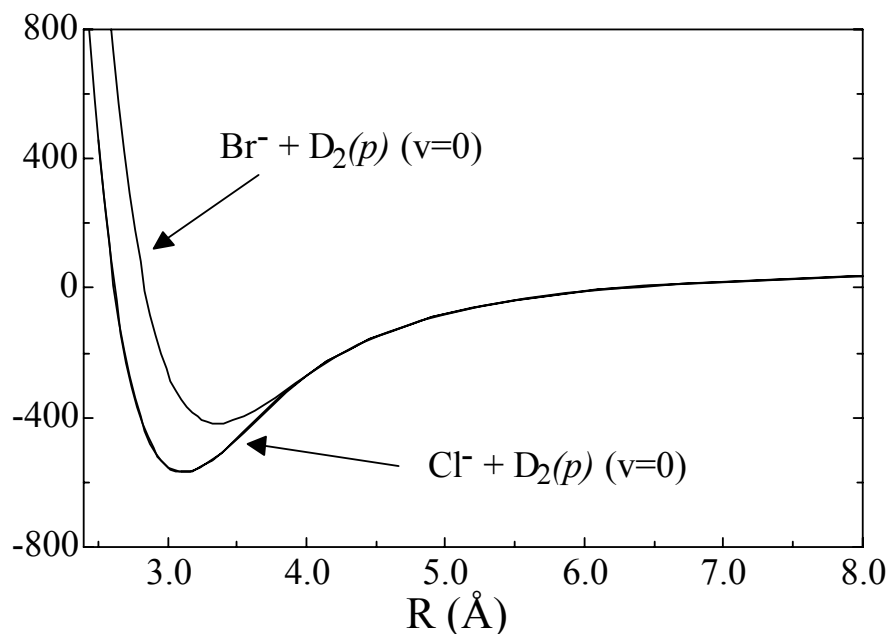
Figure 4.11: *RKR–BO potential energy curves describing the $^{35}Cl^- + D_2(p)$ and $^{79}Br^- + D_2(p)$ interactions. Parameters for the potentials are listed in Table 4.3.*

It is noteworthy that a linear correlation exists between the vibrationally averaged intermolecular separations in the halide–H_2 complexes and the intermolecular distances for the isoelectronic alkali halide diatomic molecules. This is apparent in Fig. 4.12 where the intermolecular separations for Cl^-–H_2, Br^-–H_2 and I^-–H_2 are plotted against the equilibrium bond–lengths for gas phase LiCl, LiBr, and LiI.[33–35] The X^-–H_2 intermolecular bonds become longer more rapidly than the alkali–halide bonds (the slope of the line is ~1.8), presumably a consequence of the weaker cohesive forces for the anion complexes (charge–quadrupole and induction interactions *vs* the Coulomb interaction for the alkali halides).
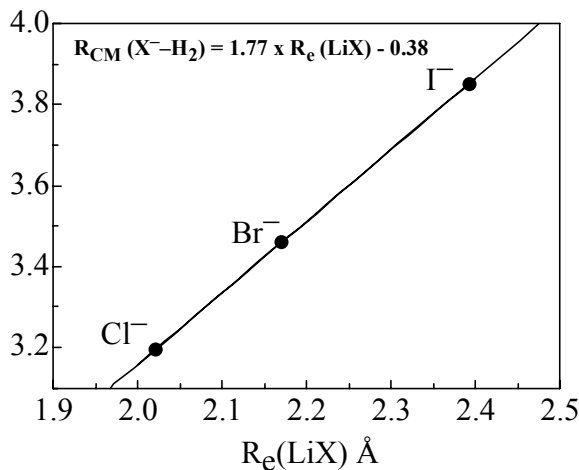
Figure 4.12: *Vibrationally averaged intermolecular separations (R_{cm}) for Cl^-–H_2, Br^-–H_2 and I^-–H_2 vs equilibrium bond lengths (R_e) of the isoelectronic LiCl, LiBr and LiI molecules.*

4.4.6 Comparison of X^-–H_2 and X^-–D_2 complexes

The BO–RKR potential energy curves highlight the differences between the halide–hydrogen and halide–deuterium intermolecular interactions. The curves predict larger binding energies for the D_2 containing complexes. The difference is principally due to the larger H_2 rotational constant, and consequent increased zero point bending motion. The greater deviations from linearity for the X^-–H_2 complexes makes the charge–quadrupole interaction less attractive, leading to smaller binding energies. This difference is revealed in the shapes of the BO–RKR curves, the Cl^-–H_2 curve is shallower with a larger equilibrium separation compared to the Cl^-–D_2 curve ($D_e = 574$ *vs* 630 cm^{-1}; $R_e = 3.130$ *vs* 3.114 Å). The larger bending excursions for the X^-–H_2 complexes are also manifested in smaller harmonic intermolecular stretching force constants compared with the X^-–D_2 complexes ($k_s'' = 2.9$ N/m for Cl^-–H_2 *vs* 3.8 N/m for Cl^-–D_2, and $k_s'' = 1.9$ N/m for Br^-–H_2 *vs* 2.4 N/m for Br^-–D_2).

4.4.7 Comparison of para and ortho–D_2 complexes

The data indicate that there are subtle differences between the interactions of X^- with *para* and *ortho*–D_2. These differences are illustrated in Fig. 4.13 where the curves for $Br^- + D_2(o)$ (v = 0) and $Br^- + D_2(p)$ (v = 0) interactions are plotted together. The two potential energy curves are virtually indistinguishable near the equilibrium separation, consistent with the fact that the rotational constants of Br^-–$D_2(o)$ and Br^-–$D_2(p)$ complexes are the same within experimental error (Table 4.1). At longer range, the potential energy curves deviate such that their asymptotes are separated by $\sim 2b''_{DD} = 59.8$ cm^{-1}. While the ground state intermolecular stretching levels for the two curves lie quite close to one another, the levels become increasingly separated as more quanta are added (Table 4.4).
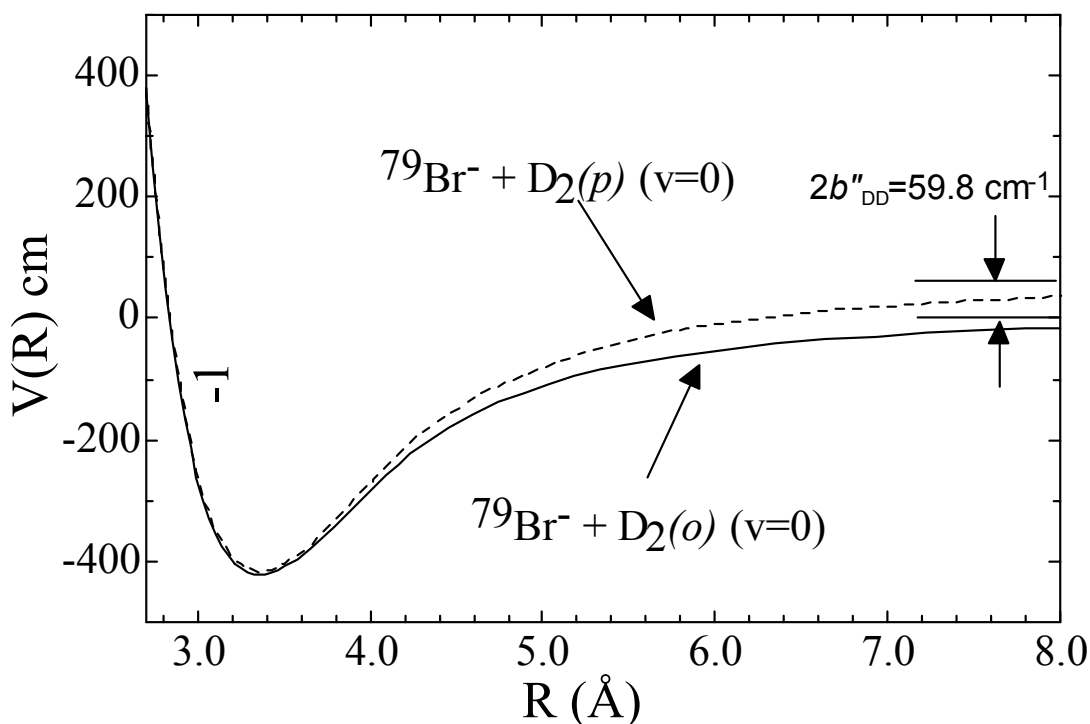
Figure 4.13: *Effective RKR–BO radial potential curves for $^{79}Br^-$ + $D_2(o)$ v = 0 (solid line) and $^{79}Br^-$ + $D_2(p)$ v = 0 (dashed line). Asymptotes for the two curves are separated by $\sim 2b''_{DD}$. Parameters for the two potentials are provided in Table 4.3.*

Comparison of the X^-–$D_2(o)$ and X^-–$D_2(p)$ potential energy curves indicate that there are some deficiencies in the BO–RKR procedure. As mentioned previously, internal rotation of the D_2 diatomic results in symmetric *ortho* levels that lie below the antisymmetric *para* levels. However, the BO–RKR Cl^-–$D_2(o)$ and Cl^-–$D_2(p)$ (v = 1) potential energy curves intersect between 3.0 and 4.0 Å such that the ground state for the v = 1 Cl^-–$D_2(p)$ curve lies $\sim$5 cm^{-1} *lower* than the ground state of the corresponding Cl^-–$D_2(o)$ curve. While the discrepancy is well within the estimated error bounds for the D_o values, it is evidence that the potential curves are not sufficiently accurate to quantitatively interpret the more subtle effects such as the *ortho/para* doubling observed in the spectra.

4.5 Infrared spectra of the F^-–$(D_2)_n$ and Cl^-–$(D_2)_n$ clusters

The discussion of the halide–hydrogen complexes now turns towards larger clusters with more than one deuterium molecule coordinated to the F^- and Cl^- anions. The evolution of the ν_{DD} vibrational frequencies as more D_2 ligands are added to the anion core provides information on the cluster solvation structures. It will be seen that the structures of the clusters are similar to those of the halide–acetylene clusters described in Chapter 3.

The infrared spectra of the F^-–$(D_2)_n$ (n = 1–6) and Cl^-–$(D_2)_n$ (n = 1–3) clusters are presented in Figs. 4.14 and 4.15 respectively. The spectrum of Cl^-–(D_2).Ar is also included in Fig. 4.15. For the fluoride–deuterium complexes, the n = 1–4 clusters' spectra were recorded by monitoring the F^-–$(D_2)_{n-1}$ dissociation channel, whereas the n = 5 and 6 spectra were recorded by monitoring the F^-–$(D_2)_{n-2}$ photofragment channel. Band wavenumbers, band shifts relative to the free D_2 stretch vibration, and band widths (fwhm) are listed in Table 4.5.
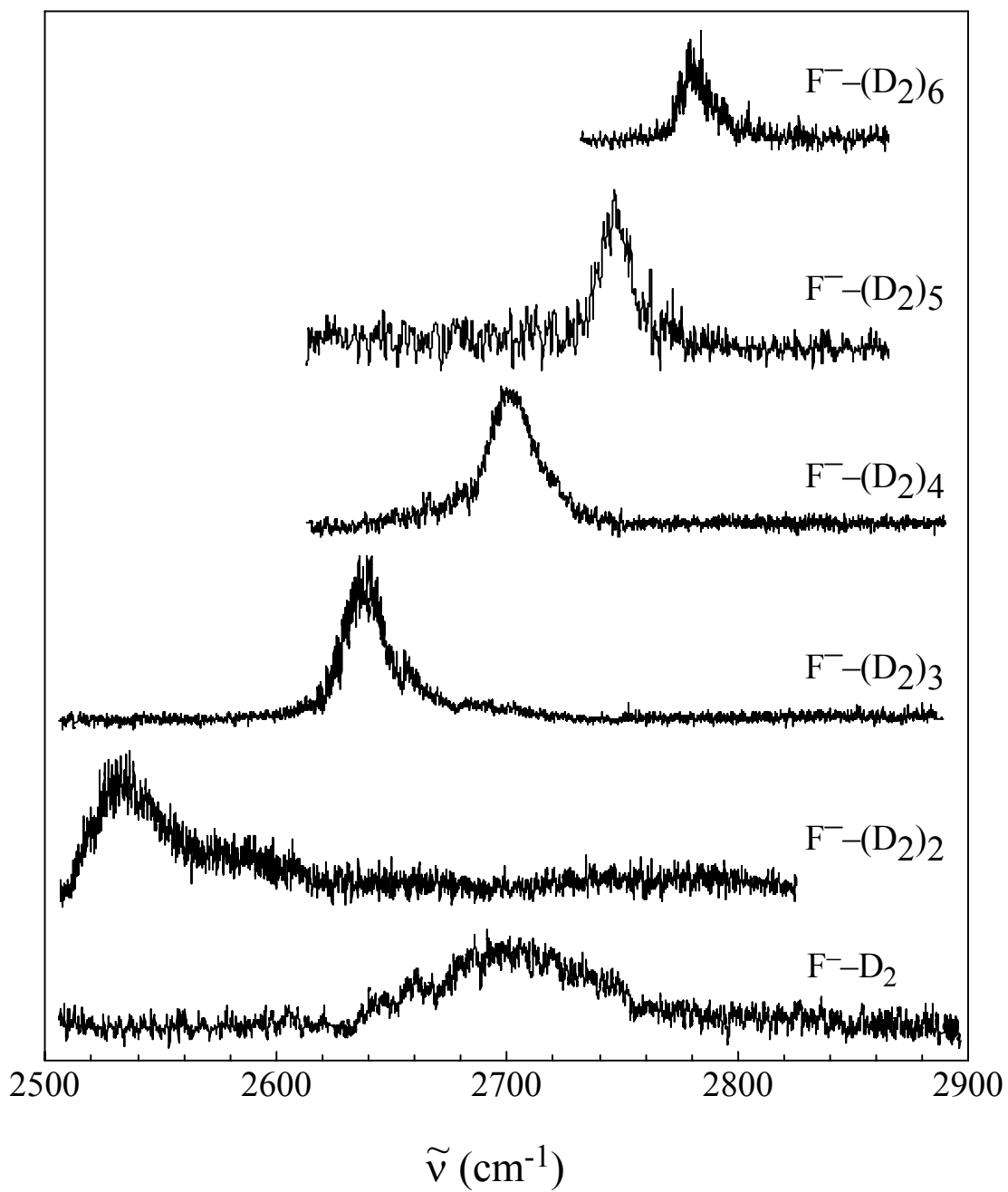
Figure 4.14: *Infrared spectra of F^-–$(D_2)_n$ clusters where n = 1–6. Spectroscopic data for each cluster are provided in Table 4.5.*
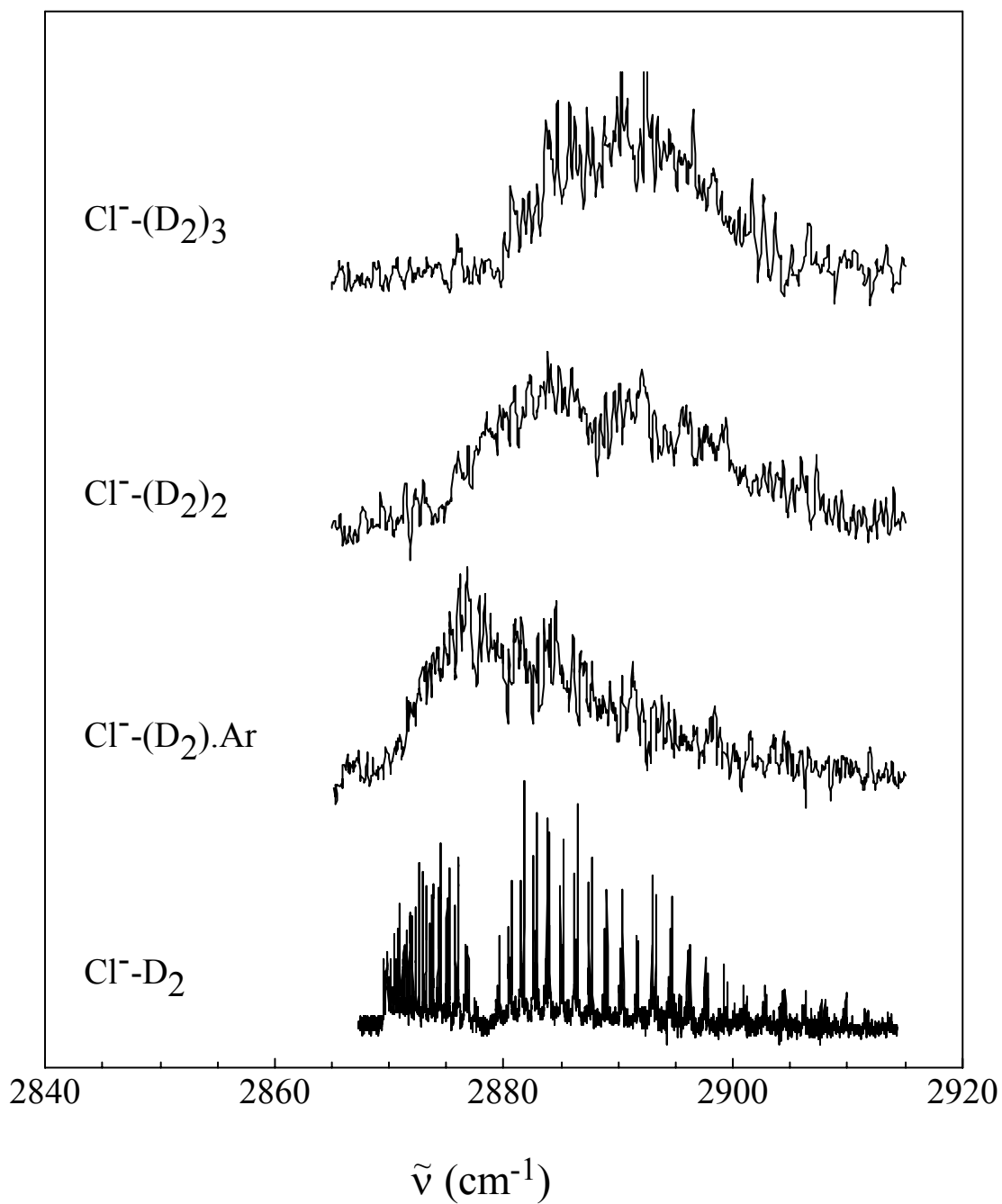
Figure 4.15: *Infrared spectra of $^{35}Cl^-–(D_2)_n$ clusters where n = 1–3. Spectroscopic data for each cluster are provided in Table 4.5. The spectrum of the $Cl^-–(D_2).Ar$ complex is also shown.*

Table 4.5: *Band positions, vibrational band shifts, and estimated band widths (fwhm) for the $F^-–(D_2)_n$ (n = 1–6) and $^{35}Cl^-–(D_2)_n$ (n = 1–3) clusters. Estimated uncertainties are given in parentheses.*

Cluster	Band Position (cm^{-1})	Band Shift[‡] (cm^{-1})	Band Width (cm^{-1})
$F^-–D_2$	2700(15)	–294	80
$F^-–(D_2)_2$	2537(10)	–457	40
$F^-–(D_2)_3$	2637(7)	–357	30
$F^-–(D_2)_4$	2706(7)	–288	25
$F^-–(D_2)_5$	2750(5)	–244	20
$F^-–(D_2)_6$	2780(5)	–214	18
$Cl^-–D_2(o)$	2878.75(8)	–114.8	N/A
$Cl^-–D_2(p)$	2878.51(8)	–113.0	N/A
$Cl^-–(D_2).Ar$	2880(5)	–114	18
$Cl^-–(D_2)_2$	2887(5)	–107	22
$Cl^-–(D_2)_3$	2891(5)	–103	18

[‡] The vibrational band shift for $Cl^-–D_2(p)$ is given with respect to the $Q_1(1)$ transition of the free D_2 molecule (2991.46 cm^{-1}; ref. 15). Shifts for the other bands are given with respect to the $Q_1(0)$ transition of the free D_2 molecule (2993.57 cm^{-1}; ref. 15)

4.5.1 $F^-–(D_2)_n$ and $Cl^-–(D_2)_n$.

The infrared spectra of the $F^-–(D)_n$ and $Cl^-–(D)_n$ clusters, except for $F^-–D_2$, contain a single band assigned to the D–D stretching modes. With the addition of more D_2 ligands to the halide anion, the band moves to higher frequency back towards the bare D_2 stretch band. This suggests that the intermolecular bond linking the ligands to the anion becomes progressively longer and weaker. The variation in D–D stretching frequencies is illustrated as a plot of the frequencies *vs* cluster size in Fig. 4.16.
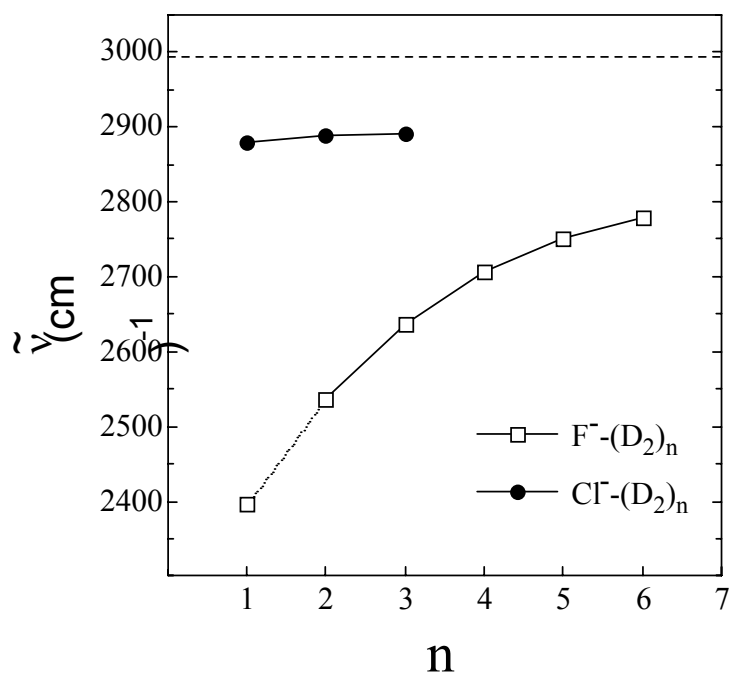
Figure 4.16: *Frequency of the D–D stretch band for $^{35}Cl^-–(D_2)_n$ and $F^-–(D_2)_n$ clusters vs ligand number. The dashed line corresponds to the frequency of bare D_2. The $F^-–D_2$ band position (2400 cm^{-1}) is estimated by extrapolating the $F^-–(D_2)_n$ ($2 \leq n \leq 6$) data (dotted line).*

Surprisingly, the band observed for the $F^-–D_2$ dimer does not fit the general trend. The band lies at ~2700 cm^{-1}, approximately 165 cm^{-1} to *higher* energy from the $F^-–(D_2)_2$ band. At this stage it seems likely that the $F^-–D_2$ band is associated with the D–D stretch mode in combination with the intermolecular stretch mode (ie, $\nu_{DD}+\nu_s$), implying that the ν_{DD} fundamental lies below 2500 cm^{-1}, outside the range of the OPO system. If the 2700 cm^{-1} band is indeed the $\nu_{DD}+\nu_s$ combination band, then the frequency of the ν_{DD} fundamental can be estimated as ~2460 cm^{-1} using the ν_s value of 243 cm^{-1} calculated by Boldyrev *et al.*[11] This compares reasonably well with the value of 2400 cm^{-1} obtained by extrapolating the band positions for the n = 2–6 spectra.

In the larger clusters, D_2 ligands that are H–bonded to the anion will avoid one another due to repulsive quadrupole–quadrupole interactions. This arrangement will be reinforced by repulsive interactions between the dipoles on the D_2 ligands induced by the anion's charge. For this reason it is anticipated that the $X^-–(D_2)_n$ clusters should posses

interior solvation structures in which the D_2 ligands are arranged about a central halide anion core.

To estimate the importance of the ligand–ligand repulsive interactions in influencing the clusters' structures, the quadrupole–quadrupole, induced dipole–induced dipole and induced dipole–permanent quadrupole interaction energies were estimated for two adjacent D_2 molecules in an octahedral complex. In this simple model, where the halide anion is represented as a point negative charge, the D_2–D_2 interaction energies depend solely on the halide–D_2 and D_2–D_2 bond lengths. The F^-–D_2 separation was taken from the *ab initio* F^-–H_2 equilibrium geometry of Boldyrev *et al.*[11] ($R_{cm} = 2.07$ Å), whereas the experimental vibrationally averaged Cl^-–D_2 intermolecular bond length ($R_{cm} = 3.16$Å) was used for the Cl^-——D_2 separation. The quadrupole moment and dipole polarizabilities were taken from ref. 14.

The induced dipole–induced dipole, induced dipole–quadrupole and quadrupole–quadrupole energies are $+365$, $+15$ and $+35$ cm^{-1} for the D_2–F^-–D_2 system and $+19$,$+12$ and $+4$ cm^{-1} for the D_2–Cl^-–D_2 system. Although several effects, such as the hindered rotation of the D_2 ligands, have been ignored it seems obvious that the repulsive interactions are sufficient to overwhelm the weak van der Waals attractions that might cause the D_2 subunits to congregate.

Cluster structures containing equivalent or near–equivalent D_2 ligands bonded end–on to a central halide anion are shown in Fig. 4.17. X^-–$(D_2)_2$ is predicted to be linear, X^-–$(D_2)_3$ trigonal planar, X^-–$(D_2)_4$ tetrahedral, X^-–$(D_2)_5$ trigonal bipyramidal, and X^-–$(D_2)_6$ octahedral. The clusters are expected to be floppy, undergoing substantial zero point excursions especially in the vibrational modes corresponding to hindered internal rotation of the D_2 subunits. The infrared spectra of the X^-–$(D_2)_{1-6}$ clusters are consistent with these proposed structures. The n = 1, 2, 3, 4, and 6 clusters shown in Fig 4.17 will each posses a single *IR* active collective D–D stretching mode (doubly degenerate for n = 3 and triply degenerate for n = 4 and 6). In the case of X^-–$(D_2)_5$ the two non–equivalent groups of ligands, corresponding to axial and equatorial positions, will be associated with two *IR* active collective D–D stretching modes (one singly degenerate and the other doubly degenerate). The appearance of a single relatively narrow band in the X^-–$(D_2)_5$ spectra suggests that the axial and equatorial D_2 ligands are similarly

perturbed by the anion. It is also possible that interconversion of the axial and equatorial ligands is a facile process, rendering the five ligands effectively equivalent to one another.
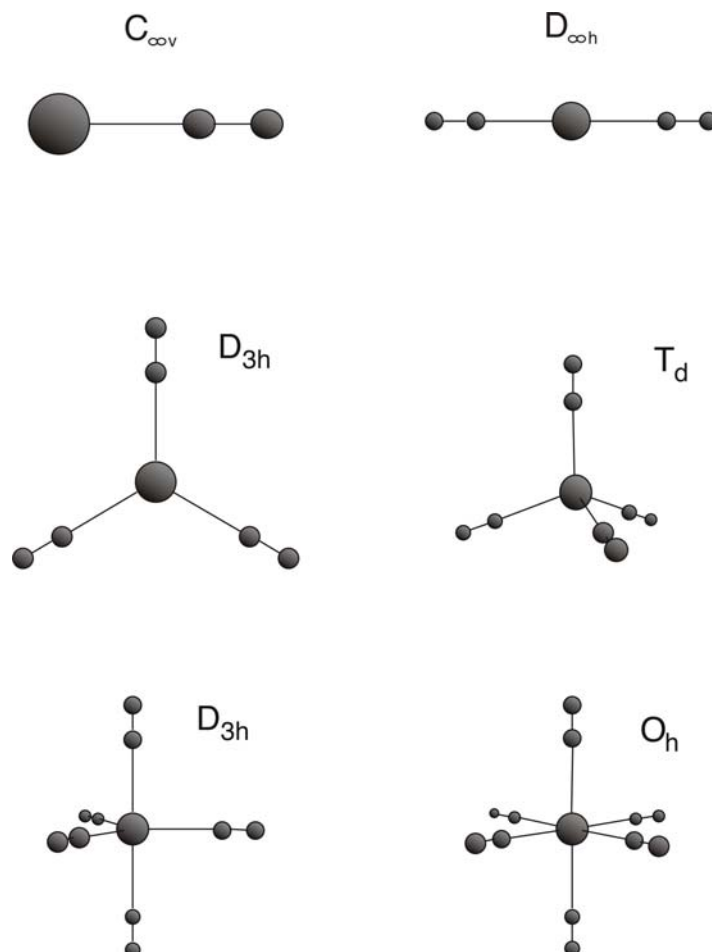
Figure 4.17: _Equilibrium structures proposed for the X^-–$(D_2)_n$ clusters derived from consideration of the infrared spectra and the dominant ligand–ion and ligand–ligand interactions._

There is no evidence from the spectra that occupation of the second solvation shell has commenced, as was observed in the infrared spectra of the Br^-–$(C_2H_2)_n$ and Cl^-–$(C_2H_2)_n$ clusters presented in Chapter 3. The spectra of the F^-–$(D_2)_n$ and Cl^-–$(D_2)_n$ clusters show no sign of bands to higher frequency that could be associated with ligands situated further from the anion core. Such bands should be weaker than those associated with D_2 ligands directly H–bonded to the halide, and hence may be obscured by the background noise. The evidence merely shows that the F^-–$(D_2)_n$ and Cl^-–$(D_2)_n$ clusters can accommodate *at least* six and three ligands respectively in their first solvation shells.

It is interesting to note that the contours of the D–D stretch bands become progressively more narrow and symmetric as the clusters become larger. These effects are most noticeable for the F^-–$(D_2)_n$ series (Fig. 4.14, Table 4.5). For example, the F^-–$(D_2)_2$ has a pronounced high energy tail and ~40 cm^{-1} width, whereas the corresponding F^-–$(D_2)_6$ band is almost symmetrical and has a width of ~18 cm^{-1}. The vibrational band narrowing is accounted for, at least in part, by the decrease in the clusters' rotational constants leading to more closing spaced rovibrational transitions. Another significant influence on the bands' widths and assymetries is related to the decreased displacement of hot bands from the ν_{DD} stretches as the clusters become larger. Hot bands of the type $\nu_{DD}+n\nu_s-n\nu_s$ and $\nu_{DD}+n\nu_b-n\nu_b$ are expected to occur to higher energy from ν_{DD} due to the strengthening of the halide–D_2 bonds upon excitation of the ν_{DD} modes. This is principally due to the increase in the quadrupole moment and polarizabilities of D_2 in the vibrationally excited state.[14] With increasing cluster size, the intermolecular bonds become longer and weaker, and excitation of the D–D stretch mode will have a smaller effect on the F^-——D_2 potential, diminishing the offset of the hot bands from the ν_{DD} fundamental.

4.5.2 Comparison of Cl^-–D_2 and Cl^-–(D_2).Ar

The *IR* spectrum of the Cl^-–D_2 dimer has already been discussed in section 4.3. Briefly, the spectrum displays two overlapping, rotationally resolved, Σ–Σ subbands (separated by 0.24 cm^{-1}) shifted to lower frequency from the bare D_2 stretch. The Σ–Σ band structure indicates that the complex possesses a linear equilibrium geometry, although the zero point stretching and bending motions are substantial. The rotational constants obtained from the analysis are consistent with a vibrationally averaged separation of 3.16 Å, contracting by 0.08 Å when the D–D stretch mode is excited.

The *IR* spectrum of the Cl^-–(D_2).Ar complex was measured in an effort to gauge the effect of argon solvation on the Cl^-–D_2 dimer. The spectrum, which was recorded by monitoring the Cl^-–Ar photofragment, features a single band that retains the asymmetric blue degraded form of the Cl^-–D_2 dimer spectrum. Although the poor S/N ratio of the spectrum makes it difficult to precisely locate the band origin it appears that addition of the argon atom has minimal effect on the D–D stretching mode. The argon induced band

shift is quite small (< 5 cm^{-1}), comparable to the band shifts observed for argon–solvated hydrated halide systems[36–38] and the Cl$^-$–(C$_2$H$_2$).Ar$_n$ complexes presented in Chapter 3.

There are interesting differences in the fragmentation pattern of Cl$^-$–(D$_2$).Ar following either collisional or photon excitation. Collision induced dissociation by residual gas in the octopole ion guide resulted in equal quantities of Cl$^-$–D$_2$ and Cl$^-$–Ar fragments, consistent with the fact that the binding energies of Cl$^-$–Ar and Cl$^-$–D$_2$ are similar (D_o'' ($Cl^- - Ar$) $\sim$500 cm^{-1}; ref. 39). In contrast, *IR* excitation of the D–D stretch vibration results exclusively in Cl$^-$–Ar fragment ions. Although the energy of a single quantum of the D–D stretch vibration is more than sufficient to break the complex into Cl$^-$ + D$_2$ + Ar fragments, it seems that little of the available energy is transferred to the Cl$^-$–Ar bond. This observation suggests that the D–D vibrational energy is transferred directly to the Cl$^-$——D$_2$ bond, followed by prompt loss of the D$_2$ molecule. Conservation of energy and momentum ensures that the light D$_2$ molecule departs with most of the excess energy, leaving insufficient energy to rupture the Cl$^-$——Ar bond.

4.5.3 Comparisons with matrix isolation spectra of CsF:D$_2$

It is worthwhile comparing the *IR* spectra of the F$^-$–(D$_2$)$_2$ and F$^-$–(D$_2$)$_3$ clusters with the Ar matrix isolation spectra of Sweany *et al.*[4] Features observed in matrix spectra recorded with large D$_2$ concentrations codeposited with CsF were assigned to the D–D stretching vibrations of multiple D$_2$ ligands attached to the CsF ion pair. It was suggested from the small changes in the spectra upon changing the identity of the alkali cation that the D$_2$ ligands predominantly interact with the halide anion of the alkali–halide ion pair. The matrix spectra contained bands at 2892 and 2895 cm^{-1} assigned to the CsF(D$_2$)$_2$ complex, while a band at 2897 cm^{-1} was assigned to the CsF(D$_2$)$_3$ complex. These bands occur at higher frequency than the corresponding D–D stretching bands of the gas phase F$^-$–(D$_2$)$_2$ and F$^-$–(D$_2$)$_3$ complexes (2537 cm^{-1} and 2637 cm^{-1} respectively). It appears that the D$_2$ molecules in the rare–gas matrix are not coordinated solely to the anion of the alkali–halide ion pair. It is also likely that the CsF diatomic is not fully ionic in the matrix, and hence the charge on the F atom is not -1. The gas phase results therefore better represent the vibrational frequencies of F$^-$–(D$_2$)$_2$ and F$^-$–(D$_2$)$_3$, as the

clusters are mass selected prior to spectroscopic interrogation and are therefore free from matrix perturbations.

4.6 Summary

Infrared spectra of the gas phase halide–hydrogen anion complexes recorded in the vicinity of the H–H (D–D) stretch feature Σ–Σ type bands, characteristic of linear complexes.   Analysis of the rovibrational transitions allow the determination of vibrationally averaged intermolecular separations, harmonic intermolecular stretching frequencies and intermolecular stretching force constants.   The data indicate that the systems can be viewed as weakly bound complexes in which the hydrogen molecule essentially maintains its structural integrity. Support for this contention comes from the observations that the H–H and D–D stretch bands are only marginally displaced from the transition of the free H_2 molecule and that the only observed photo–fragments are halide anions.   The alternative XH–H$^-$ structures should lie much higher in energy as the proton affinity (PA) of H$^-$ considerably exceeds those of Cl$^-$, Br$^-$ and I$^-$.

Effective one–dimensional radial intermolecular potential energy curves describing the $X^- + H_2(D_2)$ interactions were developed. These curves allowed estimates of binding energies and intermolecular stretching frequencies and highlighted the decreasing strength of the intermolecular interaction as the size of the halide anion increased.

The *IR* spectra of the larger F$^-$–(D$_2$)$_n$ (n = 2–6) and Cl$^-$–(D$_2$)$_n$ (n = 1–3) clusters contain a single band that is shifted to higher energy with the addition of more D$_2$ ligands to the halide core. This trend is consistent with interior solvation structures containing roughly equivalent D$_2$ ligands. Interior solvation structures are expected, as D$_2$ ligands bound to the anion core will repel one another due to quadrupole–quadrupole, induced dipole–induced dipole and induced dipole–quadrupole interactions.

4.7 References

1. M. S. Huq, D. S. Fraedrich, L. D. Doverspike, R. L. Champion and V. A. Esaulov, J. Chem. Phys. **76**, 4952 (1982)

2. J. A. Fayeton, J. C. Brenot, M. Durup–Ferguson and M. Barat, Chem. Phys. **133**, 259 (1989)

3. M. L. McKee and R. L. Sweany, J. Phys. Chem. **104**, 962 (2000)

4. R. L. Sweany and J. S. Ogden, Inorg. Chem. **36**, 2523 (1997)

5. J. S. Ogden, A. J. Rest and R. L. Sweany, J. Phys. Chem. **99**, 8485 (1995)

6. J. Z. H. Zhang, W. H. Miller, A. Weaver and D. Neumark, Chem. Phys. Lett. **182**, 283 (1991)

7. S. E. Bradforth, D. W. Arnold, D.M. Neumark and D. E. Manolopoulos, J. Chem. Phys. **99**, 6345 (1993)

8. D. M. Neumark, Acc. Chem. Res. **26**, 33 (1993)

9. M. J. Ferguson, G. Meloni, H. Gomez and D. M. Neumark, J. Chem. Phys. **117**, 8181 (2002)

10. J. A. Nichols, R. A. Kendall, S. J. Cole and J. Simons, J. Phys. Chem. **95**, 1074 (1991)

11. A. I. Boldyrev, J. Simons, G. V. Mil'nikov, V. A. Benderskii, S. Y. Grebenshchikov and E. V. Vetoshkin, J. Chem. Phys. **102**, 1295 (1995)

12. A. D. Buckingham, in *Intermolecular forces: Advances in Chemical Physics*, edited by J. O. Hirschfelder (Wiley and Sons, New York, 1967)

13. G. C. Pimentel and A. L. McClellan, *The Hydrogen Bond* (W.H. Freeman, New York, 1960)

14. J. L. Hunt, J. D. Poll and L. Wolniewicz, Can. J. Phys. **62**, 1719 (1984)

15. K. P. Huber and G. Herzberg, *Molecular Spectra and Molecular Structure IV: Constants of Diatomic Molecules* (van Nostrand Reinhold, New York, 1979)

16. P. S. Weiser, D. A. Wild, P. P. Wolynec and E. J. Bieske, J. Phys. Chem. **104**, 2562 (2000)

17. D. A. Wild, Z. M. Loh, P. P. Wolynec, P. S. Weiser and E. J. Bieske, Chem. Phys. Lett. **332**, 531 (2000)

18. S. A. Nizkorodov, J. P. Maier and E. J. Bieske, J. Chem. Phys. **102**, 5570 (1995)

19. S. A. Nizkorodov, J. P. Maier and E. J. Bieske, J. Chem. Phys. **103**, 1297 (1995)

20. R. V. Olkhov, S. A. Nizkorodov and O. Dopfer, J. Chem. Phys. **107**, 8229 (1997)

21. E. J. Bieske, S. A. Nizkorodov, F. R. Bennett and J. P. Maier, J. Chem. Phys. **102**, 5152 (1995)

22. D. J. Millen, Can. J. Chem. **63**, 1477 (1985)

23. D. Hanstorp and M. Gustafsson, J. Phys. B. **25**, 1773 (1992)

24. J. D. D. Martin and J. W. Hepburn, J. Chem. Phys. **109**, 8139 (1998)

25. C. Blondel, P. Cacciani, C. Delsart and R. Trainham, Phys. Rev. A. **40**, 3698 (1989)

26. S. T. Pratt, E. F. McCormack, J. L. Dehmer and P. M. Dehmer, Phys. Rev. Lett. **68**, 584 (1992)

27. S. Scheiner, *Hydrogen Bonding. A Theoretical Perspective* (Oxford University Press, Oxford, U.K., 1997)

28. T. Ruchti, A. Rohrbacher, T. Speck, J. P. Connelly, E. J. Bieske and J. P. Maier, Chem. Phys. **209**, 169 (1996)

29. M. S. Child and D. J. Nesbitt, Chem. Phys. Lett. **149**, 404 (1988)

30. D. J. Nesbitt, M. S. Child and D. C. Clary, J. Chem. Phys. **90**, 4855 (1989)

31. J. D. Poll and J. L. Hunt, Can. J. Phys. **63**, 84 (1985)

32. University of Waterloo Chemical Physics Research Report No. CP–642 , 2000,

33. A. J. Hebert, F. W. Breivogel Jr. and K. Street Jr., J. Chem. Phys. **41**, 2368 (1964)

34. F. W. Breivogel Jr, A. J. Hebert and K. Street Jr., J. Chem. Phys. **42**, 1555 (1965)

35. W. Gordy and E. F. Pearson, Phys. Rev. **177**, 52 (1969)

36. J. A. Kelly, J. M. Weber, K. M. Lisle, W. H. Robertson, P. Ayotte and M. A. Johnson, Chem. Phys. Lett. **327**, 1 (2000)

37. P. Ayotte, J. A. Kelly, S. B. Nielsen and M. A. Johnson, Chem. Phys. Lett. **316**, 455 (2000)

38. P. Ayotte, G. H. Weddle, J. Kim and M. A. Johnson, Chem. Phys. **239**, 485 (1998)

39. T. Lenzer, L. Yourshaw, M. R. Furlanetto, G. Reiser and D. M. Neumark, J. Chem. Phys. **110**, 9578 (1999)

Chapter 5: The Halide–Methane Anion Complexes

5.1 Introduction

The work detailed in this chapter concerns the gas phase complexes formed from halide anions and neutral methane molecules. The halide–methane complexes are part of a class of atom–tetrahedral molecule complexes that have received recent theoretical and experimental attention. Studies have embraced Ar–CH$_4$ (refs. 1 and 2), Ar–SiH$_4$ (refs. 3 and 4), Ar–NH$_4^+$ (refs. 5–8), Ne–NH$_4^+$ (ref. 8), and He–NH$_4^+$ (refs. 8 and 9). The structural and vibrational properties of these complexes critically depend on the cluster binding energies and the barriers to internal rotation of the tetrahedral molecule. The experiments discussed in this chapter aim to address the following questions. What are the structures for the halide–methane complexes? Are the complexes rigid, or is internal rotation of the methane sub–unit a facile process? What effect does complex formation have on the vibrational modes of bare methane?

Early investigations of the halide–methane complexes have focussed on gas phase reactions between the halide anions and methane molecules, via beam techniques. Energy dependent cross sections were measured for the $Br^- + CH_4$ reaction,[10] which was presumed to proceed via an S$_N$2 transition state. The major pathways were found to be H$_2$ elimination and the S$_N$2 reaction:

$$Br^- + CH_4 \rightarrow [Br^- - CH_4] \rightarrow BrCH_2^- + H_2$$
$$\rightarrow BrCH_3 + H^- \qquad [1]$$
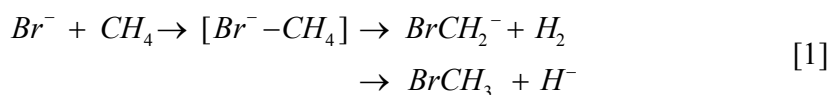
The energy of the reactants, reaction products and pathways were calculated for the $F^- + CH_4$ reaction employing the primitive MINDO–3FORCES method.[11] These calculations predicted two reaction intermediates with C$_{3v}$ symmetry, the bipyramidal distorted structure (S$_N$2 intermediate), and a structure with the fluoride bound to a single hydrogen. Activation energies were calculated for the inversion, H$_2$ elimination, and proton abstraction reactions.

In later theoretical studies, Novoa *et al*[12] addressed the halide–methane complexes using SCF and MP2 *ab initio* calculations employing the 6–31++G(d,p) basis set. The relative energies of the vertex, face and edge–bound structures shown in Fig. 5.1 were calculated, with the vertex–bound complex found to be the minimum

energy structure. The edge and face structures represent first and second order stationary points for the internal rotation of the methane sub–unit. Differences in the energies of the three structures provide estimates for the barriers to tunnelling between the four equivalent vertex bound structures. The most facile tunnelling pathway is via the C_{2v} edge bound structure (Fig. 5.1.c), with estimated barriers of ~1070, ~470, and ~460 cm^{-1} for F^-–CH_4, Cl^-–CH_4, and Br^-–CH_4 respectively.
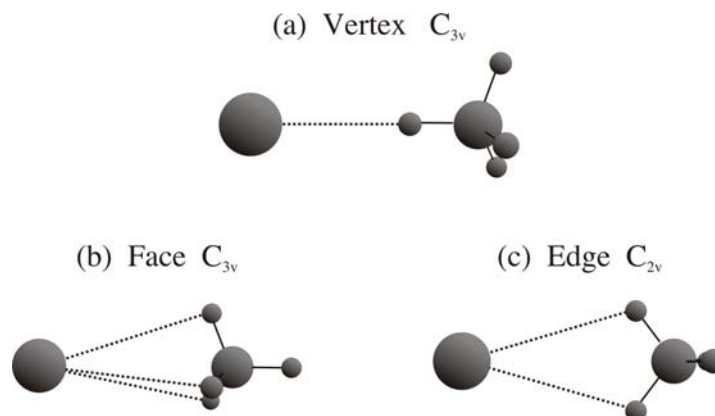
Figure 5.1: *Structures for the halide–methane dimer complex. The structures correspond to the anion being situated at the vertex, face and edge of the CH_4 tetrahedron. The vertex–bound structure is the minimum energy configuration while the edge and face structures are first and second order stationary points.*

Recently, the binding energies of the halide–methane dimer complexes and the larger X^-–$(CH_4)_n$ clusters were determined using high pressure mass spectrometry (HPMS).[13] The experimentally determined binding energies of the X^-–CH_4 dimer complexes decrease in the order $F^- >> Cl^- > Br^- > I^-$, and compare reasonably well with the energies predicted by Novoa *et al*[12] for the C_{3v} vertex–bound structures. The X^-...CH_4 binding energies decrease as more CH_4 ligands are coordinated with the halide anion to form larger X^-–$(CH_4)_n$ clusters. Our group has performed *ab initio* calculations to determine the structures and vibrational frequencies of the Cl^-–CH_4 complex at the MP2(full)/aug–cc–pVTZ level, to compare with the vibrational predissociation spectra.[14] A vertex–bound minimum energy structure was found, in agreement with the results of Novoa *et al*[12] .

Vibrations of CH$_4$ and X$^-$–CH$_4$

In the following, the fundamental vibrations of bare methane are described. Subsequently the effect of the halide anion on these vibrations is examined. Methane (T$_d$ symmetry) possesses the nine fundamental vibrations shown in Fig. 5.2. These modes correspond to the $\nu_1(a_1)$ symmetric stretching mode, the doubly degenerate $\nu_2(e)$ bending mode, the triply degenerate antisymmetric stretching mode $\nu_3(f_2)$, and the triply degenerate bending mode $\nu_4(f_2)$.
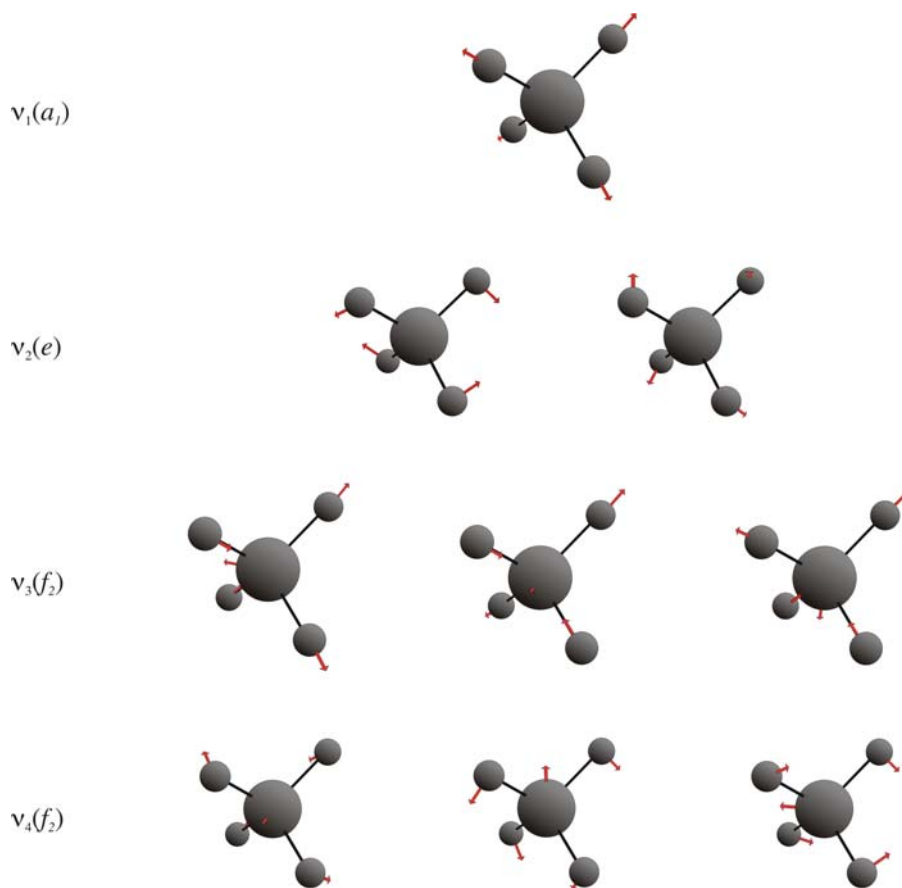
Figure 5.2: *Atomic displacements for the normal vibrational modes of the methane molecule.*

Formation of the vertex bound halide–methane complex (Fig. 5.1.a) reduces the local symmetry of the methane molecule from T$_d$ to C$_{3v}$. The two triply degenerate modes ν_3 and ν_4 (f_2 symmetry) each split into a singly degenerate a_1 symmetry mode and a doubly degenerate e symmetry mode. The $\nu_1(a_1)$ stretching mode and $\nu_2(e)$ bending mode retain the same symmetry. Two additional modes are

introduced following complex formation, the intermolecular stretching mode $\nu_s(a_1)$, and the doubly degenerate bend mode $\nu_b(e)$.   The transformation of the methane modes are summarised in Table 5.1.   The fundamental vibrational modes of the vertex–bound halide–methane complex are shown in Fig. 5.3.

Table 5.1: *Transformation of the fundamental modes of methane upon formation of the vertex bound X^-–CH_4 complex. Provided are the mode symmetries, frequency shifts ($\Delta\tilde{\nu}$) and infrared intensities (Int.)*

CH_4 (T_d)				X^-–CH_4 (C_{3v})		
Mode	$\tilde{\nu}$[♦]	Int.[‡]		Mode	$\Delta\tilde{\nu}$[◊]	Int.[‡]
$\nu_1(a_1)$	2914.2	0	$\rightarrow$	$\nu_1(a_1)$	R	VS
$\nu_2(e)$	1534	0	$\rightarrow$	$\nu_2(e)$	B	W
$\nu_3(f_2)$	3019.5	S	$\rightarrow$	$\nu_3(a_1)$	R	W
			$\rightarrow$	$\nu_3(e)$	R	S
$\nu_4(f_2)$	1306.2	M	$\rightarrow$	$\nu_4(a_1)$	R	M
			$\rightarrow$	$\nu_4(e)$	B	W
				$\nu_s(a_1)$	–	M
				$\nu_b(e)$	–	W

♦ CH_4 frequencies are taken from ref. 15
◊ R = red shift, B = blue shift.
‡ VS = very strong, S = strong, M = medium, W = weak, 0 = *IR* inactive.
Band shifts and *IR* intensities are taken from ref. 14

Methane Modes

$\nu_1(a_1)$

$\nu_2(e)$ $\nu_2(e)$

$\nu_3(a_1)$ $\nu_3(e)$ $\nu_3(e)$

$\nu_4(a_1)$ $\nu_4(e)$ $\nu_4(e)$

Intermolecular Modes

$\nu_s(a_1)$ $\nu_b(e)$ $\nu_b(e)$
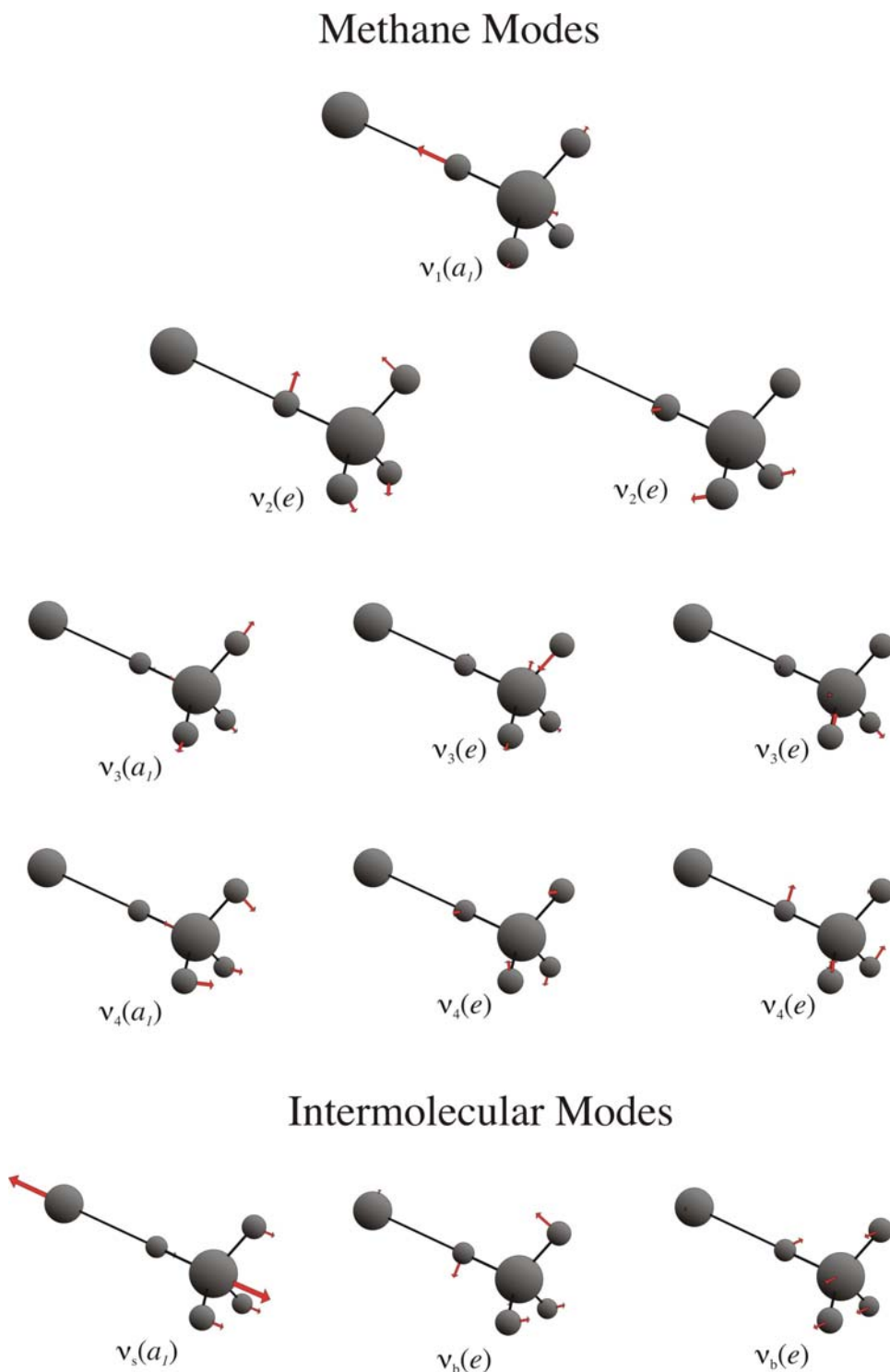
Figure 5.3: *Vibrational normal modes for the vertex bound halide–methane complex. The modes are separated into those that involve distortion of the methane ligand, and intermolecular modes involving distortion of the intermolecular bond. The numbering of the methane normal modes reflects their parentage in the bare CH$_4$ molecule.*

The work detailed in this chapter concerns the C–H stretching modes $\nu_1(a_1)$, $\nu_3(a_1)$, and $\nu_3(e)$ that occur in the mid–infrared region (~ 3000 cm^{-1}). The $\nu_3(a_1)$ and $\nu_3(e)$ modes principally involve motion of the three non–bonded hydrogens. Excitation of the singly degenerate $\nu_3(a_1)$ mode results in a parallel transition, with rotational selection rules $\Delta J = \pm 1$ and $\Delta K = 0$. The band will be comprised of several overlapping sub–bands, corresponding to separate $K = 0, 1, 2\ldots$ states, with each displaying P and R branches. Excitation of the doubly degenerate $\nu_3(e)$ mode results in a perpendicular transition, with the rotational selection rules $\Delta J = \pm 1, 0$ and $\Delta K = \pm 1$. This band should be recognisable by the presence of prominent Q–branches ($\Delta J = 0$, $\Delta K = \pm 1$).

For the halide–methane complex the $\nu_1(a_1)$ mode corresponds to motion of the shared or intermediate hydrogen. The infrared inactive $\nu_1(a_1)$ mode of bare methane is predicted to become strongly *IR* active when the molecule is attached to the halide anion.[12] Exciting this mode results in a parallel transition, with rotational selection rules $\Delta J = \pm 1$, $\Delta K = 0$. The $\nu_1(a_1)$ band will have the same form as the $\nu_3(a_1)$ band, however will be strongly red shifted due to a reduction in the force constant of the H–bonded C–H group.[16] The red shift of the $\nu_1(a_1)$ band reflects the strength of the intermolecular interaction, with a larger shift correlating with a stronger interaction. Based on these considerations, the mid–infrared spectrum of the halide–methane complexes is expected to contain three bands.

The fine structure of these bands may be affected by internal rotation of the methane sub unit[12] which is expected to be significant due to the low barriers to CH$_4$ internal rotation. Tunnelling between equivalent vertex bound minima can occur via the edge transition state depicted in Fig. 5.1.c and will lead to a splitting of the rovibrational energy levels. For infinite tunnelling barriers, the complex resembles a rigid prolate symmetric top, while at the other extreme, for no barrier to internal rotation, the methane is a free rotor and the rovibrational energy levels of the complex will resemble those of bare methane. In reality, the tunnelling barrier lies between these two extremes and depends on the relative energies of the minimum energy

vertex bound structure (Fig. 5.1.a) and the edge transition state (Fig. 5.1.c) (~1070, ~470, and ~460 cm^{-1} for F$^-$–CH$_4$, Cl$^-$–CH$_4$, and Br$^-$–CH$_4$ respectively; ref. 12)

The effects of internal rotation on the energy level structure and infrared spectra have been investigated for the Ar–NH$_4{}^+$ (refs. 5–7) and He–NH$_4{}^+$ (refs. 8 and 9) atom–tetrahedral molecule cation complexes. *Ab initio* calculations suggest that He–NH$_4{}^+$ is quite loosely bound ($D_e \approx 150$ cm^{-1}), with a barrier to internal rotation less than 30 cm^{-1}.[9]   It is therefore not surprising that apart from a small shift in frequency (~ 0.7 cm^{-1}), the infrared spectrum of the complex closely resembles that of bare NH$_4{}^+$.   In contrast the Ar–NH$_4{}^+$ complex is more strongly bound ($D_e \sim 930$ cm^{-1}) with a barrier to internal rotation via the edge transition state of ~200 cm^{-1}.   The infrared spectrum is complicated by rovibrational transitions originating from the various tunnelling energy levels. The halide–methane and Ar–NH$_4{}^+$ complexes have similar binding energies, and therefore it is conceivable that tunnelling may also be significant and could affect the vibrational and structural properties of the complexes.

The remainder of this chapter begins with a brief description of the experimental conditions employed to produce and interrogate the halide–methane gas phase complexes. The mid–infrared spectra of the halide–methane complexes are then presented. This is followed by a discussion of the form of the bands. Finally, the vibrational and structural properties of the halide–methane complexes are compared with the isoelectronic halide–ammonia and halide–water complexes.

5.2 Experimental

The halide–methane dimer complexes were produced from a gas mixture consisting of traces of the halide ion precursors (NF$_3$, CCl$_4$, CH$_2$Br$_2$) seeded in approximately 1:50 CH$_4$:Ar. Spectra were recorded over the 2500–3100 cm^{-1} range by monitoring the intensity of the X$^-$ photo–fragment *vs IR* wavenumber. The spectra are the average of a number of separate scans. The wavenumbers of the Q branch lines were corrected for the Doppler shift arising from the ions' ~10 eV kinetic energy in the octopole region of the apparatus. The Doppler corrections were +0.07, +0.06, and +0.05 cm^{-1} for F$^-$–CH$_4$, ^{35}Cl$^-$–CH$_4$, ^{79}Br$^-$–CH$_4$ respectively.

5.3 Halide–methane dimers

Infrared spectra for F^-–CH_4, $^{35}Cl^-$–CH_4 and $^{79}Br^-$–CH_4 recorded over the 2700–3100 cm^{-1} range are presented in Fig. 5.4. Stick vibrational spectra based on the calculation of Novoa *et al.*[12] and Wild *et al.*[14] are included for comparison. The calculated harmonic frequencies are scaled by the factors required to bring the calculated bare methane frequencies in line with the experimental values. Spectroscopic data for the three complexes are provided in Table 5.2.

Table 5.2: *Spectroscopic data for the F^-–CH_4, $^{35}Cl^-$–CH_4 and $^{79}Br^-$–CH_4 dimers. The $\nu_1(a_1)$ band positions, and $\nu_3(e)$ Q–branch positions are provided. The Q–branch wavenumbers have ± 0.5 cm^{-1} uncertainties, while uncertainties in the $\nu_1(a_1)$ band positions are estimated to be ± 5 cm^{-1}.*

	Assignment	F^-–CH_4	Cl^-–CH_4	Br^-–CH_4
$\nu_1(a_1)$	head	2522.0 ± 0.5		
	origin	2535	2874	2883
$\nu_3(e)$	$^PQ_9$	2881.2		
	$^PQ_8$	2890.8		
	$^PQ_7$	2900.5		
	$^PQ_6$	2910.0		
	$^PQ_5$	2919.0		
	$^PQ_4$	2927.7	2947.1	
	$^PQ_3$	2935.5	2957.1	2961.4
	$^PQ_2$	2942.7	2966.8	2971.2
	$^PQ_1$	2947.8	2976.7	2980.9
	$^RQ_0$	2956.0	2986.5	2990.6
	$^RQ_1$	2964.1	2996.1	2999.5
	$^RQ_2$	2972.8	3005.6	3007.9
	$^RQ_3$	2981.5	3015.3	3016.8
	$^RQ_4$	2990.5		
	$^RQ_5$	2999.2		
	$^RQ_6$	3008.0		
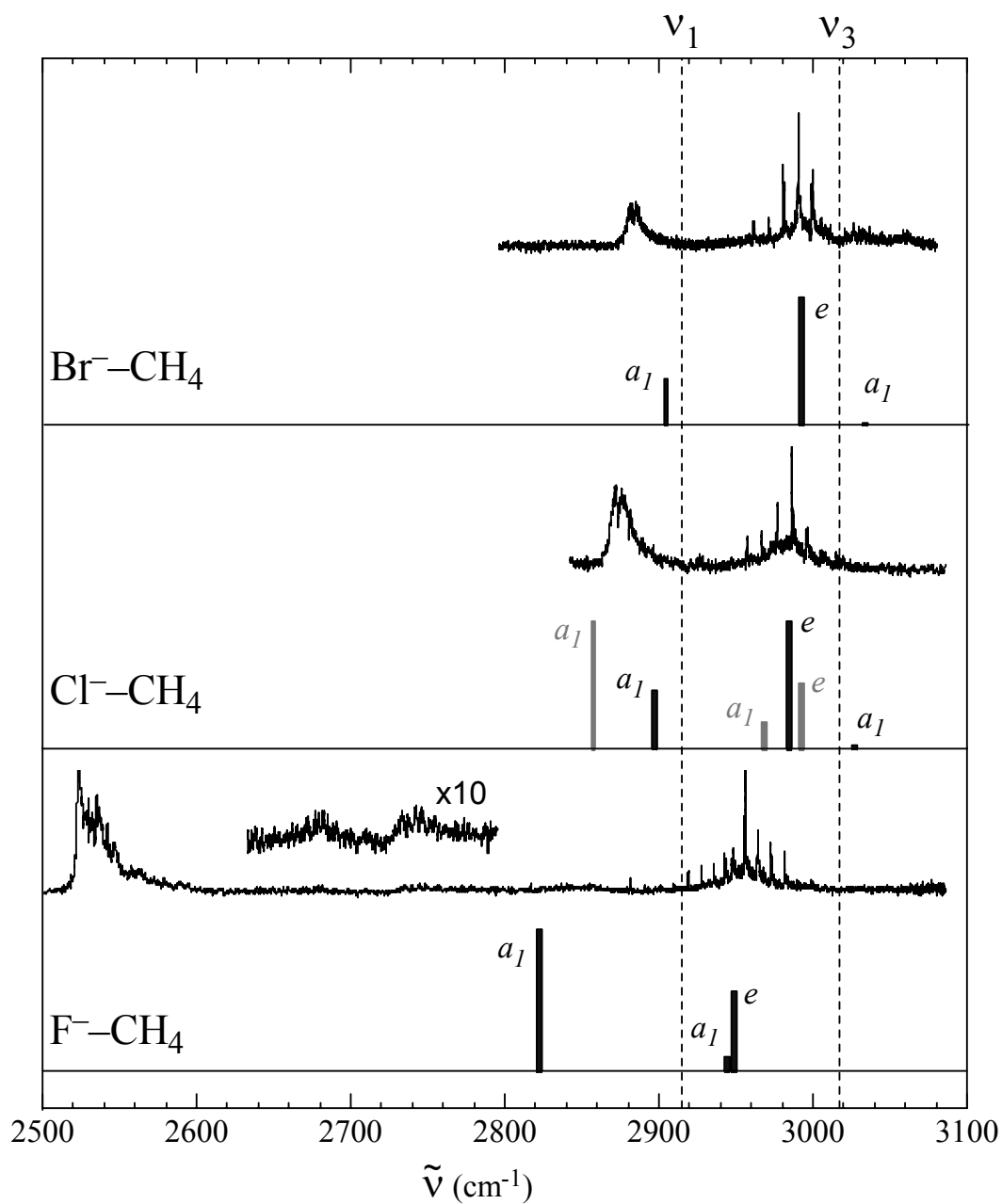
Figure 5.4: *Infrared spectra of the F⁻–CH₄, Cl⁻–CH₄ and Br⁻–CH₄ dimers. Frequencies of the $\nu_1(a_1)$ and $\nu_3(f_2)$ vibrations of bare methane are indicated by dashed lines. The stick spectra based on the ab initio calculations of Novoa et al.[12] (black lines; frequencies scaled by 0.921) and Wild et al.[14] (grey lines; frequencies scaled by 0.944).*

5.3.1 Band assignments

The infrared spectra of the F^-–CH_4, Cl^-–CH_4, and Br^-–CH_4 dimer complexes feature two prominent transitions in the 2500–3100 cm^{-1} range. The higher frequency band displays the sharp Q–branches expected for a perpendicular transition of a prolate symmetric top, and therefore is assigned to the $\nu_3(e)$ band. The lower frequency band displays the characteristic form of a parallel transition, with a clear band gap for the Cl^-–CH_4 and Br^-–CH_4 complexes. This parallel band is assigned to the $\nu_1(a_1)$ mode, rather than to the $\nu_3(a_1)$ mode, as the calculations suggest that $\nu_1(a_1)$ is more intense than $\nu_3(a_1)$ and is shifted further from the bare methane C–H stretch bands. The absence of the $\nu_3(a_1)$ band is at first surprising, however the calculations indicate that the band is quite weak, and it is possible that it is concealed by the $\nu_3(e)$ band. The structure of the bands and the similarity between the *ab initio* and experimental spectra suggest that the halide–methane complexes adopt vertex–bound C_{3v} structures.

The spectrum of the F^-–CH_4 complex also contains two very weak bands at $\sim$2680 cm^{-1} and $\sim$2745 cm^{-1} (see Fig. 5.4) for which only tentative explanations can be offered. One possible assignment is to overtones of the bending vibrational modes localised on the CH_4 sub–unit. In particular, the overtone of the CH_4 $\nu_4(f_2)$ mode ($2\nu_4 = 2600$ cm^{-1}, ref. 15) occurs in the appropriate region. Alternatively, the bands may be due to combinations of $\nu_1(a_1)$ and the intermolecular stretching or bending modes. Assignment of the 2745 cm^{-1} band to the $\nu_1(a_1) + \nu_s$ combination implies that the ν_s intermolecular stretch mode has a frequency of $\sim$210 cm^{-1}, which compares favourably with the theoretical prediction of 199 cm^{-1} from ref. 12 .

5.3.2 Vibrational band structures and shifts

The $\nu_1(a_1)$ band

For all three complexes the $\nu_1(a_1)$ band is shifted to lower frequency from the $\nu_1(a_1)$ symmetric stretch of the bare CH_4 molecule (2914.2 cm^{-1}; ref. 15). The magnitude of the band shift for the X^-–CH_4 complexes decreases in the order F^- $\gg Cl^- > Br^-$ in accord with the calculations of Novoa *et al.*[12] Although the

calculations correctly predict the order of the band shifts, there is less than satisfactory agreement with the actual band positions. The calculations slightly overestimate the $\nu_1(a_1)$ frequency of the Cl^-–CH_4 and Br^-–CH_4 complexes (by ~20 cm^{-1}), and massively overestimate the frequency of the F^-–CH_4 complex (by ~285 cm^{-1}). It seems that the anharmonicity in the C–H stretching potential is not adequately accounted for by simply scaling the *ab initio* harmonic stretching frequencies, particularly for the F^-–CH_4 complex. Similar, although more extreme effects have been observed in experimental and theoretical studies of the isoelectronic F^-–H_2O complex.[17] More reasonable theoretical estimates for the $\nu_1(a_1)$ frequency may be obtained by employing the vibrational self–consistent field (VSCF) method that has been used successfully to account for anharmonicities and intermode couplings in the Cl^-–H_2O complex.[18, 19] It is worthwhile noting that the *ab initio* calculations for Cl^-–CH_4 at the MP2(full)/aug–cc–VTZ level[14] predict a lower frequency $\nu_1(a_1)$ frequency than the calculations of Novoa *et al.*[12]

The $\nu_1(a_1)$ bands have asymmetric profiles, with each displaying evidence for the formation of a P–branch head. This is particularly evident for the F^-–CH_4 complex. Formation of a head in the P–branch indicates that excitation of the intermediate proton leads to contraction of the intermolecular bond, and subsequent increase in the *B* rotational constant of the complex. This effect is related to the vibrational dependence of the methane electrical properties. For methane, vibrational excitation presumably increase the vibrationally averaged local dipole moment of the hydrogen bonded C–H group, either due to electrical or mechanical anharmonicity, leading to an increase in the electrostatic attraction with the halide anion.

The $\nu_1(a_1)$ bands for the Cl^-–CH_4 and Br^-–CH_4 complexes show evidence of rotational structure, with narrow features whose widths are limited by the bandwidth of the infrared light source (~0.017 cm^{-1}). The situation is complicated however by the presence of the various overlapping *K* sub–bands, with the resulting spectral congestion making it extremely difficult to assign the transitions.

The $\nu_3(e)$ band

The $\nu_3(e)$ bands of the F^-–CH_4, Cl^-–CH_4, and Br^-–CH_4 complexes are shown in more detail in Fig. 5.5. The bands are shifted to lower frequency with respect to that of the $\nu_3(f_2)$ band of bare methane (3019.5 cm^{-1}; ref. 20), as predicted by the calculations of Novoa *et al.*[12] The profiles of the $\nu_3(e)$ bands are consistent with C_{3v} prolate symmetric top structures, with the prominent Q–branches assigned as the ^RQ_K ($\Delta K = +1$) and ^PQ_K ($\Delta K = -1$) transitions. If the most intense peak is assigned to the $^RQ_0$ transition, the Q–branches follow the strong–weak–weak–strong pattern expected for a prolate symmetric rotor with three equivalent off–axis hydrogen atoms.[15] The $\nu_3(e)$ band origins will lie approximately midway between the $^PQ_1$ and $^RQ_0$ peaks, at around 2952, 2982, and 2986 cm^{-1} for F^-–CH_4, Cl^-–CH_4, and Br^-–CH_4, respectively. There is better agreement between the experimental and calculated band positions (corrected by 0.9621) for these bands than for the $\nu_1(a_1)$ bands (refer to Fig. 5.1).
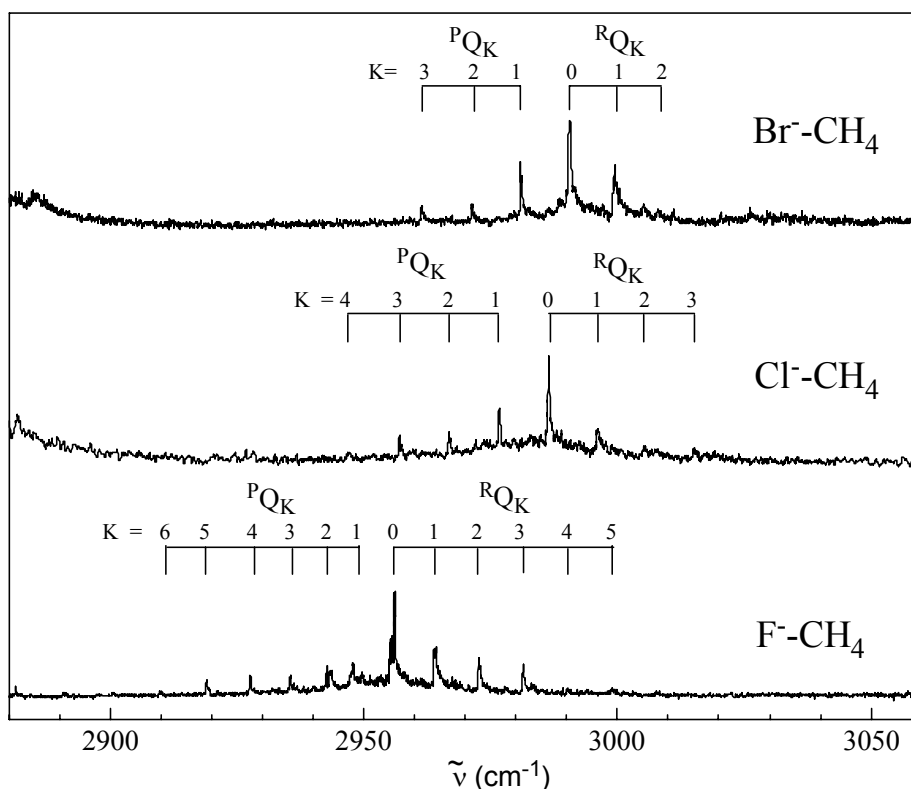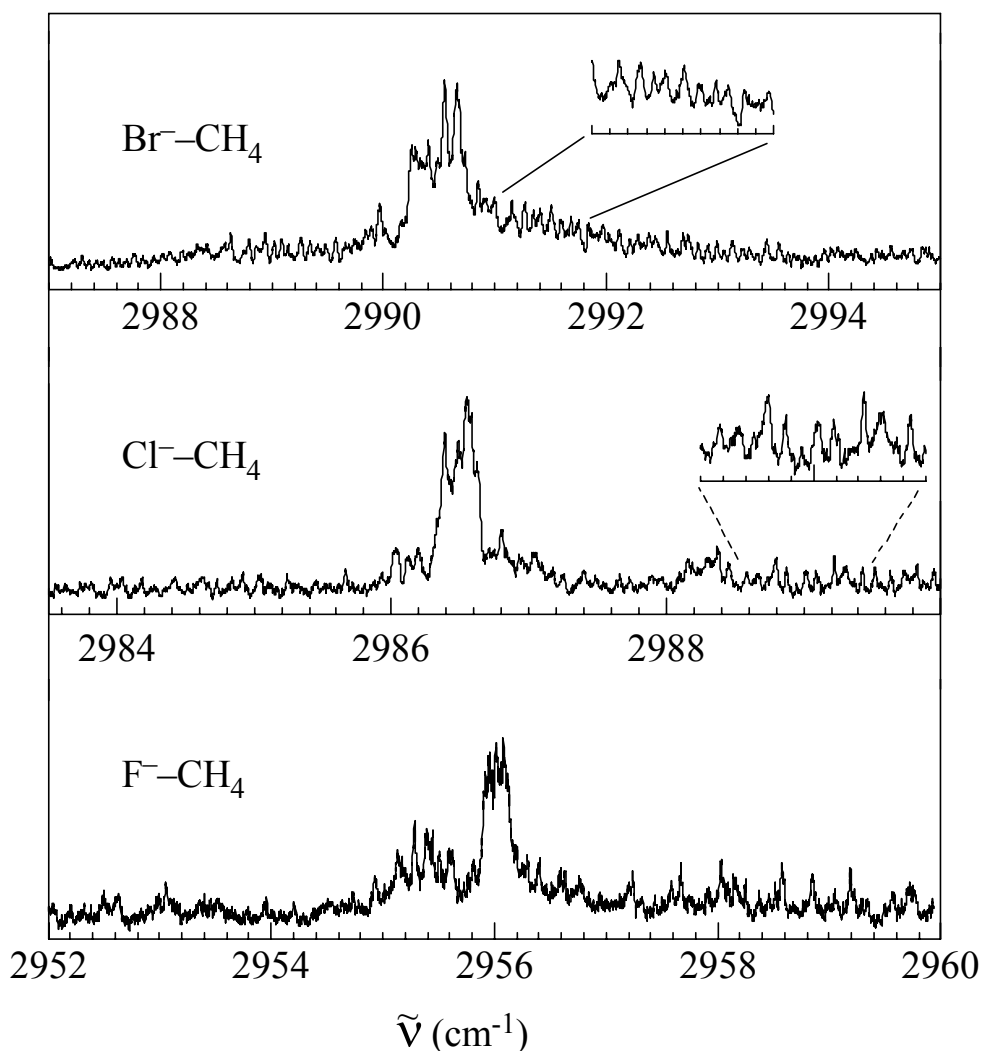

Figure 5.5: *The $\nu_3(e)$ bands of the F^-–CH_4, Cl^-–CH_4, and Br^-–CH_4 complexes. The Q–branches follow the strong–weak–weak–strong pattern expected for a prolate symmetric rotor containing three identical off–axis H atoms. Q–branch positions are summarised in Table 5.2.*

For a prolate symmetric rotor, the Q–branch spacings are given by $2A'(1-\zeta_3)-2B'$, where A' and B' are rotational constants for the complex, and ζ_3 is the Coriolis coupling constant for the ν_3 mode. Assuming the structural parameters from Novoa *et al*,[12] and using the Coriolis coupling constant for CH_4 ($\zeta_3 = 0.05533$; ref. 15) the Q–branch spacings are calculated to be 9.7, 9.8, and 9.9 cm^{-1} for F^--CH_4, Cl^--CH_4, and Br^--CH_4, respectively. These compare reasonably well with the observed spacings of 8.2, 9.7, and 9.2 cm^{-1} for F^--CH_4, Cl^--CH_4, and Br^--CH_4, respectively.

Inspection of the regions to either side of the Q–branches of the $\nu_3(e)$ bands reveals resolved P and R branch rovibrational transitions corresponding to $\Delta J = -1$ and $\Delta J = +1$ respectively. The most intense $\Delta K = 1 \leftarrow 0$ Q–branches for the F^--CH_4, Cl^--CH_4, and Br^--CH_4 complexes are presented in Fig. 5.6. Unfortunately, assigning and analysing these $\Delta J = \pm 1$ transitions is precluded by the poor S/N ratios of the spectra, especially for the P–branch transitions. However, the resolved features do provide some information on the dissociation dynamics of the halide–methane complexes. The widths of the rovibrational lines are limited by the $\sim 0.017\ cm^{-1}$ bandwidth of the OPO light source. Since lifetime broadening is estimated to contribute less than $0.01\ cm^{-1}$ to the width of the rovibrational lines, vibrational predissociation must occur on a timescale longer than 530 ps. A rough upper limit to the lifetime of the vibrationally excited state is provided by their dissociation during the $\sim 100\ \mu s$ flight time through the octopole ion guide.

The Q–branches of the $\nu_3(e)$ band are split into two or more components, with typical separations of $\sim 0.1-0.2\ cm^{-1}$. The splitting is compelling evidence that the complexes are not locked into the prolate symmetric top structures, and that tunnelling between the equivalent hydrogen–bonded minimum energy structures is occurring. While the poor S/N ratios of the spectra precludes analysis of the P/R branch rotational structure, it seems that there are at least two superimposed sets of P and R branch lines with slightly different sub–band origins. For example, whereas the calculations for the Cl^--CH_4 suggest that the spacing between P and R branch lines in each band should be $2B \sim 0.2\ cm^{-1}$ (from ref. 14) the spacing between the R–branch lines in Fig. 5.6 is $\sim 0.1\ cm^{-1}$.

Figure 5.6: *Expanded view of $\Delta K = 1 \leftarrow 0$ Q–branches of the $\nu_3(e)$ bands for F^-–CH_4, Cl^-–CH_4, and Br^-–CH_4. The spectra show resolved P and R branch transitions. The Q–branch splitting and spacing of the P and R branch transitions in the Cl^-–CH_4 and Br^-–CH_4 spectra indicate that tunnelling is significant.*

Given that internal rotation of the methane moiety is not quenched, an understanding of the energy level structures and infrared spectra of the X^-–CH_4 complexes requires solution of the hindered–rotor Hamiltonian for an atom interacting with a tetrahedral molecule in its ground and triply degenerate $\nu_3(f_2)$ state. Discussions of this problem can be found in refs. 1, 21 and 22. Of the other atom–tetrahedral complexes characterized so far, the X^-–CH_4 complexes appear to be most similar to Ar–NH_4^+, with both systems preferring proton–bound structures and having

similar binding energies. In a thorough study, Lakin *et al.*[6, 7] determined the energy level structure of Ar–NH$_4^+$ using *ab initio* and fitted potential energy surfaces. Simulations of the $\nu_3(e)$ infrared band showed that the splittings between *A*, *T*, and *E* components in each $\Delta K = \pm 1$ sub–band diminish as the system approaches the prolate symmetric top limit, mainly due to the introduction of higher order anisotropy terms into the intermolecular PES. The calculated barriers for internal rotation in F$^-$–CH$_4$, Cl$^-$–CH$_4$, and Br$^-$–CH$_4$ (~1070, ~470, and ~460 cm^{-1} respectively; ref. 12) are substantially larger than for Ar–NH$_4^+$ (204 cm^{-1}; ref. 6) and this appears to be reflected in the smaller $\nu_3(e)$ band splittings for X$^-$–CH$_4$ complexes compared to Ar–NH$_4^+$ (0.1–0.2 cm^{-1} *vs* 0.5–1.0 cm^{-1}; ref. 5).

A more comprehensive understanding of the X$^-$–CH$_4$ potential energy surfaces and mid–infrared spectra will require further experimental and theoretical effort. On the experimental side, higher resolution spectra with improved S/N ratios are desirable so that the P and R branch structure in the $\nu_3(e)$ band can be properly resolved and assigned. Linking the experimental spectrum with the intermolecular PES requires solution of the hindered–rotor Hamiltonian describing the interaction of an atom and a tetrahedral molecule in its ground and triply degenerate ν_3 state.

5.4: Comparison of X$^-$–CH$_4$, X$^-$–NH$_3$, and X$^-$–H$_2$O

It is worthwhile concluding this discussion of the X$^-$–CH$_4$ anion complexes by comparing their structural and vibrational properties with the isoelectronic X$^-$–NH$_3$ and X$^-$–H$_2$O gas phase anion species. Particular attention is given to the chloride complexes as they have been investigated theoretically at comparable levels (MP2/aug–cc–pVTZ).

The X$^-$–CH$_4$, X$^-$–NH$_3$, and X$^-$–H$_2$O complexes all possess proton–bound equilibrium conformations in which a perturbed neutral ligand is attached to the X$^-$ anion through a single hydrogen bond. To some extent, all three of the complexes can be considered as two Lewis bases sharing an intermediate proton. As the proton affinities (PAs) of OH$^-$, NH$_2^-$, and CH$_3^-$ (1635, 1692, and 1744 kJ/mol respectively; refs. 23–25) considerably exceed those of F$^-$, Cl$^-$ and Br$^-$ (1555, 1395, and 1354 kJ/mol respectively; refs. 26 and 27), there should be only marginal proton transfer

from the ligand towards the halide. For proton–bound complexes, the strength of the intermolecular bond and disruption to the ligand's geometrical and vibrational structure are usually correlated with the difference between the PAs of the participating bases (ΔPA).[28, 29] When ΔPA is small, the proton is effectively delocalized between the two bases, resulting in the formation of a short, strong intermolecular bond, and a large red–shift in the frequency of the proton stretch vibrational mode. As the ΔPA increases, the proton becomes more localized on the base with higher PA. For these complexes, the intermolecular bond is weaker and the red shift for the proton stretch frequency is smaller.

Theoretical and experimental data for $Cl^-–H_2O$ (refs. 30–32), $Cl^-–NH_3$ (ref. 33), and $Cl^-–CH_4$ (refs. 12 and 14) (ΔPA = 240, 297, 349 kJ/mol respectively) are consistent with the expectations outlined above and demonstrate that the $X^-–CH_4$ complexes are relatively weakly bound compared to $X^-–H_2O$ and $X^-–NH_3$. Both the intermolecular bond strength and extent of proton transfer increase in the order $X^-–CH_4 < X^-–NH_3 < X^-–H_2O$. For example, the calculated binding energies for $Cl^-–CH_4$, $Cl^-–NH_3$, and $Cl^-–H_2O$ are 793, 2695, and 5075 cm^{-1} respectively, while the calculated increases in the $X–H_b$ bondlengths ($X = C$, N, and O) accompanying complex formation with Cl^- are $\Delta R_{X–H} = 0.006$, 0.018, and 0.028 Å. The vibrational red–shifts also vary in the expected way. The modest ~40 cm^{-1} displacement for the $\nu_1(a_1)$ vibration of $Cl^-–CH_4$ with respect to the free CH_4 $\nu_1(a_1)$ mode can be compared with the corresponding ~275 and ~580 cm^{-1} shifts for the H–bonded N–H and O–H groups of the $Cl^-–NH_3$ and $Cl^-–H_2O$ complexes.[33, 34]

5.5 Summary

Infrared spectra of the gas phase halide–methane anion complexes recorded in the vicinity of the C–H stretching modes display a parallel band assigned to the $\nu_1(a_1)$ mode and a perpendicular band assigned to the $\nu_3(e)$ mode. These assignments are consistent with vertex bound C_{3v} minimum energy structures for the complexes. Splittings observed in the Q–branches indicate that the complexes are not rigid and that internal rotation of the methane moiety is not completely quenched.

The experimental spectra were compared with simulated spectra based on *ab initio* calculations. Generally the calculations overestimate the frequencies of the $\nu_1(a_1)$ modes, especially for the F^-–CH_4 complex, possibly due to the neglect of anharmonicity in the C–H stretching potential. Agreement between the experimental and calculated frequencies for the $\nu_3(e)$ modes are much better, with the calculations adequately predicting the experimental Q–branch spacings.

The available data indicates that the systems can be viewed as weakly bound complexes in which the methane molecule essentially maintains its chemical integrity. Support for this contention comes from the observations that the $\nu_1(a_1)$ and $\nu_3(e)$ bands are only marginally displaced from the transitions of the free CH_4 molecule ($\Delta\nu_1(a_1) = -379$, -40, and -31 cm^{-1} for F^-–CH_4, Cl^-–CH_4, and Br^-–CH_4 respectively and $\Delta\nu_3(e) = -67$, -37, and -33 cm^{-1} for F^-–CH_4, Cl^-–CH_4, and Br^-–CH_4 respectively).

5.6 References

1. T. G. A. Heijmen, P. E. S. Wormer, A. van der Avoird, R. E. Miller and R. Moszynski, J. Chem. Phys. **110**, 5639 (1999)

2. R. E. Miller, T. G. A. Heijmen, P. E. S. Wormer, A. van der Avoird and R. Moszynski, J. Chem. Phys. **110**, 5651 (1999)

3. R. W. Randall, J. B. Ibbotson and B. J. Howard, J. Chem. Phys. **100**, 7051 (1994)

4. Y. Kawashima, R. D. Suenram, G. T. Fraser, F. J. Lovas and E. Hirota, J. Mol. Spectrosc. **197**, 232 (1999)

5. E. J. Bieske, S. A. Nizkorodov, O. Dopfer, J. P. Maier, R. J. Stickland, B. J. Cotterell and B. J. Howard, Chem. Phys. Lett. **250**, 266 (1996)

6. N. M. Lakin, O. Dopfer, M. Meuwly, B. J. Howard and J. P. Maier, Mol. Phys. **98**, 63 (2000)

7. N. M. Lakin, O. Dopfer, B. J. Howard and J. P. Maier, Mol. Phys. **98**, 81 (2000)

8. N. M. Lakin, R. V. Olkhov and O. Dopfer, Faraday Discuss. **118**, 455 (2001)

9. O. Dopfer, S. A. Nizkorodov, M. Meuwly, E. J. Bieske and J. P. Maier, Chem. Phys. Lett. **260**, 545 (1996)

10. N. Kashihira, E. Vietzke and G. Zellermann, Chem. Phys. Lett. **39**, 316 (1976)

11. M. Shanshal, Z. Naturforsch. **33a**, 1069 (1978)

12. J. J. Novoa and M–H. Whangbo, Chem. Phys. Lett. **180**, 241 (1991)

13. K. Hiraoka, T. Mizuno, T. Iino, D. Eguchi and S. Yamabe, J. Phys. Chem. **105**, 4887 (2001)

14. D. A. Wild, Z. M. Loh, P. P. Wolynec, P. S. Weiser and E. J. Bieske, Chem. Phys. Lett. **332**, 531 (2000)

15. G. Herzberg, *Molecular Spectra and Molecular Structure II: Infrared and Raman Spectra of Polyatomic Molecules* (Krieger, Malabar, 1991)

16. G. C. Pimentel and A. L. McClellan, *The Hydrogen Bond* (W.H. Freeman, New York, 1960)

17. P. Ayotte, J. A. Kelly, S. B. Nielsen and M. A. Johnson, Chem. Phys. Lett. **316**, 455 (2000)

18. S. Irle and J. M. Bowman, J. Chem. Phys. **113**, 8401 (2000)

19. G. M. Chaban, J. O. Jung and R. B. Gerber, J. Chem. Phys. **111**, 1823 (1999)

20. L. Henry, N. Husson, R. Andia and A. Valentin, J. Mol. Spectrosc. **36**, 511 (1970)

21. J. E. Hutson and A. E. Thornley, J. Chem. Phys. **100**, 2505 (1994)

22. R. W. Randall, J. B. Ibbotson and B. J. Howard, J. Chem. Phys. **100**, 7042 (1994)

23. P. A. Schulz, R. D. Mead, P. L. Jones and W. C. Lineberger, J. Chem. Phys. **77**, 1153 (1982)

24. C. T. Wickham–Jones, K. M. Ervin, G. B. Ellison and W. C. Lineberger, J. Chem. Phys. **91**, 2762 (1989)

25. G. B. Ellison, P. C. Engelking and W. C. Lineberger, J. Am. Chem. Soc. **100**, 2556 (1978)

26. C. Blondel, P. Cacciani, C. Delsart and R. Trainham, Phys. Rev. A. **40**, 3698 (1989)

27. J. D. D. Martin and J. W. Hepburn, J. Chem. Phys. **109**, 8139 (1998)

28. M. Meot–Ner and O. Dopfer, J. Am. Chem. Soc. **106**, 1257 (1984)

29. E. J. Bieske and O. Dopfer, Chem. Rev. **100**, 3963. (2000)

30. P. Ayotte, G. H. Weddle, J. Kim and M. A. Johnson, J. Am. Chem. Soc. **120**, 12361 (1998)

31. J–H. Choi, K. T. Kuwata, Y–B. Cao and M. Okumura, J. Phys. Chem. **102**, 503 (1998)

32. S. S. Xantheas, J. Phys. Chem. **100**, 9703 (1996)

33. P. S. Weiser, D. A. Wild, P. P. Wolynec and E. J. Bieske, J. Phys. Chem. **104**, 2562 (2000)

34. J. A. Kelly, J. M. Weber, K. M. Lisle, W. H. Robertson, P. Ayotte and M. A. Johnson, Chem. Phys. Lett. **327**, 1 (2000)

Appendix 1

Tables A.1-8: *Wavenumbers for rovibrational transitions observed for the X^-–H_2 and X^-–D_2 complexes (Differences (last significant figure) between the measured and calculated positions are given in parentheses, $(\nu_{obs} - \nu_{fit})$). Constants, ν_o, B'', B', D'' and D', are determined from a fit to a pseudo-diatomic energy level expression:*

$$\nu_{obs} = \nu_o + B'\left[J'(J'+1)\right] - D'\left[J'(J'+1)\right]^2 - B''\left[J''(J''+1)\right] + D''\left[J''(J''+1)\right]^2$$

Table A.1: $^{35}Cl^-$–H_2*(o)*

J″	P(J″)	R(J″)
0		4006.68(0)
1	4003.12(0)	4008.65(0)
2	4001.56(0)	4010.74(0)
3	4000.11(0)	4012.96(0)
4	3998.80(0)	4015.33(2)
5	3997.63(-1)	4017.78(0)
6	3996.61(-1)	4020.35(0)
7	3995.76(1)	4023.04(-2)
8	3995.05(2)	4025.88(0)
9	3994.45(0)	4028.82(0)
10	3994.04(0)	4031.88(0)
11	3993.79(0)	4035.06(2)
12	3993.72(0)	4038.35(0)
13		4041.72(-2)
14		4045.28(2)
15		4048.88(-1)
16		4052.64(0)
17		4056.53(0)

Table A.2: $^{37}Cl^--H_2(o)$

J″	P(J″)	R(J″)
0		4006.57(-3)
1	4003.06(0)	4008.55(-2)
2	4001.45(-1)	4010.70(4)
3	4000.06(1)	4012.91(3)
4	3998.76(1)	4015.24(2)
5	3997.59(0)	4017.71(3)
6	3996.58(0)	4020.23(-3)
7	3995.71(0)	4022.93(-3)
8	3995.00(2)	4025.75(-2)
9	3994.37(-3)	4028.68(-2)
10	3993.97(-2)	4031.73(-1)
11	3993.75(2)	4034.92(3)
12		4038.17(3)
13		4041.53(1)
14		4044.97(-1)
15		4048.56(-1)

Table A.3: $^{81}Br^--H_2(o)$

J″	P(J″)	R(J″)
0		4045.98(-2)
1	4043.08(1)	4047.53(-7)
2	4041.76(1)	4049.31(1)
3	4040.54(1	4051.10(0)
4	4039.43(1)	4052.97(-1)
5	4038.45(4)	4054.93(-2)
6	4037.51(0)	4057.02(1)
7	4036.71(-1)	4059.16(0)
8	4036.03(-1)	4061.37(-2)
9	4035.50(1)	4063.72(1)
10	4035.05(0)	4066.09(-3)
11	4034.73(-1)	4068.62(0)
12	4034.53(3)	4071.20(-1)
13	4034.49(-2)	4073.88(0)
14	–	4076.68(4)
15	–	4079.45(-4)
16	4035.18(-4)	4082.43(0)
17	4035.41(3)	4085.52(5)
18	4036.41(-3)	4088.59(-1)
19	4037.31(2)	4091.82(0)
20		4095.11(-3)

Table A.4: $I^- - H_2(o)$

J″	P(J″)	R(J″)
0		4082.32(0)
1	4079.97(-1)	4083.60(1)
2	4078.95(4)	4084.92(0)
3	4077.90(-1)	4086.31(-1)
4	4077.03(4)	4087.75(-4)
5	4076.13(-1)	4089.30(-1)
6	4075.37(0)	4090.92(2)
7	4074.69(1)	4092.56(2)
8	4074.06(-2)	4094.21(-4)
9	4073.54(-1)	4096.00(-2)
10	4073.09(-3)	4097.87(2)
11	4072.81(3)	4099.75(1)
12	4072.53(0)	4101.73(4)
13	4072.38(0)	4103.71(1)
14	4072.33(0)	4105.74(-3)
15		4107.89(-2)
16		4110.11(1)

Table A.5: $^{35}Cl^- - D_2(o)$

J″	P(J″)	R(J″)
0		2879.48(0)
1	2877.59(0)	2880.49(0)
2	2876.72(1)	2881.57(2)
3	2875.88(1)	2882.65(-1)
4	2875.11(0)	2883.79(-1)
5	2874.37(0)	2885.00(0)
6	2873.68(-1)	2886.24(1)
7	2873.06(1)	2887.51(0)
8	2872.46(-1)	2888.82(-1)
9	2871.94(1)	2890.19(0)
10	2871.45(0)	2891.60(0)
11	2871.02(0)	2893.04(0)
12	2870.63(-1)	2894.53(0)
13	2870.31(0)	2896.05(-1)
14		2897.63(0)
15		2899.24(1)
16		2900.88(0)
17		2902.57(0)
18		2904.29(0)

Table A.6: ^{35}Cl$^-$–D$_2$(p)

J″	P(J″)	R(J″)
0		2879.70(-2)
1	2877.83(0)	2880.72(-1)
2	2876.96(1)	2881.82(3)
3	2876.11(-2)	2882.89(1)
4	2875.35(1)	2884.06(2)
5	2874.61(0)	2885.23(0)
6	2873.92(-1)	2886.48(1)
7	2873.30(0)	2887.75(0)
8	2872.72(1)	2889.06(-1)
9	2872.17(-1)	2890.43(0)
10	2871.72(2)	2891.83(0)
11	2871.29(1)	2893.28(0)
12	2870.90(0)	2894.77(0)
13	2870.57(-1)	2896.29(-1)
14		2897.87(0)
15		2899.50(2)
16		2901.10(-3)
17		2902.82(0)
18		2904.56(1)

Table A.7: ^{79}Br$^-$–D$_2$(o)

J″	P(J″)	R(J″)
0		2908.26(2)
1	2906.70(-2)	2909.05(0)
2	2906.01(0)	2909.89(-1)
3	2905.34(1)	2910.77(-1)
4	2904.68(-1)	2911.68(-1)
5	2904.08(0)	2912.62(-1)
6	2903.50(-1)	2913.60(-1)
7	2902.97(-1)	2914.61(0)
8	2902.48(0)	2915.65(0)
9	2902.01(-1)	2916.73(1)
10	2901.61(1)	2917.83(0)
11	2901.24(2)	2918.95(-1)
12	2900.85(-2)	

Table A.8: $^{79}Br^{-}-D_2(p)$

J″	P(J″)	R(J″)
0		2907.68(1)
1	2906.16(2)	2908.48(-1)
2	2905.43(0)	2909.32(-1)
3	2904.76(1)	2910.21(0)
4	2904.12(1)	2911.11(-1)
5	2903.50(-0)	2912.06(0)
6	2902.92(1)	2913.02(-2)
7	2902.40(0)	2914.04(0)
8	2901.90(0)	2915.07(-1)
9	2901.44(-0)	2916.15(0)
10	2901.01(1)	2917.25(1)
11	2900.64(0)	2918.38(1)
12	2900.29(0)	2919.53(0)
13	2900.00(-1)	2920.73(1)
14	2899.73(1)	2921.94(-1)
15	2899.53(-1)	2923.19(-1)
16	2899.34(1)	2924.48(0)
17	2899.22(0)	2925.80(0)
18	2899.15(1)	2927.14(0)
19		2928.53(1)
20		2929.93(0)
21		2931.35(-2)

Table A.9: *Data for the sharp structure observed in the ν_3 bands of the $Br^--C_2H_2$ and I^- $-C_2H_2$ dimer complexes. Provided are the peak positions, incremental shifts from the initial peak, and peak widths (fwhm). Numbers in parentheses for $I^--C_2H_2$ correspond to incremental shifts calculated by Botschwina et al for the $\nu_3+n\nu_s-n\nu_s$ sequence band series.[1]*

Br⁻–(C₂H₂)			I⁻–(C₂H₂)		
Peak Position (cm⁻¹)	Incremental Shift (cm⁻¹)	fwhm (cm⁻¹)	Peak Position (cm⁻¹)	Incremental Shift (cm⁻¹)	fwhm (cm⁻¹)
2978.8 ± 0.2	0	0.2	3071.8 ± 0.2	0	0.5
2986.2 ± 0.2	7.4	2	3079.0 ± 0.2	7.2 (6.6)	2
2992.5 ± 0.2	6.3	4	3085.8 ± 0.2	6.8 (6.5)	2.5
2996.5 ± 0.2	4	2	3092.2 ± 0.2	6.4 (6.5)	3
3004.0 ± 0.2	7.5	4	3099.0 ± 0.5	6.8 (6.4)	3.5
3012.0 ± 0.2	8	2	3104.5 ± 0.5	5.5 (6.2)	4
3020.1 ± 0.2	8.1	4			
3028.0 ± 0.2	7.9	2			
3036.1 ± 0.2	8.1	2			
3044.0 ± 0.2	7.9	2			
3052.0 ± 0.2	8	2			
3056.2 ± 0.2	4.2	2			
3060.0 ± 0.2	3.8	2			

1. P. Botschwina and H. Stoll, Phys. Chem. Chem. Phys. **3**, 1965 (2001)